# Magnetic Resonance Investigations of pH in Microemulsions

by
Nicola Ann Halliday

A thesis submitted to
the University of Birmingham
for the degree of
DOCTOR OF PHILOSOPHY

School of Chemistry
College of Engineering and Physical Sciences
University of Birmingham
October 2010

# Abstract

The work presented in this thesis has investigated the development of magnetic resonance (MR) techniques to probe the pH in aqueous solutions and reverse micelles formed in CTAB, Triton-X and AOT microemulsions. These techniques have enabled visualisation of propagating acidity fronts in the bromate-sulfite reaction using magnetic resonance imaging.

Contrast agents that are sensitive to pH were investigated in aqueous and microemulsion media. Successful magnetic resonance imaging of the aqueous system was achieved using the pH-dependent chelation of the paramagnetic species Cu(II), with the chelating ligand triethylenetetramine. However, it was found that MR contrast agents were not required for probing the pH in reverse micelles of the CTAB and Triton-X microemulsions. Magnetic resonance imaging of the bromate-sulfite reaction in a CTAB microemulsion system was achieved without the need for additional probe molecules or contrast agents and was found possible following investigations of pH in reverse micelles of the microemulsion using MR relaxation times.

$T_2$ relaxation times of water in the CTAB and Triton-X microemulsions were found to change with pH, however, $T_1$ relaxation times remained unaffected. This behaviour was attributed to acid-catalysed exchange between protons of water and hydroxyl protons of the cosurfactant alcohol in these systems. These findings present the first direct monitoring of pH in reverse micelles of microemulsion systems without the need for probe molecules.

# Acknowledgements

First and foremost, I would like to thank my supervisor Melanie, whose support, assurance and continued belief in my ability has contributed enormously to the existence of this thesis. I would also like to thank Dr Andrew Peet and Dr Annette Taylor for their contributions in numerous discussions, and whose comments were always gratefully received.

To the members of the Britton group, past and present, I owe sincere gratitude: to Dr Nossov, for Madame Bovary; to Jan and Heather, for suffering me so graciously; to Antoine, for just being Antoine and to Binks, for becoming one of my greatest friends (and for suffering me not-so-graciously!). My thanks also go to all of my colleagues and friends in the School of Chemistry over the past four years: Sam, Tom, Johanna, Lasse, Andy, Oliver, Loggy, Jon, Christina, Laura, Simon, Claire, Charlotte, Graham, Sarah, Josephine, Fabrice, Neil and Helen. This list is by no means complete and to all of those people with whom I have shared a tea–break or been acquainted over the last four years, my thanks go to you. To Ian, I would like to acknowledge that we are *still* at uni. together and that it has been great. Special acknowledgment must be given to Professors Roy Johnston and Richard Tuckett, who are two people that I feel privileged to have known.

I would like to thank my closest friends, Deb and Lynette, for their continued willingness to offer me tea, listen and make me smile, just when I need it.

To my family, I would like to thank you for more than I could ever hope to express in words and for representing everything that I truly value.

And finally, to Ad, thank you for making me happy, each and every day.

This thesis and the work described in it are entirely my own, except where I have acknowledged either help from a named person or a reference is given to a published source or a thesis. Text taken from another source has been enclosed in quotation marks and a reference given.

1st October 2010

# Contents

# List of tables

# List of figures

# 1 Thesis introduction

## 1.1 Introduction to nonlinear dynamics

Travelling fronts are ubiquitous in nature[1, 2]; from the spread of fire to the formation of slime moulds. The fronts can manifest as stationary patterns, such as the animal markings of zebras and tigers, and display periodic behaviour, such as the beating of the heart. Although these patterns can be appreciated, the underlying mechanisms that determine the observable may not easily be defined and when irregularities within the pattern occur, an explanation can be lacking; arrhythmia can be diagnosed however its cause is not fully understood. Recent decades have seen an explosion of interest in the field of nonlinear chemical dynamics[3] and their application in understanding biological behaviour, with a number of reviews being published[4-6]. The coupling of nonlinear, autocatalytic reactions with diffusion has demonstrated a wealth of behaviour that mimics features encountered, not only in nature, but also in areas of physics, biology, geology and engineering. Reaction-diffusion models have been used to account for propagation of signals in nerve axons[7] and to explain various ecological patterns, such as migration and predator/prey populations[5]. This subject is thus, not only of interest to chemists, but also to physicists and biologists for example, such that the universal relevance of reaction-diffusion phenomena has propelled the growth of the field of nonlinear chemical dynamics.

The first reported nonlinear chemical system was the Landolt clock, which was reported in 1886. The reaction demonstrated the rapid, autocatalytic production of a coloured iodide species after an initial period where the reaction mixture remained

colourless. In 1906, Luther[8, 9] published the first description of propagating reaction fronts in a chemical system. However, it was the discovery of the oscillatory Belousov-Zhabotinsky (BZ) reaction[10], nearly 70 years later, that reignited the interest and study of nonlinear chemical reactions. Oscillatory reactions had previously been reported[11, 12] but the chemical community remained reluctant to accept the findings, believing that the phenomenology violated the second law of thermodynamics[13]. The self-organising patterns of the BZ reaction however, which displayed amazing similarities to, for example, pattern formation in slime moulds (Figure 1.1), combined with the subsequent mechanistic understanding of the reaction that was developed by Field, Koros and Noyes[14, 15], ensured that the area of nonlinear chemical dynamics became a topic of significant interest.

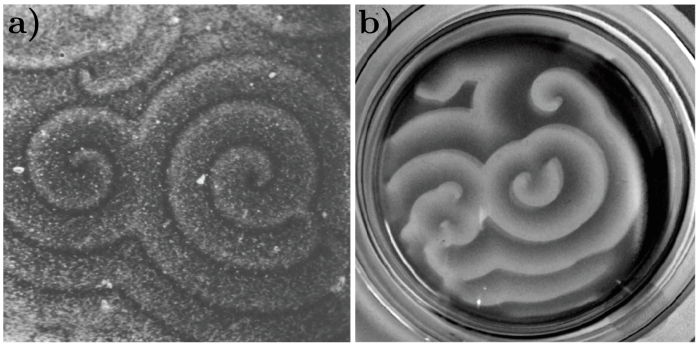


Figure 1.1: Patterns observed in a) a population of *dicytostelium discoideum* undergoing chemotactic movement[16] and b) the BZ reaction performed in a Petri dish[17].

Since the discoveries, there have been numerous studies aimed at a greater range of non-linear reactions. Many more reactions have been found over the last few decades and taxonomy of reactions is now possible: The BZ reaction is an example of a bromate oscillator but chlorite, thiosulfate, iodate and many other chemical oscillators exist[4, 18, 19]. The majority of these reactions only produce chemical oscillations in time in an open system, for example a continuous stirred-tank reactor

(CSTR), and display clock behaviour and chemical fronts in closed reactors. Only a few reactions, the BZ being an example, can produce patterns. Several of these nonlinear reactions are pH clocks that are capable of displaying propagating acidity fronts[20-23]. The investigation of nonlinear pH reactions is of particular importance since hydrogen ion concentration plays a significant role in a range of inorganic reactions and biological processes. Propagating waves of protons have been observed in glial cells[24] and pattern formation has been observed near the surface of *chara corallina* cells arising from the distribution of acid/base as a function of light[25].

More recently, focus has shifted to the study of autocatalytic reactions in gels[26, 27] and microemulsions[28, 29] since homogenous aqueous systems do little to represent differing diffusive properties that are present in natural structures. The realisation of Turing patterns, a specific type of stationary patterns that result from the sole coupling of reaction and diffusion processes and that were first hypothesised by the mathematician Alan Turing[30], were first observed by Patrick De Kepper's group[26]. The Turing patterns were observed in the chlorite-iodide-malonic acid (CIMA) system using a continuously fed unstirred reactor (CFUR) that contained a thin layer of polyacrylamide gel. The incorporation of the BZ reaction in a bis(2-ethylhexyl) sulfosuccinate (AOT) based water-in-oil microemulsion medium expanded the range of patterns that had previously been observed[29] in the BZ reaction, and included Turing structures that are not achieved in the aqueous system. A summary of some of the patterns found in the BZ-AOT system is shown in Figure 1.2. To date, the only studies of a non-linear pH reaction in water-in-oil microemulsions have been performed by McIlwaine *et al.*[28]. They have demonstrated that the behaviour of the reaction system is sensitive to the structure of the microemulsion and that

propagating fronts are supported whose behaviour is unlike that observed in the aqueous analogue[28].

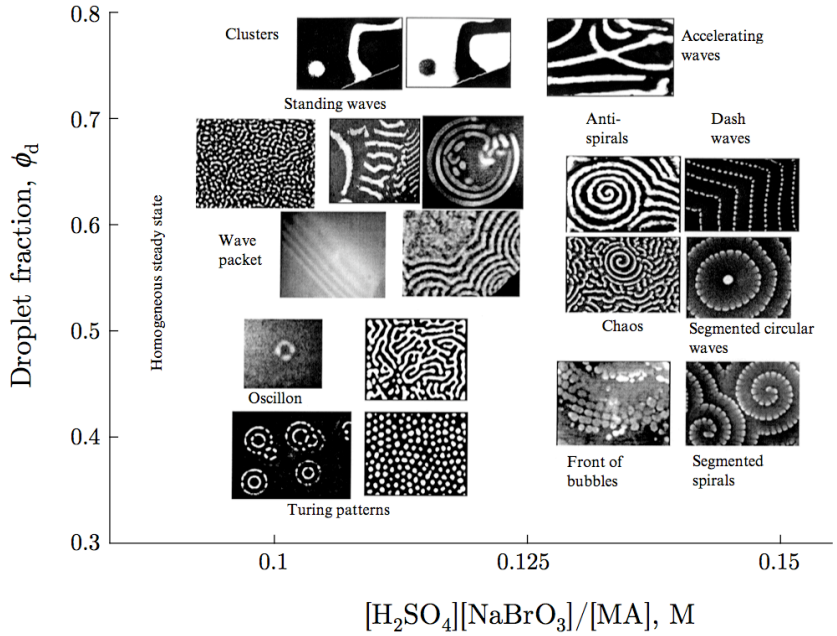


Figure 1.2: Schematic overview of patterns found in the BZ-AOT system[29]. The $x$-axis represents the concentrations of BZ reactants whilst the $y$-axis reflects a change in the structure of the microemulsion.

This introductory chapter provides an overview of nonlinear reaction kinetics, front propagation in autocatalytic systems and water-in-oil microemulsions and their applications. Particular attention is given to the bromate-sulfite reaction and its behaviour in a water-in-oil microemulsion as described by McIlwaine *et al.*[28] This system has been investigated using magnetic resonance and dynamic light scattering techniques and an introduction will be provided for these techniques.

## 1.2 Kinetics

### 1.2.1 Nonlinearity and autocatalysis

Most reaction mechanisms consist of a series of elementary steps, each of which is considered to describe an individual molecular event within the overall reaction process. The rate of an elementary step is given in terms of the concentrations of participating reactants and the rate coefficient, $k$. For example, the elementary process in 1.1 has the rate equation shown in 1.2:

$$\mathrm{A} + \mathrm{B} \longrightarrow \mathrm{C} \tag{1.1}$$

$$\text{Rate} = k\,[\mathrm{A}][\mathrm{B}] \tag{1.2}$$

The combination of all the elementary steps must give the correct overall reaction stoichiometry and account for the experimentally observed rate law. Elementary steps are typically bimolecular; from equation 1.1 the implication is that a molecule of A collides with a molecule of B to produce C. This bimolecular process results in a rate law containing a quadratic term, which thus, by definition describes nonlinear kinetics.

Nonlinearity itself does not produce clock or oscillatory behaviour, the majority of elementary steps are bimolecular processes[31] and thus nonlinearity is the norm and not the exception. For clock or oscillatory behaviour to occur, the system must firstly be far from its equilibrium position, and secondly, must display feedback within the reaction mechanism. Feedback is the process by which products in later steps of the mechanism influence the rate of an earlier reaction step. The most common form of feedback in chemical kinetics is autocatalysis. Reaction scheme 1.3 displays quadratic

autocatalysis and has the rate equation given in 1.4. From this simplified schematic it can be seen that production of species B will accelerate and thus, species B is known as the autocatalyst.

$$\mathrm{A} + \mathrm{B} \longrightarrow 2\mathrm{B} \tag{1.3}$$

$$\text{Rate} = k\,[\mathrm{A}][\mathrm{B}] \tag{1.4}$$

## 1.3 Chemical clocks

Chemical clocks are a simple example of a nonlinear reaction that feature autocatalysis. Clock behaviour is characterised by a period of little change in the concentration of some chemical species, which is known as the induction period, followed by a rapid change in the concentration of that species (Figure 1.3). The Landolt reaction is probably the most famous example of this and displays a sharp colour change from colourless to blue-black, which is associated with the rapid formation of a triiodide-starch complex as the reaction 'clocks'. In the case of the Landolt clock, $I^-$ is the autocatalyst. The final state of the system, i.e. after the reaction has 'clocked', is the equilibrium state of the system.

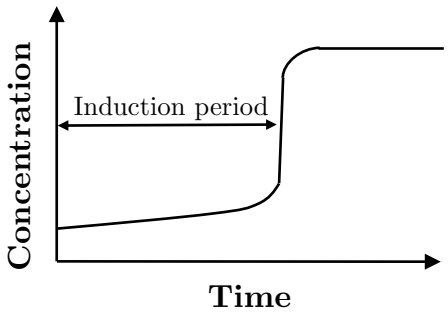


Figure 1.3: Schematic of a clock reaction performed in a stirred batch reactor.

Numerous examples of chemical clocks have been reported, including those that involve the oxidation of thiosulfate by bromate[23] and chlorite[22] and reactions between oxyhalides and iodine[32, 33]. Clock reactions that do not involve oxyhalide species are limited but include the reaction of formaldehyde with a sulfite/bisulfite buffer[34]. For many clock reactions, acidity affects the rate of reaction[23] and in pH clocks, the autocatalytic production of $OH^-$ or $H^+$ species is observed. Oscillatory behaviour arises when a separate feedback mechanism contributes to 'resetting' the clock. The oxidation of sulfite and ferrocyanide by bromate displays oscillatory behaviour when performed in a CSTR.[35]

## 1.4 Propagating fronts

Autocatalytic reactions of the type listed in section 1.3 can also demonstrate propagating reaction fronts[8, 9, 23]. Reaction fronts are universal and since the work of Fisher[36] and Kolmogorov[37], reaction-diffusion models have been used to describe the front behaviour observed, not only in chemical systems but also those of a biological[5], physical[38, 39] and environmental[40] nature. A reaction front is defined as the propagating interface at which reactants are converted to products, and arises through the coupling of diffusion of the autocatalytic species with reaction of that species. With respect to clock reactions; at the locale where the reaction is initiated there is a rapid increase in the concentration of the autocatalyst, diffusion then allows the autocatalyst to spread to neighbouring regions triggering the autocatalytic reaction in those areas and producing a rapid increase in the autocatalyst concentration. The front is hence able to progress at a rate faster than under pure diffusion alone.

Travelling reaction fronts have been reported in a number of autocatalytic chemical systems[41-45]. The reaction between nitric acid and iron(II) displays travelling waves when an inhibitor (hydrazine) is used to stabilise the reaction mixture[46]. Propagating acidity fronts result from the diffusion of protons produced in the chemical reaction coupling to their autocatalytic effect. Szirovicza *et al.*[23] have developed an algorithm for designing systems that support propagating acidity fronts based on the redox reactions of oxyanions. A combination of reactions between oxyhalogen ions and oxyanions of sulfur containing an S-S bond were investigated and the behaviour described; 20 of the 30 reactions investigated displayed propagating acidity fronts whilst four of the reactions occurred quickly without a front.

For a clock reaction to display a propagating reaction front a) the clock time must be sufficiently long to ensure diffusion controlled reaction of the autocatalyst and b) the reaction must originate from a localised area of the reaction mixture. This is achieved by using initial reactant concentrations that favour a long induction period, and by supplying a confined area of the unstirred reaction mixture with the autocatalyst[23, 43]. Often, cylindrical tubes are used and initiation is performed at one end of the tube: if the point of initiation covers the surface area of the tube, a single direction of propagation results (Figure 1.4).

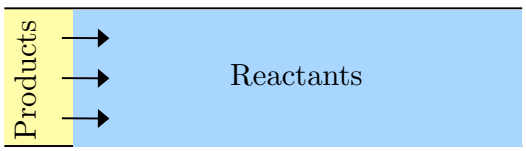


Figure 1.4: Schematic of a reaction-diffusion front. The arrows indicate the direction of front propagation.

A pure reaction-diffusion front in an aqueous-phase system will typically travel with a constant waveform[47] and at a constant speed[8, 9, 31], $v$, that is dependent upon the diffusion coefficient, $D$, of the autocatalyst, the pseudo-first-order rate constant, $k$, for the reaction and a proportionality constant, $a$ (equation 1.5).

$$v = a\sqrt{kD} \tag{1.5}$$

## 1.5 The bromate-sulfite reaction

### 1.5.1 Clock behaviour

The reaction of a bromate solution with a bisulfite/sulfite solution is known to display clock behaviour when performed in batch in a closed system[18, 28, 48]. The reaction produces a sharp drop in pH, from approximately 7 to approximately 2, following conversion of bisulfite ($HSO_3^-$) to hydrogen sulfate ($HSO_4^-$), and proceeds according to the reaction mechanism[28, 49] proposed by Hanazaki and Rabai[49]:

$$BrO_3^- + HSO_3^- \rightarrow BrO_2^- + SO_4^{2-} + H^+ \tag{1.6}$$

$$BrO_2^- + 2HSO_3^- \rightarrow Br^- + 2SO_4^- + 2H^+ \tag{1.7}$$

$$BrO_2^- + 2H_2SO_3 \rightarrow Br^- + 2SO_4^- + 4H^+ \tag{1.8}$$

$$BrO_3^- + H_2SO_3 \rightarrow BrO_2^- + SO_4^- + 2H^+ \tag{1.9}$$

$$HSO_3^- \rightleftharpoons SO_3^- + H^+ \tag{1.10}$$

$$H_2SO_3 \rightleftharpoons HSO_3^- + H^+ \tag{1.11}$$

$$HSO_4^- \rightleftharpoons SO_4^- + H^+ \tag{1.12}$$

The induction period of the clock reaction is controlled by reaction 1.6 and the equilibrium process 1.10; the acid produced through the reaction of bromate with

bisulfite (1.6) protonates the sulfite initially present in the buffer solution (reverse reaction 1.10), thus maintaining the concentration of bisulfite. Once the sulfite species has been consumed, $H^+$ autocatalysis occurs and can be demonstrated through consideration of reactions 1.9 and 1.11; as the concentration of acid increases, the rate of production of $H_2SO_3$ increases in reaction 1.11 and subsequently the rate of formation of acid increases in reaction 1.9.

#### *1.5.1.1 Stirring effects*

The induction period of the aqueous bromate-sulfite clock reaction is dependent on the initial concentration of reactants. The induction period is also dependent on the stirring rate of the system[50], with an increase in the stirring rate resulting in an increase in the induction period. This behaviour has also been observed for the autocatalytic batch reactions of chlorite-thiosulfate[22] and chlorite-iodide[51] and for the oscillatory Briggs-Rauscher[52] and BZ[53] reactions. Vanag and Melikhov[54] have described this stirring phenomenon as being an effect of fluctuations or nuclei on the dynamics of the averages, where nuclei are defined as "short-living, accidentally appearing microvolumes where autocatalysis induced by the large-scale fluctuations starts much earlier than in the rest of the reactionary volume". The rationale for the increased induction period of the bromate-sulfite reaction with an increased stirring rate is thus that lower stirring rates allow for a critical, autocatalytic acid concentration to be achieved, for a given unit volume, more readily than in a well-stirred system[50].

### 1.5.2 Front behaviour

The bromate-sulfite reaction also demonstrates propagating reaction fronts[43, 50]. Keresztessy *et al.*[43] have investigated travelling fronts of the bromate-sulfite reaction in cylindrical tubes of inner diameter (i.d.) 0.14 to 5.95 cm. Tubes of i.d. 0.14 cm were demonstrated to support the propagation of both ascending and descending flat fronts. In a tube of i.d. 0.26 cm the ascending front was found to be slightly curved and the descending front had a significant parabolic shape, whilst fronts in tubes of larger inner diameters were distorted due to convection[43]. The ascending and descending front velocities for tubes of i.d. 0.26 cm were found to be 0.33 and 1.04 cm $min^{-1}$ respectively, however the ascending front travelled much faster than the descending front in larger tubes[43]. The behaviour of the front deviated from that predicted by pure reaction-diffusion models[8, 9, 55] and demonstrated the contribution of convection to the rate of propagation[56].

#### *1.5.2.1 Convective effects*

Hydrodynamic processes can significantly affect the behaviour of reaction-diffusion fronts[55, 57]. Convection can enhance wave velocities and the shape of the front can also be altered. The types of convection that can occur include simple convection and double-diffusive convection and depend on the density difference, $\Delta\rho$, between the products and reactants (equation 1.13, where $\rho_r$ and $\rho_p$ are the densities of the reactant and product solutions, respectively).

$$\Delta\rho = \rho_p - \rho_r \qquad (1.13)$$

The density difference produced during a reaction is a combination of the difference in densities associated with the composition, $\Delta\rho_c$, due to the difference between the

molar volumes of the products and reactants, as well as a thermal contribution, $\Delta\rho_T$, due to the exo-/endothermicity of the reaction (equation 1.14). Note that an exothermic reaction causes thermal expansion and a subsequent $-\Delta\rho_T$.

$$\Delta\rho = \Delta\rho_c + \Delta\rho_T \tag{1.14}$$

According to Pojman and Epstein[56] if both $\Delta\rho_T$ and $\Delta\rho_c$ are of the same sign then simple convection will occur, however, if the signs are opposite then double-diffusive convection may occur. Convective effects have been investigated and observed in a range of autocatalytic reactions[57] and a summary of these studies is given in Table 1. The table has been reproduced from an article by D'Hernoncourt *et al.*[57] and the reader is encouraged to seek the references therein for further details. The bromate-sulfite reaction is exothermic, with an enthalpy change of $-1070 \pm 10$ kJ mol$^{-1}$, and has an isothermal density change of $2.40 \times 10^{-4}$ g cm$^{-3}$, thus double-diffusive convection was expected and was observed[43].

Table 1: A list of autocatalytic reactions whose density effects have been investigated, and their associated solutal ($\Delta\rho_c$) and thermal ($\Delta\rho_T$) density changes[57].

| **Reaction** | $\Delta\rho_c$ | $\Delta\rho_T$ |
|---|---|---|
| Bromate-sulfite | + | − |
| Nitric acid-iron(II) | + | − |
| Chlorite-thiosulfate | + | − |
| Chlorite-tetrathionate | + | − |
| Chlorate-sulfite | + | − |
| Chlorite-thiourea | + | − |
| Polymerisation front | + | − |
| Iodate-arsenous acid | − | − |
| Iodide-nitric acid | − | − |
| Iodate-sulfite | − | − |
| Combustion front | − | − |

## 1.6 Alternative reaction media

The ability to have some form of control over the chemical reaction is important to assist in a systematic study of behaviour. The presence of hydrodynamic convection can often be undesirable and so gel systems are frequently employed to study nonlinear reactions[26, 27]. By investigating chemical fronts and patterns in a gel, convective contributions are eliminated and it becomes possible to probe the behaviour that is purely associated with the chemistry of the reaction. It is apparent that theoretical descriptions of reaction-diffusion phenomena can be compared only with experimental findings that are based solely on reaction-diffusion and not on reaction-diffusion-convection. In addition to suppressing convection, gels also provide a medium that allows for a greater control of the reaction. Gel media, such as silica gel and alginate, are able to immobilise different chemical species within a reaction,

leading to differences in diffusivities of the reactants[27]. The investigation of the CIMA reaction in a polyacrylamide gel produced the first realisation of Turing patterns[26]. These patterns were visualised using a starch indicator that was immobilised in the polyacrylamide gel. The starch formed a coloured complex with triiodide ions produced in the reaction, through the formation of a starch-iodide complex. The formation of this complex effectively inhibited the diffusion of the iodide species resulting in Turing patterns, which are not observed in the aqueous analogue.

Microemulsions have also proved to be a valuable medium in which to study nonlinear reactions. The range of patterns observed in the BZ reaction was expanded, and included Turing structures, when performed in AOT microemulsions[29]. The range of patterns observed was achieved, not only, by adjusting the concentrations of the reactants but also by the ability to adjust the structure of the microemulsion system.

## 1.7 Microemulsions

### 1.7.1 Introduction to microemulsions

Microemulsions have widespread applications[58]; they have been frequently employed in cleaning systems/detergents and as separators, owing to their ability to solubilise both hydrophilic and hydrophobic components, and have been used in the delivery of transdermal drugs[59] where they facilitate an increased absorption of the drug through the skin. More recently, the use of microemulsions has been proposed in the field of enhanced oil recovery where a higher viscosity and ability to induce low interfacial tension may increase the efficiency of oil extraction[60]. Reverse micelles in

water-in-oil microemulsion systems are of particular interest[61-63] since they display compartmentalisation and confinement of water, which are features shared with biological membranes[64, 65]. RMs have thus been used as model systems for studying biological processes such as enzymatic reactions[66-68]. Chemical reactions performed in reverse micelles are sensitive to the nature of the confined water[69]. The effect of pH in the aqueous environment, for example, has particular significance in acid-catalysed[70] and electron transfer reactions[71]. The interest in reverse micellar systems thus spans a range of disciplines, with the properties of confined water within such systems being of particular interest to chemists and biologists.

A microemulsion (μE) is an isotropic, thermodynamically stable and optically transparent mixture of water, oil, surfactant and, frequently, co-surfactant. The surfactant is often an amphiphilic molecule (Figure 1.5a) and can be; cationic, for example, cetyltrimethylammonium bromide (CTAB); non-ionic, for example, Triton X-100 (TX) and anionic, for example, AOT (Figure 1.5b-d). The surfactant molecules serve to lower the interfacial tension between the two immiscible solvents, and do so by self-organising so as to minimise the unfavourable interactions between the polar solvent and the hydrophobic "tails" of the surfactant, and between the apolar solvent and the hydrophilic "head groups" of the surfactant. In mixtures of oil and water, and in the absence of a surfactant, an emulsion can form; however, such mixtures are thermodynamically unstable and, with time, separate into the two different phases. The second defining feature of a microemulsion, compared to that of an emulsion, is transparency: microemulsions consist of sub-microscopic structures that do not significantly scatter visible light. Emulsions, however, contain dispersed droplets that have a diameter generally greater than 200 nm, resulting in an opaque

system. Microemulsions thus represent a macroscopically homogenous yet microscopically heterogeneous medium.

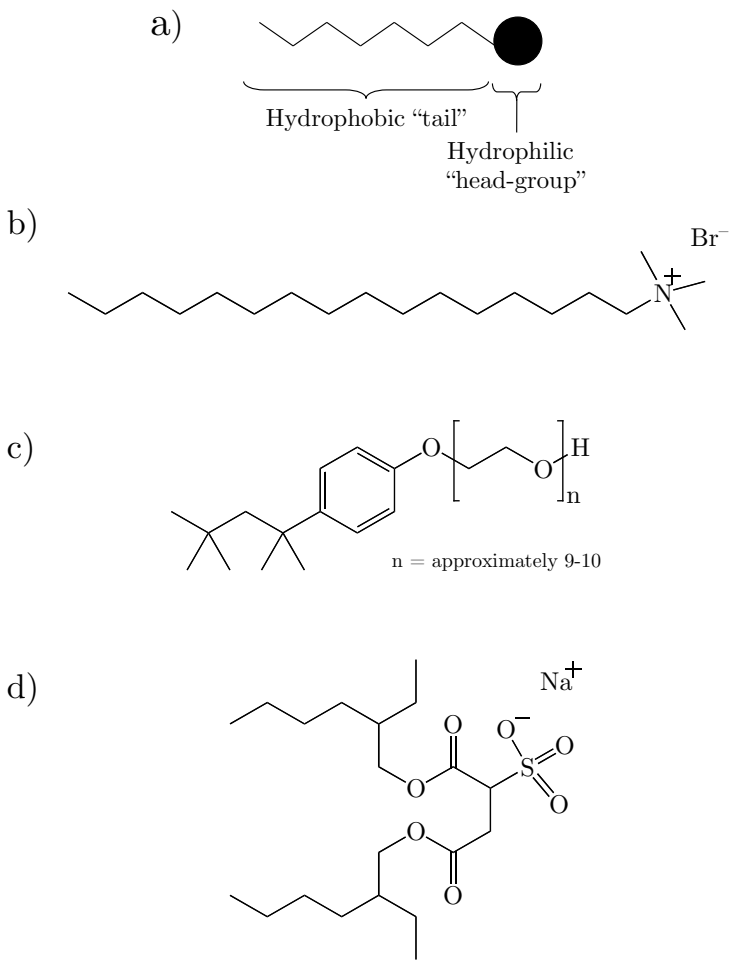


Figure 1.5: Figures illustrating a) a schematic of an amphiphilic molecule and b) the cationic cetyltrimethylammonium bromide (CTAB), c) the nonionic Triton X-100 (TX) and d) the anionic sodium bis(2-ethylhexyl) sulfosuccinate (AOT) surfactant molecules.

#### *1.7.1.1 Composition*

The composition and phase behaviour of water, oil and surfactant mixtures are often described using a ternary phase diagram, a schematic of which is illustrated in Figure 1.6. The apex of the triangle represents a volume fraction of 100 % of the

indicated component and moving away from the apex represents a decrease in the percentage volume of that component within the mixture. The composition can consist of one, two or three phases that can be characterised by diffusion measurements, optical examination, conductance and viscosity. A phase diagram is constructed that describes the structure adopted for a given composition at a constant temperature, pressure and ionic strength.

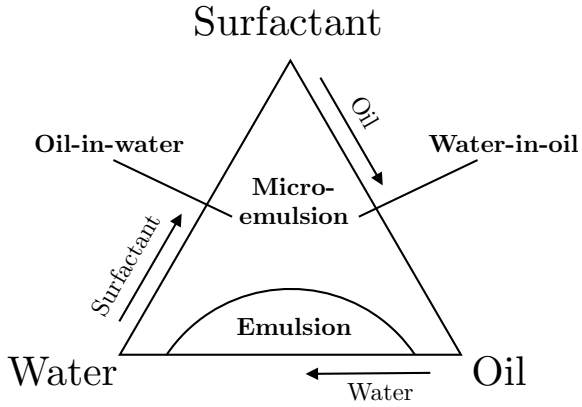


Figure 1.6: Schematic ternary phase diagram for a water-oil-surfactant system. The apex represents a volume fraction of 100 % of the expressed component. Note that for systems containing a cosurfactant, a pseudoternary phase diagram is constructed with an apex representing both the surfactant and cosurfactant.

For different compositions the mixture can self-organise to form oil-in-water (o/w) or water-in-oil (w/o) microemulsions. An oil-in-water microemulsion contains nanosized droplets of oil that are sequestered from the continuous water phase by a monolayer of surfactant molecules. Conversely, water-in-oil microemulsions contain nanosized droplets of water that are sequestered from the continuous oil phase by a monolayer of surfactant molecules (Figure 1.7). In a w/o microemulsion, the surfactant molecules self-organise in such a manner that the hydrophobic tails of the surfactant remain exposed to the apolar solvent whilst the hydrophilic heads are sequestered in the reverse micellar core. These self-assembled structures are known as

reverse micelles (RMs). RMs are typically spherical in shape and have a hydrodynamic radius, $R_d$ that is the sum of the water core and surfactant length, the radius of the water droplet is denoted $R_w$.

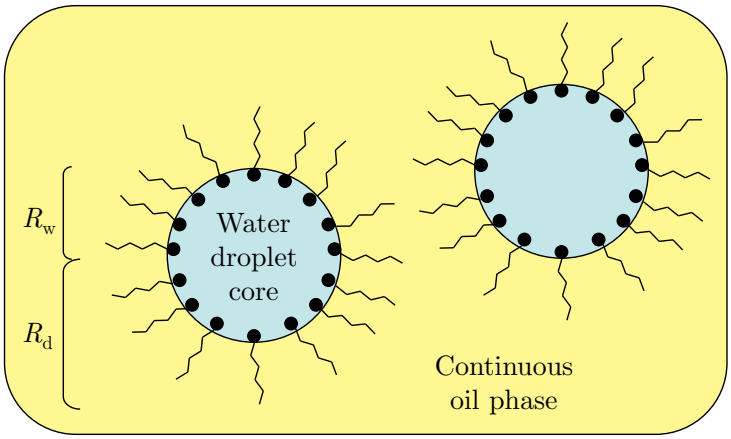


Figure 1.7: Schematic of a water-in-oil microemulsion. A monolayer of surfactant molecules surrounds the water droplet from the continuous oil phase. The hydrophobic tails of the surfactant remain exposed to the apolar solvent whilst the hydrophilic heads are sequestered in the reverse micellar core. $R_w$ is the radius of the water droplet whilst $R_d$ is the radius of the micelle i.e. the sum of the water core and surfactant length.

For many systems that constitute oil, water and surfactant, a cosurfactant is required in order to form RMs. The cosurfactant is often an alcohol that is able to partially locate itself amongst the interface. This arrangement minimises unfavourable electrostatic interactions between charged surfactant headgroups[72] and facilitates the uptake of water by the RM. The chain length of the alcohol affects the interfacial properties and thus affects the amount of water that can be solubilised[73]. For systems using a cosurfactant, a pseudoternary phase diagram is often constructed whereby the cosurfactant is represented as a fixed ratio to the surfactant. The surfactant AOT forms RMs in oils without using a cosurfactant and is consequently one of the simplest and most widely studied and understood

microemulsion systems[74]. The formation of RMs in CTAB systems, however, does require a cosurfactant to be employed.

W/o microemulsions are characterised by two important parameters which control the concentration of droplets and the droplet size; these are, the droplet fraction, $\phi_d$ (equation 1.15), and the molar ratio, $\omega_0$ (equation 1.16), respectively.

$$\phi_d = \frac{V_{water} + V_{surfactant}}{V_{water} + V_{surfactant} + V_{oil}} \quad (1.15)$$

$$\omega_0 = \frac{[H_2O]}{[surfactant]} \quad (1.16)$$

$V_{water}$, $V_{surfactant}$ and $V_{oil}$ are the volumes of the aqueous, surfactant and oil phases respectively and $[H_2O]$ and [surfactant] are the concentrations of the aqueous and surfactant phases respectively. The ratio $\omega_0$ is related to the radius of the water droplet, $R_w$, with an increase in $\omega_0$ correlating to an increase in the diameter of the droplet[75, 76]. For AOT microemulsions the relationship between $R_w$ and $\omega_0$ is well defined[76] and is given in equation 1.17; $R_d$ is given in equation 1.18, where 1.1 nm is the approximate length of an AOT molecule. Due to the increased complexity of other microemulsions, particularly, those that use CTAB, such definitions are not currently possible.

$$R_w = 0.17\omega_0 \quad \text{(nm)} \quad (1.17)$$

$$R_d = 0.17\omega_0 + 1.1 \quad \text{(nm)} \quad (1.18)$$

*1.7.1.2 Confinement of water*

The structure and properties of water confined within reverse micelles are of great interest to scientists and have been the subject of many studies. Numerous techniques have been employed to investigate the structure of the water as a function of the droplet size; IR spectroscopy has been used to measure OH stretching vibrations as a function of $\omega_0$ and differing surfactant concentrations[77, 78], and calorimetric methods have been utilised[79]. $^{1}H$ and $^{23}Na$ NMR spectroscopy has been used to probe the effect of droplet size on the NMR relaxation times of both water and counterions in AOT reverse micellar systems[80]. The measurements made during these studies[77-80] demonstrated that the water within the RMs exist in different environments and that the overall environment of the water is strongly dependent on $\omega_0$ and the nature of the surfactant. Typically, two types of water were found to exist; water at the interface associated with the polar headgroups and, for larger values of $\omega_0$, remaining water that forms the bulk of the so-called "water pool"[81]. For charged interfaces i.e. those of AOT and CTAB, there also exists a layer of counterions that attach to the charged interface and so in these systems, interfacial water is also associated with these charged species. These findings have led to the description of the water in a *two-phase* model[82]. A *three-phase* model[82] has also been proposed[83, 84] that further describes the water located at the interface by two different types, that of water located between the surfactant chains, and water that solvates the head group: this model has been supported by recent FT-IR studies by Valero *et al.*[85]

Solvation dynamics in w/o microemulsions has been investigated using various molecular probes[69, 75, 86]. The water present at the reverse micellar interface

demonstrates ultraslow dynamics of solvation[69, 75, 86] and is thus often termed "bound" water, whilst water molecules within the bulk of the water pool are often referred to as "free" water. An increase in $\omega_0$ correlates to an increase in "free" water: Levinger *et al.*[86] have investigated solvation dynamics in RMs of the isooctane-AOT-water system using time-resolved fluorescence spectroscopy. For smaller droplet sizes, ($\omega_0 < 5$), they found that water molecules were highly immobile due to a greater proportion of the water pool being in the "bound" environment. As the droplet size was increased, the overall mobility of water increased.

The structure of the water within the nanosized droplets has a marked effect on its properties, which differ significantly from those of bulk water. Intramicellar ionic strength[87], viscosity[87-90] and polarity[90-92] have been investigated using spectroscopic measurements of probe molecules: fluorescence techniques have been used to measure the viscosity-sensitive, fluorescence probe auramine O in AOT systems[88, 89] and the photophysical behaviour of acridine orange in RMs of AOT[91, 93] and TX[91] microemulsion. Zhu and Schelly[92] have used the probe molecule methyl orange and its characteristic absorption behaviour to investigate w/o microemulsions of TX as a function of $\omega_0$. Increased microviscosity of water confined within ionic and non-ionic microemulsions has been reported[87-90] and a change in the effective polarity observed[90-92]. The properties of the water confined in RMs approaches those of bulk water as $\omega_0$ increases, however, even for large values of $\omega_0$, the properties of the intramicellar water remain different.

The characterisation of pH in microemulsions has also relied on the use of spectroscopic measurements of pH-sensitive probe molecules[81, 87, 93-96] since it is not

possible to insert a glass pH electrode into the water pool of a RM. Biswas *et al.*[96] have used absorption and emission characteristics of two photoactive probe molecules to determine the pH of water in AOT microemulsions. They found that the pH values of the water in w/o microemulsions with $\omega_0 < 10$ were higher than those of pure water and that the pH increased with decreasing $\omega_0$. Baruah *et al.*[87] have used oxovanadate probe molecules and $^{51}$V NMR spectroscopy to study pH in AOT w/o microemulsions.

The use of probe molecules in the study of pH in RMs presents further considerations: the information that they provide will be dependent upon their location within the RMs, and their presence within the microemulsion may have an effect on the structure of the RMs. Intuitively, for example, one may presume that the anionic oxovanadate ions used in the study of AOT reverse micelles would reside in the bulk of the water pool, owing to their hydrophilicity and due to Coloumbic repulsion between the negatively charged surfactant headgroups and the negative charge on the probe molecules. NOESY NMR experiments have been used to determine the location of a different anionic vanadium probe molecule in AOT RMs[97]. The NOE experiments demonstrated that the probe species resides within the hydrophobic region of the micellar interface[97] and not in the bulk of the water pool. Rack *et al.*[98] have discovered that incorporation of the chromophore probe molecule $Ru(bpy)_3^{2+}$ within CTAB based microemulsions dramatically changes the water content and distribution of droplet sizes of the RMs. $^{31}$P NMR has been used[99] to measure the chemical shifts of phosphate buffers contained in RMs[99] thus removing the requirement for additional probe molecules. However, limitations with this method include the need for the aqueous core to be a phosphate buffer and that

the p$K_a$ of phosphate ions are assumed to remain the same in the water pools as they are in bulk water[99, 100]. The definition of pH within RMs thus remains uncertain; the activity of water confined within RMs is unknown, and the pH cannot readily be measured since the restricted water represents a new solvent for which calibration has not been performed[100]. The issues concerning this are thoroughly addressed in a review by Luisi and Smith[100].

### 1.7.2 Reactions in w/o microemulsions

The confinement of water in microemulsions and the properties of the water therein have forged the use of reverse micellar systems as nano-reactors. The components of a chemical reaction can be incorporated into separate water-in-oil microemulsions; upon mixing, reverse micelles coalesce and exchange of the aqueous reactants can occur (Figure 1.8). The intermicellar exchange processes and the chemical kinetics within the nanosized water droplets thus determine the rate of the reaction.

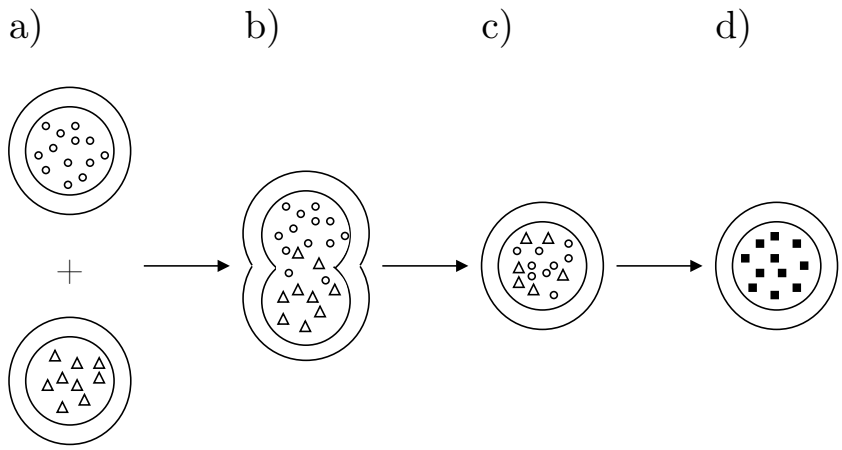


Figure 1.8: A schematic of a reaction in reverse micelles. Two separate w/o microemulsions are prepared thus reactants are compartmentalised in separate reverse micelles, the w/o microemulsions are mixed (a), coalescence occurs and exchange of reactants occurs (b), reverse micelles then contain a mixture of reactants (c) and reaction occurs (d).

The properties of "bound" water within reverse micelles mimic features observed for water associated with biological membranes[64, 65]. Consequently, reactions performed in reverse micelles serve as simplified models of reactions in biological cells[63, 101] and provide a simple, yet effective method to study the fundamental effects of compartmentalisation on reaction kinetics. The ability of reverse micelles to solubilise enzymes has been exploited and enzymatic reactions have been performed in this environment[66-68]. Numerous chemical reactions have also been investigated in reverse micellar systems[62, 74], including polymerisation reactions, ester hydrolysis and the dissociation of a charge-transfer complex. Both the retardation and catalysis of chemical reactions has been observed[62, 74] and is dependent upon the type of reaction occurring and the nature of the reversed micelle. The ability to alter and "fine-tune" the properties of the reverse micelles by adjusting the composition used further enhances the application of such systems and allows for a degree of control over the reaction. Certainly, reverse micelles are now widely used in the synthesis of nanoparticles[102], where the reverse micellar size and structure can be exploited to produce nanoparticles with uniform and pre-defined morphologies.

#### *1.7.2.1 The bromate-sulfite reaction in microemulsions*

Nonlinear, autocatalytic reactions are particularly sensitive to their environment and water-in-oil microemulsions provide a heterogeneous medium in which the effects of differences in diffusion and compartmentalisation on reaction-diffusion phenomena can be investigated. McIlwaine *et al.*[28] have performed studies of the bromate-sulfite reaction incorporated into a non-ionic (TX-toluene-water) and a cationic (CTAB-hexanol-water) microemulsion system and demonstrated that propagating reaction fronts are supported. Front behaviour in the cationic microemulsion displayed

structures, such as a turbulent wake, an extinguishing finger and spiral motion, that were not observed in the anionic microemulsion and that are not observed in the aqueous phase, the following discussion will thus focus on the cationic system.

The phase behaviour of CTAB, hexanol and water mixtures is well understood following investigations by Ekwall *et al.*[103, 104] and for certain compositions of the three components a water-in-oil microemulsion phase exists. Here, the alcohol acts as both continuous oil phase and co-surfactant by partially locating itself in the polar interfacial region. Numerous reactions have been performed in reverse micelles of CTAB[105, 106] and the surfactant is one of the two most frequently used for materials synthesis[102, 107]. The investigations by McIlwaine *et al.*[28] are the only known studies of a nonlinear, pH reaction in water-in-oil microemulsions. The clock behaviour of bromate-sulfite in the CTAB microemulsion was slower than the aqueous phase equivalent and was found to be dependent on $\omega_0$[28], with an increase in $\omega_0$ correlating to a decrease in the induction period. McIlwaine *et al.*[28] suggested that it is likely that the negatively charged reactants reside close to the positively charged micellar interface. In this environment, the micropolarity is reduced[90, 91] and thus the rate of reactions involving the formation of charged species is reduced[69]; this effect will be most pronounced for smaller water droplets, i.e. lower $\omega_0$. The clock times of the bromate-sulfite-CTAB system were highly variable and it was suggested[28] that this demonstrated the sensitivity of the system to nonequilibrium concentration fluctuations[54]. The pH of the system was measured using a combination pH glass electrode and was found to shift to higher pH values compared to those of the aqueous phase[28]. A possible sequestering of $H_2SO_3$ was proposed[28] although, from earlier discussions (section 1.7.1.2) regarding the activity of water, the meaning of

the pH measured using a glass electrode remains ambiguous. A pH indicator (bromocresol purple) was also used in the study; the colour of the bromate-sulfite-CTAB mixture changed at the time with which a sudden drop in the pH was measured using the glass electrode. Although the pH indicator can show the change in the pH associated with the 'clocking' of the reaction, the transition pH range of bromocresol purple is 5.2–6.8 and thus an exact pH cannot be elucidated.

McIlwaine *et al.*[28] also investigated propagating reaction fronts of the bromate-sulfite-CTAB system in vertical tubes of i.d. = 1 and 2.6 mm. In the smaller of the tubes, the front velocity was found to be a factor of 10 lower than the equivalent aqueous phase and did not demonstrate a $\omega_0$ dependence. The diffusion coefficients of the reverse micelles containing the aqueous reactants will be much lower than for the free reactants in a bulk aqueous phase and hence the front propagation will be reduced. However, diffusion effects do not solely contribute to front propagation and the rate of the autocatalytic reaction was dependent on $\omega_0$. Simulations of front behaviour also performed by McIlwaine *et al.*[28] that combined diffusion coefficients with autocatalytic rates as a function of $\omega_0$, suggested that convection affects the front behaviour. Convective effects were observed in tubes of i.d. = 2.6 mm and the behaviour of the front was dependent on $\omega_0$[28]; the structure of the front displayed fingering and differed with $\omega_0$, and a reduced front velocity was observed as $\omega_0$ increased. The structures were described to resemble those of flame fronts, indicating that the mobility of the reacted species differ from those of the unreacted species[28].

The work presented by McIlwaine *et al.*[28] demonstrated that the behaviour of the nonlinear, pH bromate-sulfite reaction was sensitive to the micro-heterogeneity in

which it was performed, particularly the droplet size. Front behaviour was also exhibited that does not exist in the aqueous phase. The studies however, were limited in that the effect of the reaction on the structure of the microemulsion was not probed. The bromate-sulfite reaction is exothermic and temperature is known to affect the structure of the microemulsions[108], thus, there is the possibility that feedback between the microemulsion structure and the reaction exists. Similarly, the effect of $H^+$ production on the nature of the RMs remains unknown and may also contribute to a feedback mechanism, as the autocatalyst propagates. McIlwaine *et al.*[28] measured the pH of the system using a glass electrode, which is unable to probe only the water pool environment of RMs. A better understanding of the definition of pH within microemulsions is necessary before conclusions can be drawn regarding the pH of the system. The visualisation of the fronts was achieved using a charge-coupled device camera and thus a colour indicator was required to provide contrast between the reacted and unreacted regions of the system. The images that were acquired were integrated over the entire sample and so the ability to fully describe the behaviour of the front is restricted. It would be advantageous to further study such systems using methods that are not constrained by such limitations. Magnetic resonance techniques encompass such methods and are discussed in the following sections.

## 1.8 Magnetic resonance imaging in chemistry

Nuclear magnetic resonance (NMR) is an incredibly powerful tool that has proved invaluable in scientific disciplines: in chemistry it is the pre-eminent method that is used for structure elucidation. In chemical engineering, the ability to measure transport properties using NMR is utilised[109] and transport processes within porous

media and flow reactors have been investigated. The use of nuclear magnetic resonance imaging (MRI) techniques has also been employed in materials science[110], although the use of MRI remains primarily in the field of medicine.

Over the past two decades, the application of MRI to the study of nonlinear chemical reactions has proved to be a growing area of research. Tzalmona *et al.*[111] first reported the visualisation of chemical waves produced in an autocatalytic reaction in 1990, where waves of the aqueous manganese-catalysed BZ reaction were observed using MRI. Since then, it has been possible to investigate the BZ reaction in opaque porous media using MRI[112, 113]. MRI has also been used to successfully image pattern formation in the oscillatory 1,4-cyclohexanedione-bromate-acid system[114] and front propagation in the autocatalytic reaction of a cobalt(II) complex with hydrogen peroxide[115]. More recently, the formation of autocatalytic plumes in the iodate-arsenous acid reaction have been imaged using MRI[116] and the effect of exothermicity of the chlorite-thiosulfate reaction on NMR behaviour has been exploited to image chemical fronts in the reaction[117]. To date, MRI of the autocatalytic, pH bromate-sulfite reaction has not been performed and there have been no reported magnetic resonance investigations of a clock pH reaction in water-in-oil microemulsion media.

The work described in this thesis presents the first magnetic resonance investigation of the autocatalytic, pH bromate-sulfite reaction. The behaviour of the reaction has been characterised by measuring the pH as a function of time and using optical imaging, before MRI has been used to image propagating fronts of the reaction in both aqueous and CTAB-based w/o microemulsion media. Magnetic resonance

relaxation times have also been investigated in the microemulsion system as a function of pH, and a possible method for the monitoring of pH changes within these systems proposed. The next section provides an introduction to nuclear magnetic resonance and the techniques that have been used, however, for further details the reader is encouraged to source one of the many texts available on the subject[118-123].

## 1.9 Introduction to Magnetic Resonance Imaging

### 1.9.1 Principles of NMR

#### *1.9.1.1 Nuclear spin*

The subatomic particles electrons, protons and neutrons, each possess an intrinsic angular momentum called spin, which has a value equal to $\frac{1}{2}$. In many atomic nuclei, such as $^{12}C$, the spins of the protons and the neutrons are paired, which removes any net nuclear spin, $I$. However, some atoms, for example $^{1}H$, $^{2}H$ and $^{13}C$, possess nuclei that do have an overall spin that is a positive, non-zero integer or half-integer value: In the hydrogen ($^{1}H$) nucleus, the single unpaired proton results in a nuclear spin of $I = \frac{1}{2}$, whilst the deuterium ($^{2}H$) nucleus has an unpaired proton and an unpaired neutron, giving a nuclear spin of $I = 1$.

A nucleus with spin angular momentum has $2I + 1$ possible orientations along a given axis. Thus the $^{1}H$ nucleus (which will be the only nucleus considered in the proceeding discussion) has two spin states, each of which are given the quantum number $m$ and are equal to $\pm \frac{1}{2}$. In the absence of external fields, these spin states are degenerate in energy. However, the contribution of both motion and charge from

the nucleus generates a magnetic field with magnetic moment $\mu$, and this magnetic moment interacts with a static magnetic field. Consequently, when nuclei possessing a non-zero nuclear spin are placed in a magnetic field, denoted $\boldsymbol{B}_0$, the degeneracy of the spin-states is lost (Figure 1.9): For the $^1$H nucleus, the spins occupy the spin-up ($m = \frac{1}{2}$) and spin-down ($m = -\frac{1}{2}$) states, and are aligned parallel or anti-parallel respectively, with $\boldsymbol{B}_0$.

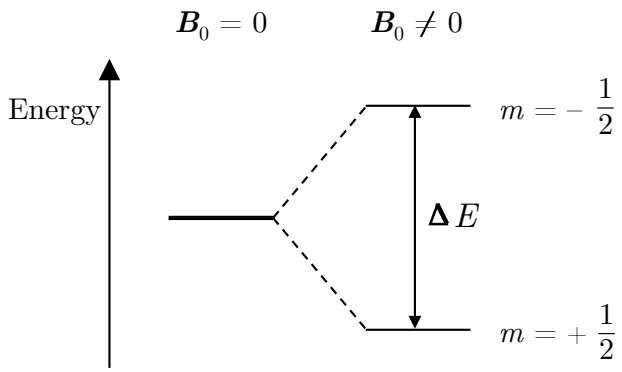


Figure 1.9: An energy level diagram showing the splitting of degenerate spin-states of the $^1$H nucleus in a magnetic field denoted $\boldsymbol{B}_0$. $\Delta E$ is the difference in energy between the two spin states and is given in equation 1.21.

The magnetic field also imposes a torque on the magnetic moments of nuclei, causing the spins to precess about the direction of $\boldsymbol{B}_0$ (Figure 1.10). The rate of precession, which is known as the Larmor frequency, is increased by stronger magnetic fields and is directly proportional to the inherent gyromagnetic ratio, $\gamma$, of the nucleus of interest. Equations for the Larmor frequency are given below, where $\omega$ and $\nu$ denote the Larmor frequency in radians per second (equation 1.19) and Hertz (equation 1.20) respectively.

$$\omega = \gamma \boldsymbol{B}_0 \tag{1.19}$$

$$\nu = \frac{\gamma \boldsymbol{B}_0}{2\pi} \tag{1.20}$$

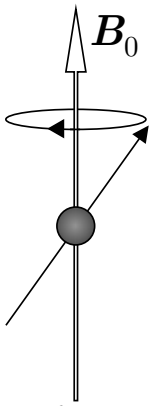


Figure 1.10: Schematic to show precession of a nucleus possessing a non-zero nuclear spin in a static magnetic field, $\boldsymbol{B}_0$.

The spin-up state of nuclei in a static magnetic field is lower in energy than the spin-down state, with an energy difference, $\Delta E$, of that shown in equation 1.21, where h is Planck's constant.

$$\Delta E = \mathrm{h}\nu = \frac{\gamma \boldsymbol{B}_0 \mathrm{h}}{2\pi} \tag{1.21}$$

The difference in equilibrium populations of the two energy levels is given by the Boltzmann distribution:

$$\frac{N_{1/2}}{N_{-1/2}} = e^{\Delta E / k_{\mathrm{B}} T} \tag{1.22}$$

$N_{1/2}$ and $N_{-1/2}$ are the populations of spin-up and spin-down states, respectively, $\Delta E$ is the energy difference between the two states, $k_{\mathrm{B}}$ is the Boltzmann constant and $T$ is the temperature. Summation of the contribution from individual spins for an ensemble of spins at thermal equilibrium thus gives an overall macroscopic

magnetisation vector, $\mathbf{M}_0$, which is aligned along the direction of $\boldsymbol{B}_0$. It is the disturbance of $\mathbf{M}_0$ and its return to equilibrium that is utilised in NMR experiments.

### 1.9.2 Radiofrequency pulses

The application of a pulse of radiofrequency (rf) radiation with energy equal to $\Delta E$ results in transitions between the spin-up and spin-down states. The rf pulse redistributes the populations of the spin states whilst simultaneously imposing a torque on the magnetic moments, perpendicular to the direction of the applied field. The net result is deflection of the bulk magnetisation vector, $\mathbf{M}$, by the tip angle, $\theta$. The degree of $\theta$ is determined by the amplitude, $B_1$ and duration, $\tau$ of the rf pulse (equation 1.23):

$$\theta = 2\pi\gamma\tau B_1 \tag{1.23}$$

In a vertical bore magnet, $\boldsymbol{B}_0$ is aligned along the length of the magnet, which is denoted as the $z$-axis, hence $\mathbf{M}_0$ can be denoted as $\mathbf{M}_z$. A 90° rf pulse equalises the populations of spin-up and spin-down states thus eliminating any net magnetisation along the $z$-axis. However, the 90° rf pulse 'bunches' the spins such that they precess from one point of the normal precession route, a property known as phase-coherence, and a net magnetisation appears in the $xy$ (transverse) plane. For example, a $90^{\circ}_{y}$ pulse brings the magnetisation vector down onto the $x$-axis to give $\mathbf{M}_x$ (Figure 1.11). A 180° pulse brings the magnetisation vector onto the $-z$-axis.

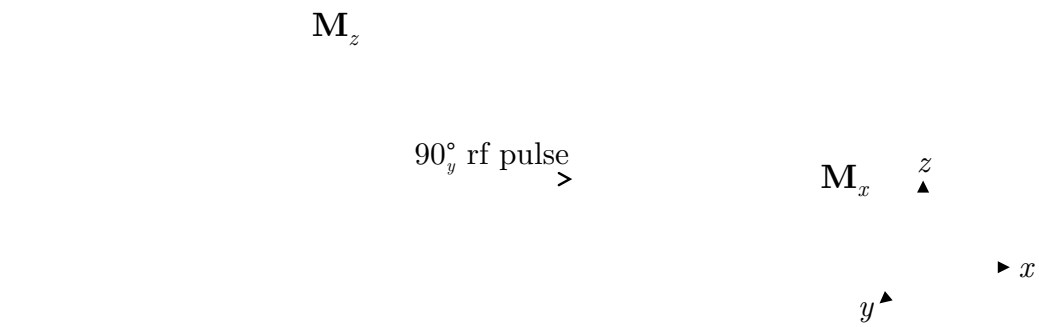


Figure 1.11: A schematic representation of the rotation of the bulk magnetisation vector following the application of a $90^\circ_y$ pulse.

Precession of the transverse magnetisation vector induces an oscillating current in the same rf coil that provided the excitation pulse. This current is detected and forms the NMR signal. Maximum signal arises following a 90° rf pulse; however, there is no signal following a 180° rf pulse as there is not a net magnetisation in the transverse plane. The amplitude of the induced current decays due to relaxation processes, described below, which return the magnetisation vector to its equilibrium position. The NMR signal decay is known as the free induction decay (FID). A Fourier transform converts the FID, which is time-domain data, into the frequency-domain to produce an NMR spectrum or image.

### 1.9.3 Relaxation processes

Following an excitation rf pulse, the system returns to thermal equilibrium via two relaxation processes: $T_1$ (spin-lattice) relaxation and $T_2$ (spin-spin) relaxation; both of these processes are exponential in behaviour. $T_1$ and $T_2$ are the time constants associated with the relaxation processes, respectively.

#### *1.9.3.1 $T_1$ relaxation*

$T_1$ relaxation is the process by which the magnetisation vector returns to the equilibrium value aligned along the $\boldsymbol{B}_0$ axis ($\mathbf{M}_z$). Neighbouring spins generate weak, local magnetic fields that fluctuate due to molecular motion. If fluctuations of the local magnetic field occur at the Larmor frequency, transitions can be induced between the spin states, eventually returning the system to its Boltzmann distribution. The relaxation time is dependent upon the local fluctuations in the magnetic field and thus the most important contribution to $T_1$ relaxation is dipolar coupling. The magnetic fields experienced by neighbouring spins are modulated by the rotational correlation time, $\tau_c$, of the nuclei. The rotational correlation time is a measure of the time taken for a molecule to rotate by one radian[118]; generally, small molecules have short rotational correlation times, whilst large molecules have long rotational correlation times. $T_1$ is inversely proportional to $\tau_c$. The recovery of $\mathbf{M}_z$ from $\mathbf{M}_z = 0$ with respect to time, $t$, is exponential in behaviour and is described by equation 1.24:

$$\mathbf{M}_z = \mathbf{M}_0(1 - e^{-t/T_1}) \qquad (1.24)$$

#### *1.9.3.2 $T_2$ relaxation*

$T_2$ relaxation is the process by which phase-coherence of the precessing spins is lost. For phase-coherence to be maintained each spin must experience the same magnetic field; however, local magnetic fields from neighbouring nuclear spins cause the precessional frequencies of individual spins to differ. The consequence of this is a dephasing of the magnetisation vector in the $xy$ plane, $\mathbf{M}_{xy}$. The decay of $\mathbf{M}_{xy}$ with time, $t$, is exponential in behaviour and is described by equation 1.25, where $\mathbf{M}_{xy}(0)$ is

the initial transverse magnetisation taken at $t = 0$. The time constant for this process, $T_2$, is related to intrinsic properties of the spin system under study.

$$\mathbf{M}_{xy}(t) = \mathbf{M}_{xy}(0)e^{-t/T_2} \tag{1.25}$$

Transverse relaxation is also affected by inhomogeneities in the static magnetic field ($T_{2(\Delta \boldsymbol{B}_0)}$). The homogeneity of $\boldsymbol{B}_0$ can be optimised through a process known as shimming. Here, a set of shim coils through which an electrical current is passed, is used to make fine adjustments of $\boldsymbol{B}_0$. The observed time constant for transverse relaxation, $T_2$*, has contributions from the intrinsic transverse relaxation of the system and the relaxation arising from field inhomogeneities (equation 1.26).

$$\frac{1}{T_2^*} = \frac{1}{T_2} + \frac{1}{T_{2(\Delta \boldsymbol{B}_0)}} \tag{1.26}$$

### 1.9.4 Pulse sequences

A pulse sequence is a set of instructions that controls the various hardware components of the magnetic resonance spectrometer. Pulse sequences are stored as computer programs and coordinate the application of rf pulses, gradient pulses and acquisition. Numerous pulse sequences exist that range in complexity and that are able to manipulate the magnetisation vector to produce a specific form of NMR signal.

#### *1.9.4.1 Pulse-acquire*

The most basic pulse sequence is the pulse-acquire, or 90°-FID sequence. A single 90° pulse is applied to bring the magnetisation vector into the transverse plane and the

resulting FID, induced in the rf coil, is acquired. The Fourier transform of the FID gives a 1-dimensional NMR spectrum. The individual nuclear spins of protons experience different local magnetic fields that are dependent on their chemical environment; this is represented in the NMR spectrum as differing proton resonance frequencies (Hz) or chemical shifts (ppm). Typically, the pulse sequence is repeated multiple times with the phase of the excitation rf pulse and acquisition cycled. Phase cycling is used to suppress 'false' signals that are generated by imperfections in the spectrometer hardware. Multiple signal acquisition also improves the signal-to-noise ratio, where signal adds constructively and noise adds with a square-root dependence. The amplitude of the signal is governed by the spin density, the relaxation rate of the system and the delay, or repetition, time ($T_R$) between acquisition and the consecutive rf pulse.

#### *1.9.4.2 Inversion recovery*

An inversion recovery experiment is commonly used to measure the $T_1$ of a system[120]. A schematic of the pulse sequence is shown in Figure 1.12. An initial 180° generates an inverted spin population distribution and results in a bulk magnetisation vector along the $-z$ axis, $\mathbf{M}_{-z}$. During a delay time $\tau$, the population distribution of spins relaxes back to its equilibrium state and $\mathbf{M}_{-z}$ reduces in magnitude. A 90° pulse is applied to flip the magnetisation vector onto the transverse plane and the signal is acquired.

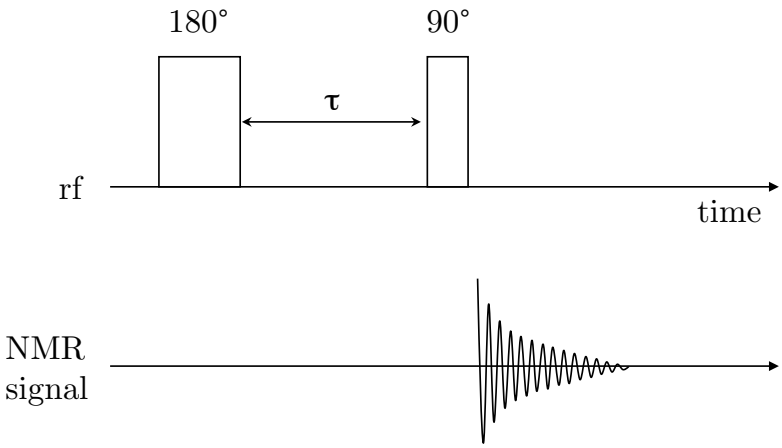

Figure 1.12: Schematic of an inversion recovery pulse sequence.

The amount by which the magnetisation vector returns to its equilibrium magnitude and position, and hence the signal intensity, is dependent on $\tau$. A null point, $\tau_{\text{null}}$, is observed at a $\tau$ value given in 1.27.

$$\tau_{\text{null}} = \ln 2(T_1) \tag{1.27}$$

Typically, a range of delay times is used during an inversion recovery experiment to give a range of signal intensities. A sequence of one-dimensional NMR spectra is acquired. Fitting the peak amplitude of the resonance frequency of interest to equation 1.28 allows $T_1$ to be measured. Equation 1.28 is similar to equation 1.24; however, equation 1.24 describes the recovery of $\mathbf{M}_z$ after saturation and equation 1.28 describes the recovery of $\mathbf{M}_z$ after population inversion.

$$\mathbf{M}_z = \mathbf{M}_0(1 - 2e^{-t/T_1}) \tag{1.28}$$

*1.9.4.3 Spin-echo sequence*

The spin-echo (Hahn echo) sequence[124], shown in Figure 1.13a, can be used to measure transverse relaxation. A $90^{\circ}_{x}$ rf pulse brings the magnetisation vector onto the transverse plane, along the $y$-axis. To explain the behaviour of these spins in the transverse plane the rotating frame of reference will be introduced. In the rotating frame of reference, the $xy$ plane is rotating at a reference frequency. If the reference frequency equals the Larmor frequency the system is referred to as "on-resonance". Thus, following a $90^{\circ}_{x}$ rf pulse the bulk magnetisation vector resides in the transverse plane along the $y$-axis, however, phase-coherency can only be maintained if all spins experience the same magnetic field. Spins begin to dephase due to $T_2$ relaxation processes. This is observable in the rotating frame as some spins precessing faster and some spins precessing slower than the reference frequency. By applying a $180^{\circ}_{y}$ pulse the magnetisation vector is inverted about the $y$-axis, the continuing direction and nature of the spins now acts to regain the previously lost phase coherence. The amplitude of the magnetisation vector and NMR signal subsequently increases. For a spin echo sequence, a number of experiments are performed where the delay time, $\boldsymbol{\tau}$, between the 90° and 180° pulse is incrementally increased. The behaviour of the spins during a spin-echo sequence is illustrated in Figure 1.13b. The amplitude of the acquired NMR signal for each value of $\boldsymbol{\tau}$ is fitted to equation 1.25 to give $T_2$.

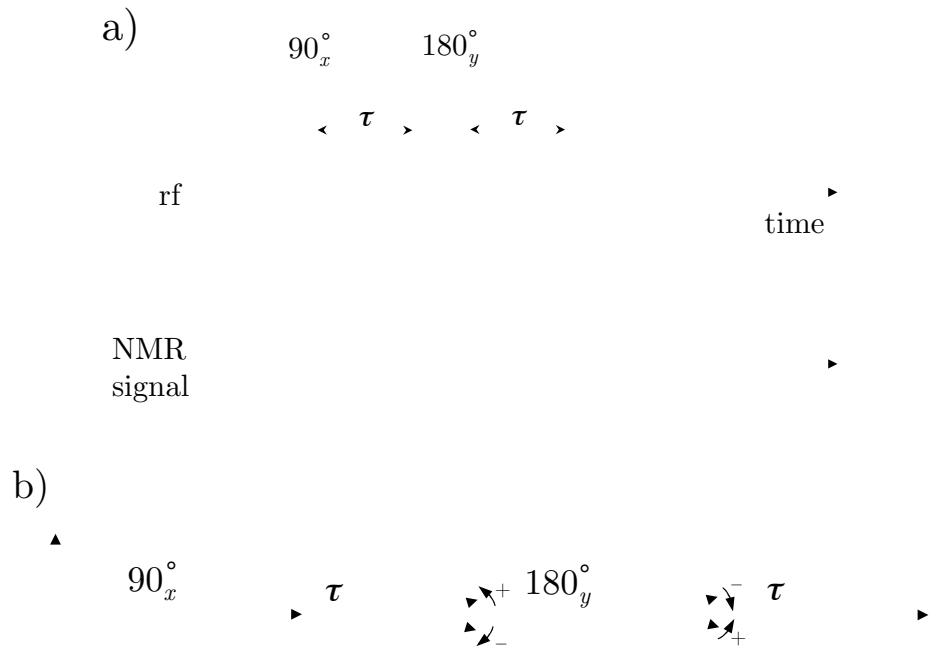


Figure 1.13: a) A spin-echo pulse sequence and b) an illustration of spin behaviour during a spin-echo pulse sequence. A $90^{\circ}_{x}$ rf pulse brings the magnetisation vector onto the transverse plane along the $y$-direction. During a delay time $\tau$, spins experience different local magnetic fields and precess at different frequencies. A $180^{\circ}_{y}$ rf pulse inverts the spins about the $y$-axis and the continued direction and frequency of the spins now serves to refocus them.

#### *1.9.4.4 Carr-Purcell-Meiboom-Gill*

The Hahn echo pulse sequence is susceptible to inhomogeneities in $\boldsymbol{B}_0$. This is because diffusion of nuclei to a region experiencing a slightly different magnetic field can occur, during the course of the experiment. This results in incomplete rephasing of the spins following the 180° pulse and is more pronounced for longer $\tau$. In this case, $T_2^*$ is measured and not the intrinsic $T_2$ of the sample. To minimise the effects of diffusion, a Carr-Purcell-Meiboom-Gill (CPMG)[125, 126] sequence can be adopted. The CPMG sequence uses multiple $180^{\circ}_{y}$ pulses with a delay time, $\tau$, that is held constant (Figure 1.14). The pulse sequence is repeated a number of times and the number of 180° pulses prior to signal acquisition varied. This produces spectral data

and keeps $\boldsymbol{\tau}$ short. As for the spin-echo sequence, the peak amplitude of the signal is fitted to equation 1.25 to give $T_2$. The amplitude and decay of successive echoes, acquired following the 180° refocusing pulses, gives the intrinsic $T_2$ of the system.

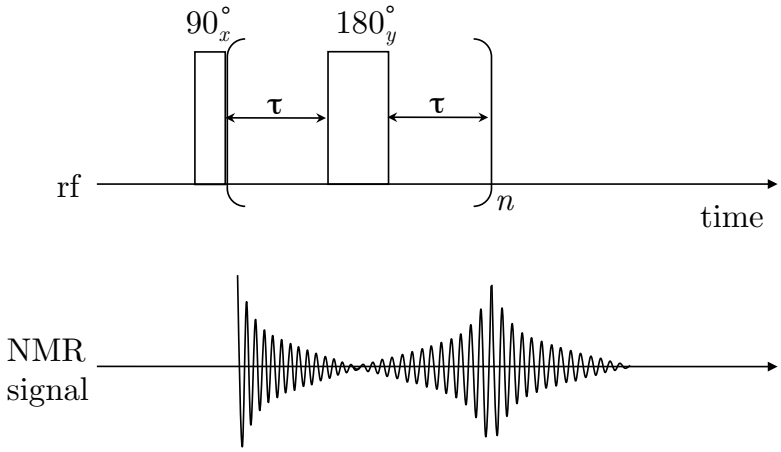


Figure 1.14: Schematic of a CPMG pulse sequence.

### 1.9.5 Magnetic field gradients

Magnetic field gradients can be applied such that the static magnetic field, $\boldsymbol{B}_0$, is no longer homogeneous. The static magnetic field varies linearly in the direction of the applied gradient causing the spins of nuclei experiencing a higher magnetic field to precess faster than those experiencing a lesser magnetic field; the Larmor frequency at which the nuclei now precess is spatially dependent and defined as:

$$\omega(\boldsymbol{r}) = \gamma \boldsymbol{B}_0 + \gamma \boldsymbol{G} \bullet \boldsymbol{r} \tag{1.29}$$

where $\boldsymbol{G}$ is the magnetic gradient component and $\boldsymbol{r}$ is the position in a given direction $x$, $y$, $z$. The application of a linear gradient causes a helix of phase of the precessing nuclear spins to be wound (Figure 1.15).

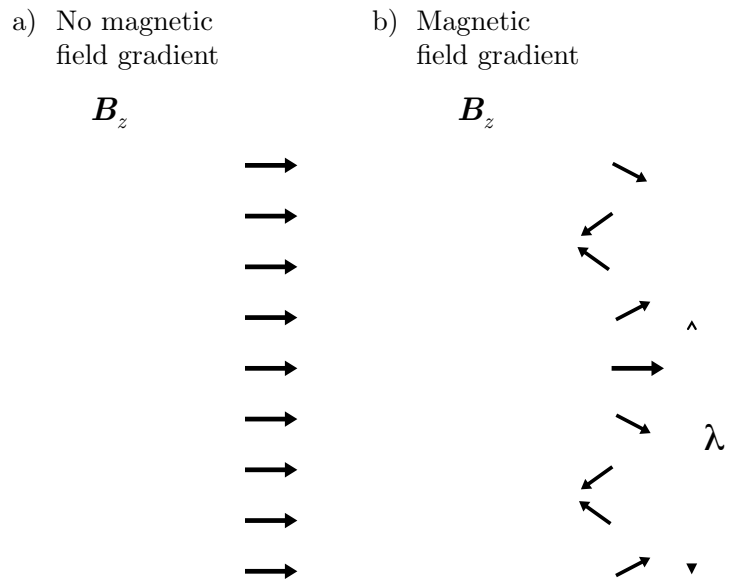


Figure 1.15: An illustration of nuclear spins following a 90° pulse; a) with no applied magnetic field gradient, thus exhibiting phase coherence and b) with a linear magnetic field gradient applied (here denoted in the *z*-direction), thus a helix of phase is wound. The wavelength, λ, of the helix of phase is shown.

The wavelength of the helix, λ, is the length over which a 360° phase shift occurs and is dependent on the duration of the gradient, $t$, and the gradient strength, $\boldsymbol{G}$ (equation 1.30). $\boldsymbol{k}$ is the reciprocal space vector (equation 1.31).

$$\boldsymbol{k} = \frac{\gamma \boldsymbol{G} t}{2\pi} \tag{1.30}$$

$$\boldsymbol{k} = \frac{1}{\lambda} \tag{1.31}$$

Magnetic field gradients can be applied in the $x$, $y$ and $z$ directions and can be applied along 1, 2 or 3 directions. It is this that allows for 2- and 3-dimensional images to be acquired.

*1.9.5.1 Pulsed Gradient Spin Echo sequence*

The pulsed gradient spin echo sequence (PGSE) is a modification of the spin echo sequence that uses magnetic field gradients and allows translational motion to be measured[127, 128]. A schematic of the pulse sequence is shown in Figure 1.16

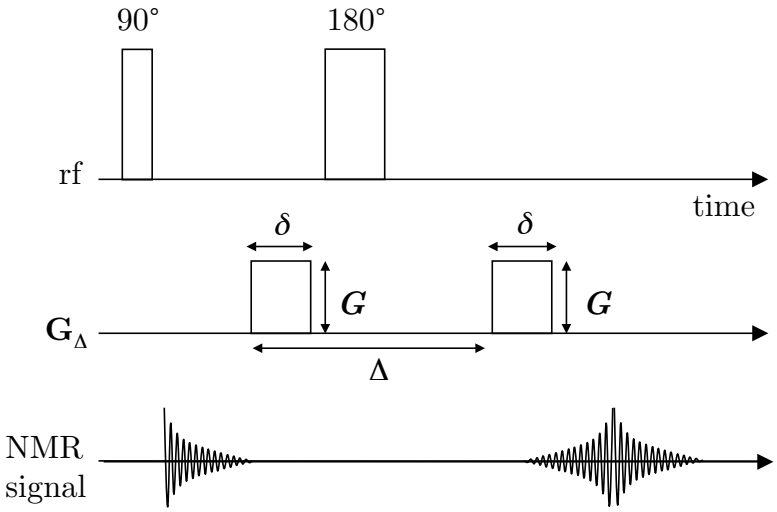


Figure 1.16: A schematic of a PGSE experiment.

An initial 90° pulse is applied that brings the magnetisation vector onto the transverse plane and the first of two gradient pulses is applied for a duration denoted $\delta$. The gradient pulse causes nuclei to precess at different frequencies, depending on their position in the pulsed magnetic field. Once the gradient pulse is off, the nuclei will precess at the same frequency but with different phases. A 180° pulse is then applied that flips the magnetisation vector about the transverse plane and the second gradient pulse applied. This pulse serves to refocus the magnetisation; if any translational motion of the nuclei has occurred between gradient pulses, the magnetisation vector will not be fully refocused and a phase shift, $\varphi$, will be observed (equation 1.32).

$$\varphi = \gamma \boldsymbol{G}_{\boldsymbol{\Delta}} \delta \Delta(\mathbf{R}) \tag{1.32}$$

$\boldsymbol{G}_{\boldsymbol{\Delta}}$ is the amplitude of the two gradient pulses, $\Delta$ is the time difference between the gradient pulses and $\mathbf{R}$ is the displacement of the spins. Coherent translational motion, i.e. flow, will cause a shift in the phase proportional to the velocity of flow. Random translational motion, i.e. diffusion, results in a range of phases and subsequent attenuation of the acquired signal. This attenuation is dependent upon $\gamma$, $\mathbf{G}_{\boldsymbol{\Delta}}$, $\delta$, $\Delta$ and the diffusion coefficient of the nuclei, $D$. Application of the Stejskal-Tanner relationship[127] (equation 1.33) to the measured signal intensity, $I$, and measured signal intensity at $\mathbf{G}_{\boldsymbol{\Delta}} = 0$, $I_0$, of the PGSE experiment, gives the value of $D$.

$$\frac{\mathrm{I}}{\mathrm{I}_0} = \exp[-\gamma^2 \delta^2 \mathbf{G}_{\boldsymbol{\Delta}}^2 D(\Delta - \frac{\delta}{3})] \tag{1.33}$$

### 1.9.6 Principles of magnetic resonance imaging

#### *1.9.6.1 Frequency and phase encoding*

The use of magnetic field gradients causes the precessional frequencies of nuclei to be dependent upon their position along the applied gradient, thus providing spatial information. Typically, two methods are employed to encode the spatial information in MRI; these are frequency and phase encoding. In frequency encoding, a magnetic field gradient is applied during the acquisition of the NMR signal, causing spins at different positions along the gradient to precess at varying frequencies. The gradient is kept constant during acquisition and signal is acquired. A Fourier transformation

of the NMR signal results in a frequency-domain spectrum that contains a range of frequencies; the signal intensity is proportional to the number of spins at a particular frequency. For a one-dimensional frequency encoded experiment where a single frequency encoding gradient is applied along the $x$-axis, the resultant spectrum is a one-dimensional profile of all the spins in the $z$- and $y$-axes projected onto the $x$-axis (Figure 1.17).

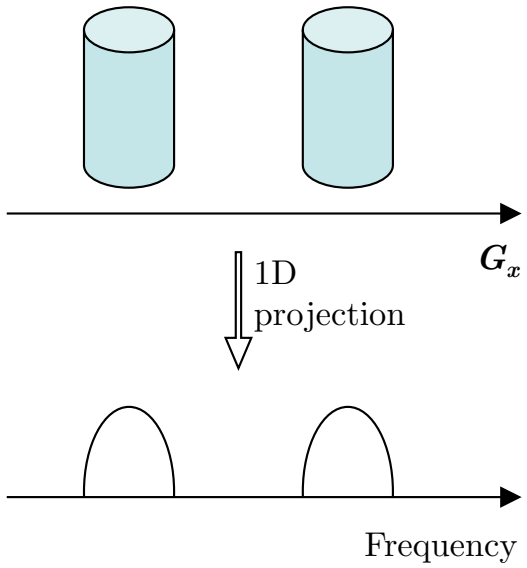


Figure 1.17: One-dimensional frequency encoding spin density profile of two tubes containing, for example, water. A frequency encoding gradient is applied along a single axis, $x$. The resultant spectrum is a projection of all spins in the $z$- and $y$ axes projected onto the $x$-axis.

In phase encoding, a magnetic field gradient is applied for a fixed period of time prior to signal acquisition and switched off as the signal is acquired. Again, the application of the magnetic field gradient causes spins to precess at different frequencies, depending on their position along the gradient. However, when the gradient is switched off, all spins have an identical precessional frequency but they are now

phase shifted as a consequence of their previously different precessional frequencies. The phase shift of the spins is dependent upon their position and the phase angle, $\varphi$, of the shift at a position $\boldsymbol{r}$ along the phase encoded axis is given by equation 1.34, where $\boldsymbol{G}_{\mathrm{PE}}$ is the amplitude of the phase encoding gradient and $t$ is the duration of the gradient. Phase encoding requires multiple excitation pulses to be applied (discussed further in section 1.9.6.3 below) whereby the gradient strength is increased in units of $\Delta\boldsymbol{G}_{\mathrm{PE}}$ for each. Spatial information in the phase-encoded direction is encoded in the value of the phase shift.

$$\varphi = \gamma\Delta\boldsymbol{G}_{\mathrm{PE}}t\boldsymbol{r} \tag{1.34}$$

A combination of frequency and phase encoding is used in MR imaging experiments and can produce two- and three-dimensional images.

#### *1.9.6.2 Slice selection*

Slice selection in MRI is the selection of spins in a plane through the sample of interest. Slice selection thus allows for two-dimensional images to be produced, which can represent horizontal or vertical planes through the sample (Figure 1.18). Slice selection is achieved by simultaneously applying a magnetic field gradient and a 90° or 180° rf pulse. The bandwidth of frequencies excited by a rf pulse is inversely proportional to the duration of the pulse and thus a soft frequency selective rf pulse is used. The magnetic field gradient pulse causes nuclei to precess with different frequencies whilst the application of a soft frequency selective rf pulse causes the excitation of only those spins within a narrow range of frequencies. Multiple slices can be excited sequentially through different spatial locations of the sample.

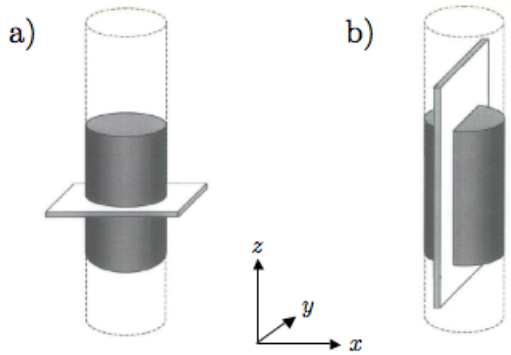


Figure 1.18: Schematic to illustrate a) horizontal and b) vertical slice selection through a cylindrical sample. The shaded region is the observable region of the rf coil. The slice length and width is the field-of-view.

#### *1.9.6.3 k-space*

In 2D MR imaging the 2D data that are acquired from a combination of frequency and phase encoding are stored in a spatial frequency domain known as *k*-space (reciprocal space). The subsequent reconstruction of the data using a 2D Fourier transformation produces an MR image. *k*-space is defined by the *k*-space vectors $\boldsymbol{k}_x$, $\boldsymbol{k}_y$ and (for 3-D images) $\boldsymbol{k}_z$. Figure 1.19 shows a *k*-space raster for a two-dimensional 8 × 8 matrix with a frequency encoded *x*-direction and a phase encoded *y*-direction. A *k*-space raster is a representation of the data points acquired for a 2D image and has the same number of points as the number of pixels in the image.

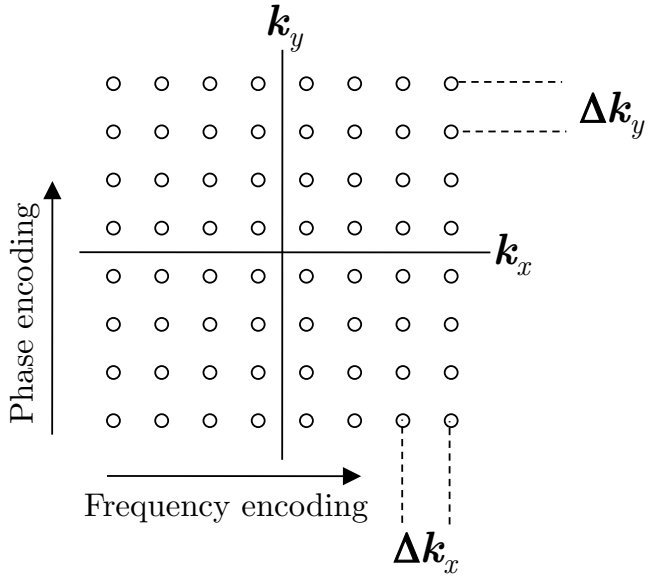


Figure 1.19: A two-dimensional $k$-space raster for an 8 × 8 matrix selected about the $z$-axis. Frequency encoding is along the $x$-direction and phase encoding is achieved along the $y$-direction.

The $k$-space raster can be traversed by applying phase and frequency gradients (the origin of $k$-space is $\boldsymbol{k}_x = \boldsymbol{k}_y = 0$). $\boldsymbol{k}_x$ is traversed in time through the application of a frequency encoding gradient. The $k$-space sampling interval in the $x$-direction, $\Delta\boldsymbol{k}_x$, is given by equation 1.35 where $\Delta t$ is the sampling interval of the FID. For a complete line to be read in the frequency encoded direction it is necessary to traverse negative values of $\boldsymbol{k}_x$, this is achieved by applying a negative pre-cursor gradient prior to the positive read gradient.

$$\Delta k_x = \frac{\gamma \boldsymbol{G}_x \Delta t}{2\pi} \tag{1.35}$$

$\boldsymbol{k}_y$ is traversed through the application of successive phase encoding gradients where the strength of the gradients is incremented. The $k$-space sampling interval in the $y$-

direction, $\Delta \boldsymbol{k}_y$, is given by equation 1.36 where $\Delta \boldsymbol{G}_y$ is the phase encoding step size and $t$ is the duration of the phase encoding gradient.

$$\Delta k_y = \frac{\gamma \Delta \boldsymbol{G}_y t}{2\pi} \tag{1.36}$$

Typically, each horizontal line in the raster is acquired for a single excitation and "read" during signal acquisition; the frequency encoded direction is thus often termed the read direction. Since the frequency encoding gradient is on during acquisition, only one direction can be frequency encoded. Spatial encoding in the second dimension is acheived using phase encoding gradients. Each horizontal line in the $k$-space raster requires a different phase encoding gradient strength, therefore, for each horizontal line that is read a separate excitation is required.

#### *1.9.6.4 Resolution and field-of-view*

Image resolution determines the size of spatial features that are discernable; a higher resolution reflects that smaller features can be resolved. Spatial resolution in MR imaging experiments is determined by the $k$-space sampling intervals and the number of data points, $n$, that are sampled in the $k$-space raster. Equation 1.37 gives the spatial resolution of frequency encoding ($1/\Delta x$) and equation 1.38 gives the spatial resolution of phase encoding ($1/\Delta y$):

$$\frac{1}{\Delta x} = n_x \Delta \boldsymbol{k}_x = \boldsymbol{k}_{x,\max} \tag{1.37}$$

$$\frac{1}{\Delta y} = n_y \Delta \boldsymbol{k}_y = \boldsymbol{k}_{y,\max} \tag{1.38}$$

Spatial resolution in the frequency encoding direction is limited by the NMR linewdith, $\Delta\nu$ (equation 1.39):

$$\frac{1}{|\Delta x|} = \left|\frac{\gamma \boldsymbol{G}_x}{2\pi\Delta\nu}\right| \tag{1.39}$$

The field-of-view (FOV) gives the maximum spatial distance that can be imaged and is dependent on the $k$-space sampling interval $\Delta k$. Image artefacts can arise if the FOV is not appropriate for the sample that is being investigated.

#### *1.9.6.5 Experiment time*

The length of time that an MRI experiment takes is determined by the experimental parameters that are used to investigate the system of interest. An approximation of the experiment time is given in equation 1.40 where $T_{\mathrm{R}}$ is the repetition time (i.e. the time between successive excitation pulses for a given pulse sequence), $n_{\mathrm{PE}}$ is the number of phase encoding pixels (number of horizontal lines in the $k$-space raster) and $n_{\mathrm{rep}}$ is the number of repetitions of the pulse sequence.

$$\text{Experiment time} = n_{\mathrm{PE}} \times T_{\mathrm{R}} \times n_{\mathrm{rep}} \tag{1.40}$$

### 1.9.7 Magnetic resonance imaging pulse sequences

#### *1.9.7.1 Spin-echo imaging*

The spin-echo imaging sequence is based on the spin-echo pulse sequence discussed in section 1.9.4.3 but uses additional slice selection and frequency and phase encoding gradients to spatially encode the NMR signal. A schematic of a 2-dimensional spin-

echo imaging pulse sequence is shown in Figure 1.20. An initial soft 90° pulse is used in conjunction with a magnetic field gradient in the $z$-direction to allow for slice selection within the sample. A negative slice gradient can be seen which acts to refocus the spins. A phase encoding gradient is then applied and is represented as a segmented box to illustrate that the gradient is stepped with each repeat of the sequence. This phase encoding gradient spatially encodes the spins in the $y$-direction. A hard 180° rf pulse is then applied that produces a spin-echo. A negative read precursor gradient is applied to allow for a complete line of $k$-space to be sampled, followed by a positive read gradient that refocuses the spins thus forming the spin-echo. The signal is acquired during the application of the positive read gradient.

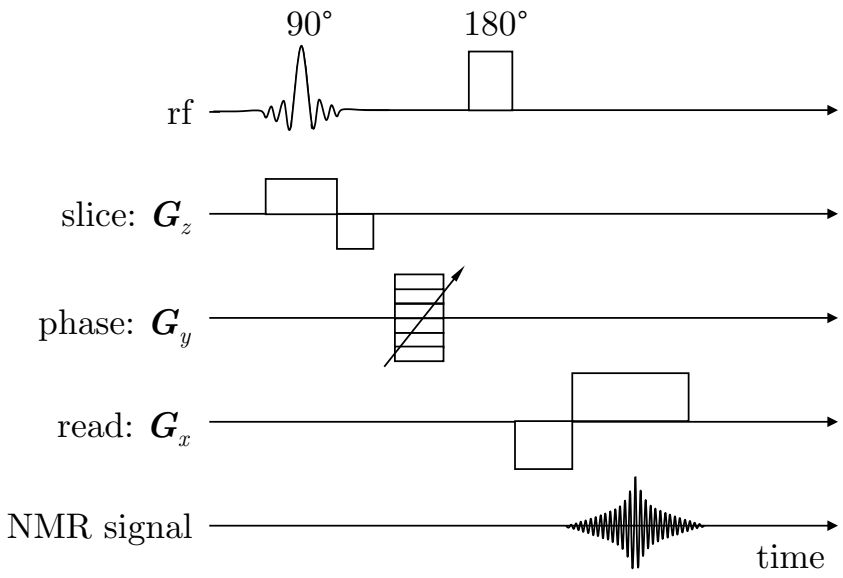


Figure 1.20: A schematic of a 2-dimensional spin-echo imaging pulse sequence.

#### *1.9.7.2 RARE imaging*

Rapid acquisition with relaxation enhancement (RARE)[129] imaging is a modification of the spin-echo imaging that is used to reduce the experiment time. A schematic of

the sequence is shown in Figure 1.21. In the RARE imaging sequence, spins are refocused and a spin-echo is produced a number of times, $n$, per excitation. This allows for multiple lines of $k$-space to be collected for a single excitation. The number of echoes acquired per excitation is often termed the RARE factor. The larger the RARE factor the shorter the experiment time (equation 1.41)

$$\text{Experiment time} = \left( \frac{n_{\text{PE}}}{\text{RARE factor}} \right) \times T_{\text{R}} \times n_{\text{rep}} \tag{1.41}$$

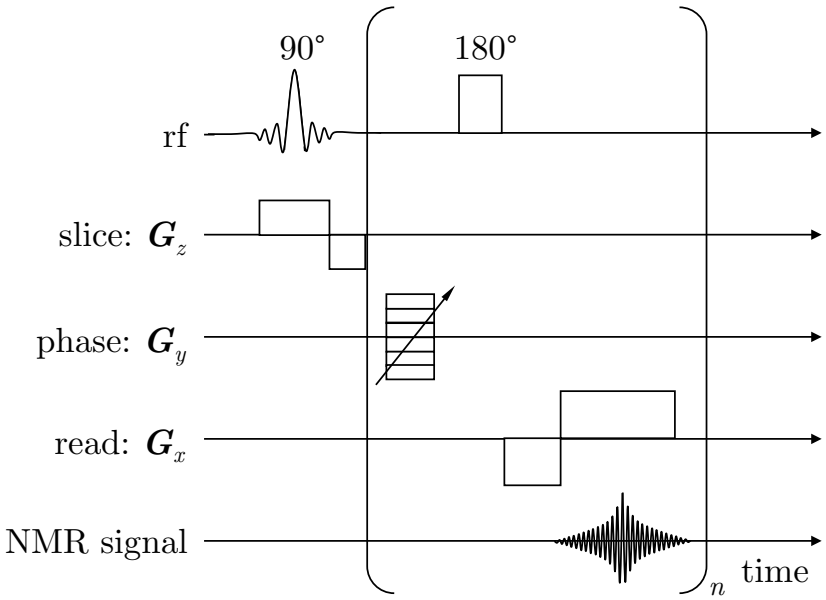


Figure 1.21: A schematic of a 2-dimensional RARE imaging pulse sequence that acquires $n$ echoes per 90° excitation rf pulse.

### 1.9.8 Contrast in MRI

Magnetic resonance imaging is used to distinguish between regions of different chemical and physical composition; for this to be achieved, contrast is required between these regions. Contrast in MRI arises from the variation in signal intensity between neighbouring voxels to which there are three main contributors:

*i) spin density*

*ii) relaxation times*

*iii) chemical shift*

#### *1.9.8.2 Spin density contrast*

The signal intensity acquired during a spin echo experiment can be used to produce spin density images of a system. The signal intensity, $a_{SE}$, at a point $\mathbf{r}$, is given by:

$$\mathrm{a_{SE}}(\mathbf{r}, T_\mathrm{R}, T_\mathrm{E}) = \mathbf{M}_0(\mathbf{r})\left[1 - \exp\left(-\frac{T_\mathrm{R}}{T_1(\mathbf{r})}\right)\right]\exp\left(-\frac{T_\mathrm{E}}{T_2(\mathbf{r})}\right) \qquad (1.42)$$

To ensure that the contrast obtained is based solely on spin density, experimental parameters must be set to exclude the effect of, for instance, relaxation of the system. This is achieved by ensuring an experimental echo time ($T_\mathrm{E}$) that is shorter than the $T_2$ relaxation time of the system, and a repetition time ($T_\mathrm{R}$), that is five times the $T_1$ relaxation time of the system, allowing complete return of the equilibrium magnetisation vector, $\mathbf{M}_0$.

#### *1.9.8.3 Relaxation time contrast*

Enhanced image contrast can be achieved by using experimental parameters that exploit differences in relaxation times within the sample. The signal intensities will

still have contributions that arise from the spin density but the images are now said to be parameter-weighted. $T_1$-weighted contrast is achieved by using a short echo time that suppresses spin-spin relaxation effects, and a repetition time that is comparable to the $T_1$ of the system ($T_R \leq T_1$). Decreasing the repetition time between excitation pulses results in excitation of a system that has not fully relaxed. Consequently, with each successive 90° pulse a magnetisation vector of a lesser magnitude is brought onto the transverse plane. The summation of signal acquisition from successive repetitions will be greater for spins that have fully relaxed, i.e. spins that have a short $T_1$, compared to that of spins with a long $T_1$. This results in areas that have a shorter $T_1$ appearing as brighter/higher intensity regions of the image. $T_2$-weighted imaging is achieved by ensuring the repetition time is sufficient to allow full spin-lattice relaxation, thus rendering the effects of $T_1$ negligible, and extending the echo time so that it becomes significant compared to the $T_2$ of the system. A short $T_2$ results in a loss of phase coherence of the precessing nuclei and a subsequent reduction of $\mathbf{M}_{xy}$. Thus, regions of the sample that contain nuclei with a short $T_2$ appear as darker regions of the image.

Paramagnetic contrast agents are commonly used to enhance relaxation time contrast in MR images[130-133]. The high magnetic moments of paramagnetic metal ions have the effect of enhancing the local magnetic fields that fluctuate in the vicinity of proton nuclei (usually, and for the purpose of this discussion, those nuclei of solvent water). Consequently, spin-lattice and spin-spin relaxation processes are enhanced and the time constants, $T_1$ and $T_2$, associated with these processes reduced. The greater fractional decrease in $T_1$ dominates the relaxation effects and generates signal enhancement of areas where fast spin-lattice relaxation occurs. The

ability of the paramagnetic species to increase the relaxation rate of the surrounding proton spins is termed its relaxivity. This relaxivity is affected by the interactions of the paramagnetic metal species with solvent nuclei and is dependent upon the total nuclear spin of the metal ion, the distance of the proton to the paramagnetic metal ion and the rotational correlation time. The amount of paramagnetic species present in a system has an inversely proportional effect on the relaxation time.

#### *1.9.8.4 Chemical shift contrast*

Nuclei that are in different chemical environments precess at different frequencies, i.e. they have different chemical shifts, and it is this that makes chemical shift contrast possible. Chemical shift contrast can be achieved when a soft, frequency selective pulse is used to excite only spins within a narrow range of frequencies. These spins can either be suppressed prior to the use of an imaging sequence such that they will not contribute to the acquired signal intensity[134, 135] or, conversely, an imaging sequence can be used whereby signal arises only from the spin densities of those nuclei that have been excited[120].

### 1.9.9 CHESS imaging

Chemical shift selective (CHESS) imaging is used to provide contrast between nuclear spins that have different precessional frequencies[120, 135]. A schematic of a CHESS imaging pulse sequence is shown in Figure 1.22.

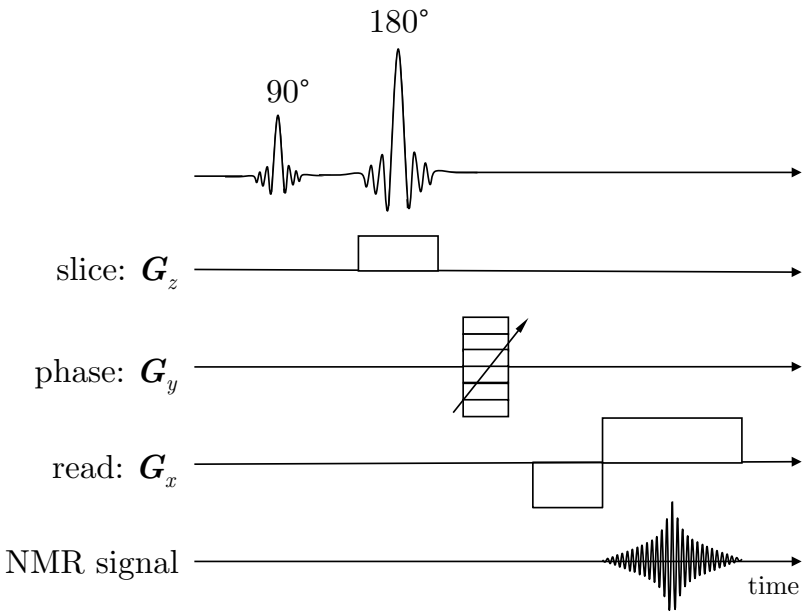


Figure 1.22: A schematic of a 2-dimensional CHESS imaging pulse sequence. The 90° rf pulse is a chemical shift selective pulse and the 180° rf pulse is used for slice selection.

In this sequence, two frequency selective soft pulses are used. The first soft 90° pulse is used in the absence of a slice selective gradient, and acts to excite only those spins with a particular chemical shift. The pulse bandwidth is inversely proportional to the pulse duration and so the selective excitement of a narrow range of frequencies, corresponding to a narrow range of chemical shifts, requires that a long pulse duration is used. This subsequently results in a longer minimum $T_{\mathrm{E}}$. The second rf pulse is now the slice selective pulse and, to this effect, is applied during the slice selection gradient. The acquisition of $k$-space data is achieved by using frequency and phase encoding gradients as with the spin-echo and RARE imaging sequences.

## 1.10Dynamic light scattering

Dynamic light scattering (DLS) is a commonly used technique for determining the droplet size of micelles in microemulsion systems[136, 137]. DLS, which is also referred to as Photon Correlation Spectroscopy (PCS), measures the Brownian motion of particles, by observing the signal intensity of scattered light as a function of time. The scattering intensity of a particle is proportional to $d^6$, where $d$ is the diameter of the particle. Scattered light from larger particles therefore dominates the measured intensity of scattered light. For this reason, DLS is not suitable for analysis of polydisperse particles. The signal intensity is fitted to an auto-correlation function. For particles that diffuse slowly, there is a strong correlation between the initial signal intensity and the measured signal intensity at a short time later. Conversely, for rapidly diffusing particles, the correlation decays more rapidly. Equation 1.43[138] gives the intensity auto-correlation function $G_2(\tau)$ for Brownian motion of monodisperse particles.

$$G_2(\tau) = A + B \exp(-2\Gamma \tau) \tag{1.43}$$

A and B are instrumental factors relating to the intercept and baseline of the correlation function and $\tau$ is the delay time. $\Gamma$ is the rate of decay and is related to the diffusion coefficient $D$ of the particle. The hydrodynamic radius, $R$, can then be determined from the diffusion coefficient using the Stokes-Einstein relationship:

$$D = \frac{k_B T}{6\pi\eta R} \tag{1.44}$$

where $k_B$ is the Boltzmann constant, $T$ is the temperature and $\eta$ is the viscosity of the solvent.

## 1.11References


[1] P. Ball, *The self-made tapestry: pattern formation in nature*, Oxford University Press, Oxford [England] ; New York, **1999**.

[2] J. J. Tyson, J. P. Keener, *Physica D* **1988**, *32*, 327.

[3] I. R. Epstein, J. A. Pojman, *An introduction to nonlinear chemical dynamics : oscillations, waves, patterns, and chaos*, Oxford University Press, New York, **1998**.

[4] I. R. Epstein, K. Showalter, *The Journal of Physical Chemistry* **1996**, *100*, 13132.

[5] V. Volpert, S. Petrovskii, *Physics of Life Reviews* **2009**, *6*, 267.

[6] F. Sagues, I. R. Epstein, *Dalton Transactions* **2003**, 1201.

[7] P. Grindrod, B. D. Sleeman, *Journal of Mathematical Biology* **1985**, *23*, 119.

[8] R. Luther, *Zeitschrift Fur Elektrochemie Und Angewandte Physikalische Chemie* **1906**, *12*, 596.

[9] R. Luther, *Journal of Chemical Education* **1987**, *64*, 740.

[10] A. N. Zaikin, Zhabotin.Am, *Nature* **1970**, *225*, 535.

[11] W. C. Bray, Journal Of The American Chemical Society **1921**, *43*, 1262.

[12] A. T. Winfree, *Journal of Chemical Education* **1984**, *61*, 661.

[13] I. N. Levine, *Physical chemistry*, 5th ed., McGraw-Hill, Boston, **2002**.

[14] R. M. Noyes, R. J. Field, E. Koros, *Journal Of The American Chemical Society* **1972**, *94*, 1394.

[15] R. J. Field, R. M. Noyes, E. Koros, *Journal Of The American Chemical Society* **1972**, *94*, 8649.

[16] M. Hauser, Picture Gallery, Department of Physics, Otto-von-Guericke University Madgeburg **2009**.

[17] D. A. Binks, *PhD Thesis* University of Birmingham, School of Chemistry, **2009**.

[18] E. C. Edblom, Y. Luo, M. Orban, K. Kustin, I. R. Epstein, *Journal of Physical Chemistry* **1989**, *93*, 2722.

[19] R. D. Faria, I. R. Epstein, K. Kustin, *Journal Of The American Chemical Society* **1992**, *114*, 7164.

[20] J. Harrison, K. Showalter, *Journal Of Physical Chemistry* **1986**, *90*, 225.

[21] A. K. Horvath, Journal Of Physical Chemistry A **2005**, *109*, 5124.

[22] I. Nagypal, I. R. Epstein, *Journal Of Physical Chemistry* **1986**, *90*, 6285.

[23] L. Szirovicza, I. Nagypal, E. Boga, *Journal Of The American Chemical Society* **1989**, *111*, 2842.

[24] S. Sanchez-Armass, S. R. Sennoune, D. Maiti, F. Ortega, R. Martinez-Zaguilan, *American Journal of Physiology-Cell Physiology* **2006**, *290*, C524.

[25] A. A. Bulychev, S. V. Zykov, A. B. Rubin, S. C. Muller, *European Biophysics Journal with Biophysics Letters* **2003**, *32*, 144.

[26] V. Castets, E. Dulos, J. Boissonade, P. Dekepper, *Physical Review Letters* **1990**, *64*, 2953.

[27] T. Yamaguchi, L. Kuhnert, Z. Nagyungvarai, S. C. Muller, B. Hess, *Journal Of Physical Chemistry* **1991**, *95*, 5831.

[28] R. E. McIlwaine, H. Fenton, S. K. Scott, A. F. Taylor, *Journal of Physical Chemistry C* **2008**, *112*, 2499.

[29] I. R. Epstein, V. K. Vanag, *Chaos* **2005**, *15*.

[30] A. M. Turing, Philosophical Transactions of the Royal Society of London Series B-Biological Sciences **1952**, *237*, 37.

[31] S. K. Scott, *Oscillations, waves, and chaos in chemical kinetics*, Oxford University Press, Oxford ; New York, **1994**.

[32] C. R. Chinake, R. H. Simoyi, *Journal Of Physical Chemistry* **1996**, *100*, 1643.

[33] G. Rabai, M. T. Beck, *Inorganic Chemistry* **1987**, *26*, 1195.

[34] P. Jones, K. B. Oldham, *Journal of Chemical Education* **1963**, *40*, 366.

[35] G. Rabai, A. Kaminaga, I. Hanazaki, *Journal of Physical Chemistry* **1996**, *100*, 16441.

[36] R. A. Fisher, *Annals of Eugenics* **1937**, *7*, 355.

[37] A. Kolmogorov, I. Petrovsky, N. Piscounoff, *Bull. Univ. Moscow Ser. Int., Sec. A* **1937**.

[38] S. J. DiBartolo, A. T. Dorsey, *Physical Review Letters* **1996**, *77*, 4442.

[39] D. Panja, *Physics Reports* **2004**, *393*, 87.

[40] S. Anita, V. Capasso, Mathematical Methods in the Applied Sciences, *33*, 1235.

[41] P. Dekepper, I. R. Epstein, K. Kustin, M. Orban, *Journal Of Physical Chemistry* **1982**, *86*, 170.

[42] D. M. Weitz, I. R. Epstein, *Journal Of Physical Chemistry* **1984**, *88*, 5300.

[43] A. Keresztessy, I. P. Nagy, G. Bazsa, J. A. Pojman, *Journal Of Physical Chemistry* **1995**, *99*, 5379.

[44] R. H. Simoyi, J. Masere, C. Muzimbaranda, M. Manyonda, S. Dube, *International Journal Of Chemical Kinetics* **1991**, *23*, 419.

[45] A. Toth, D. Horvath, A. Siska, Journal of the Chemical Society-Faraday Transactions **1997**, *93*, 73.

[46] G. Bazsa, I. R. Epstein, *The Journal of Physical Chemistry* **1985**, *89*, 3050.

[47] S. K. Scott, K. Showalter, *The Journal of Physical Chemistry* **1992**, *96*, 8702.

[48] T. G. Szanto, G. Rabai, *Journal of Physical Chemistry A* **2005**, *109*, 5398.

[49] I. Hanazaki, G. Rabai, *Journal of Chemical Physics* **1996**, *105*, 9912.

[50] R. E. McIlwaine, *PhD Thesis*, University of Leeds, School of Chemistry, **2007**.

[51] I. Nagypal, I. R. Epstein, *Journal Of Chemical Physics* **1988**, *89*, 6925.

[52] V. K. Vanag, M. V. Alfimov, *Journal Of Physical Chemistry* **1993**, *97*, 1884.

[53] A. K. Dutt, M. Menzinger, *Journal Of Physical Chemistry* **1992**, *96*, 8447.

[54] V. K. Vanag, D. P. Melikhov, *Journal Of Physical Chemistry* **1995**, *99*, 17372.

[55] J. A. Pojman, I. R. Epstein, T. J. McManus, K. Showalter, *The Journal of Physical Chemistry* **1991**, *95*, 1299.

[56] J. A. Pojman, I. R. Epstein, *Journal Of Physical Chemistry* **1990**, *94*, 4966.

[57] J. D'Hernoncourt, A. Zebib, A. De Wit, *Chaos* **2007**, *17*, 9.

[58] B. K. Paul, S. P. Moulik, *Current Science* **2001**, *80*, 990.

[59] A. Kogan, N. Garti, Advances in Colloid and Interface Science **2006**, *123*, 369.

[60] V. C. Santanna, F. D. S. Curbelo, T. N. C. Dantas, A. A. D. Neto, H. S. Albuquerque, A. I. C. Garnica, *Journal of Petroleum Science and Engineering* **2009**, *66*, 117.

[61] B. Baruah, J. M. Roden, M. Sedgwick, N. M. Correa, D. C. Crans, N. E. Levinger, *Journal of the American Chemical Society* **2006**, *128*, 12758.

[62] J. H. Fendler, *Accounts of Chemical Research* **1976**, *9*, 153.

[63] R. Bru, A. Sanchezferrer, F. Garciacarmona, *Biochemical Journal* **1995**, *310*, 721.

[64] R. Cooke, I. D. Kuntz, Annual Review of Biophysics and Bioengineering **1974**, *3*, 95.

[65] J. S. Clegg, *Journal of Cell Biology* **1984**, *99*, S167.

[66] F. M. Menger, K. Yamada, Journal of the American Chemical Society **1979**, *101*, 6731.

[67] Y. Miyake, Colloids And Surfaces A-Physicochemical And Engineering Aspects **1996**, *109*, 255.

[68] G. Hedstrom, J. P. Slotte, O. Molander, J. B. Rosenholm, *Biotechnology and Bioengineering* **1992**, *39*, 218.

[69] K. Bhattacharyya, *Accounts of Chemical Research* **2003**, *36*, 95.

[70] B. Boyer, G. Lamaty, F. Mary, J. Mouanga, J. P. Roque, *New Journal of Chemistry* **1992**, *16*, 375.

[71] N. Nandi, K. Bhattacharyya, B. Bagchi, *Chemical Reviews* **2000**, *100*, 2013.

[72] M. Bourrel, R. S. Schechter, Microemulsions and related systems: formulation, solvency, and physical properties, M. Dekker, New York, **1988**.

[73] J. H. Clint, *Surfactant aggregation*, Blackie; Chapman and Hall, Glasgow New York, **1992**.

[74] T. K. De, A. Maitra, Advances In Colloid And Interface Science **1995**, *59*, 95.

[75] K. Bhattacharyya, B. Bagchi, *Journal of Physical Chemistry A* **2000**, *104*, 10603.

[76] V. K. Vanag, *Physics-Uspekhi* **2004**, *47*, 923.

[77] H. MacDonald, B. Bedwell, E. Gulari, *Langmuir* **1986**, *2*, 704.

[78] G. Onori, A. Santucci, *The Journal of Physical Chemistry* **1993**, *97*, 5430.

[79] P. R. Majhi, S. P. Moulik, *The Journal of Physical Chemistry B* **1999**, *103*, 5977.

[80] M. Wong, J. K. Thomas, T. Nowak, *Journal of the American Chemical Society* **1977**, *99*, 4730.

[81] F. M. Menger, G. Saito, Journal of the American Chemical Society **1978**, *100*, 4376.

[82] J. J. Silber, A. Biasutti, E. Abuin, E. Lissi, *Advances in Colloid and Interface Science* **1999**, *82*, 189.

[83] T. K. Jain, M. Varshney, A. Maitra, *The Journal of Physical Chemistry* **1989**, *93*, 7409.

[84] A. Goto, H. Yoshioka, H. Kishimoto, T. Fujita, *Langmuir* **1992**, *8*, 441.

[85] M. Valero, F. Sanchez, C. Gomez-Herrera, P. Lopez-Cornejo, *Chemical Physics* **2008**, *345*, 65.

[86] R. E. Riter, D. M. Willard, N. E. Levinger, *Journal of Physical Chemistry B* **1998**, *102*, 2705.

[87] B. Baruah, D. C. Crans, N. E. Levinger, *Langmuir* **2007**, *23*, 6510.

[88] M. Hasegawa, T. Sugimura, Y. Shindo, A. Kitahara, *Colloids and Surfaces a-Physicochemical and Engineering Aspects* **1996**, *109*, 305.

[89] Y. Hirose, H. Yui, T. Sawada, *Journal of Physical Chemistry B* **2004**, *108*, 9070.

[90] K. M. Manoj, R. Jayakumar, S. K. Rakshit, *Langmuir* **1996**, *12*, 4068.

[91] S. M. Andrade, S. M. B. Costa, *Photochemical & Photobiological Sciences* **2002**, *1*, 500.

[92] D. M. Zhu, Z. A. Schelly, *Langmuir* **1992**, *8*, 48.

[93] R. D. Falcone, N. M. Correa, M. A. Biasutti, J. J. Silber, *Langmuir* **2002**, *18*, 2039.

[94] M. Hasegawa, *Langmuir* **2001**, *17*, 1426.

[95] O. A. Elseoud, A. M. Chinelatto, M. R. Shimizu, *Journal of Colloid and Interface Science* **1982**, *88*, 420.

[96] S. Biswas, S. C. Bhattacharya, B. B. Bhowmik, S. P. Moulik, *Journal of Colloid and Interface Science* **2001**, *244*, 145.

[97] D. C. Crans, C. D. Rithner, B. Baruah, B. L. Gourley, N. E. Levinger, *Journal of the American Chemical Society* **2006**, *128*, 4437.

[98] J. J. Rack, T. M. McCleskey, E. R. Birnbaum, *Journal of Physical Chemistry B* **2002**, *106*, 632.

[99] H. Fujii, T. Kawai, H. Nishikawa, *Bulletin of the Chemical Society of Japan* **1979**, *52*, 2051.

[100] R. E. Smith, P. L. Luisi, *Helvetica Chimica Acta* **1980**, *63*, 2302.

[101] M. P. Pileni, *Journal of Physical Chemistry* **1993**, *97*, 6961.

[102] V. Uskokovic, M. Drofenik, *Surface Review and Letters* **2005**, *12*, 239.

[103] P. Ekwall, L. Mandell, K. Fontell, *Journal Of Colloid And Interface Science* **1969**, *29*, 639.

[104] P. Ekwall, L. Mandell, P. Solyom, *Journal of Colloid and Interface Science* **1971**, *35*, 266.

[105] S. Friberg, S. I. Ahmad, *The Journal of Physical Chemistry* **1971**, *75*, 2001.

[106] M. Valiente, E. Rodenas, *Journal Of Physical Chemistry* **1991**, *95*, 3368.

[107] X. L. Fang, C. F. Yang, Journal of Colloid and Interface Science **1999**, *212*, 242.

[108] J. O. Carnali, A. Ceglie, B. Lindman, K. Shinoda, *Langmuir* **1986**, *2*, 417.

[109] L. F. Gladden, *Chemical Engineering Science* **1994**, *49*, 3339.

[110] J. B. Miller, Progress in Nuclear Magnetic Resonance Spectroscopy **1998**, *33*, 273.

[111] A. Tzalmona, R. L. Armstrong, M. Menzinger, A. Cross, C. Lemaire, *Chemical Physics Letters* **1990**, *174*, 199.

[112] I. V. Koptyug, A. A. Lysova, V. N. Parmon, R. Z. Sagdeev, *Kinetics and Catalysis* **2003**, *44*, 401.

[113] M. M. Britton, A. J. Sederman, A. F. Taylor, S. K. Scott, L. F. Gladden, *Journal Of Physical Chemistry A* **2005**, *109*, 8306.

[114] M. M. Britton, Journal Of Physical Chemistry A **2003**, *107*, 5033.

[115] R. Evans, C. R. Timmel, P. J. Hore, M. M. Britton, *Chemical Physics Letters* **2004**, *397*, 67.

[116] M. C. Rogers, M. D. Mantle, A. J. Sederman, S. W. Morris, *Physical Review E* **2008**, *77*.

[117] V. V. Zhivonitko, I. V. Koptyug, R. Z. Sagdeev, *Journal Of Physical Chemistry A* **2007**, *111*, 4122.

[118] M. H. Levitt, *Spin dynamics*, John Wiley and Sons Ltd, Chichester, **2001**.

[119] R. Freeman, *Magnetic resonance in chemistry and medicine*, Oxford University Press, Oxford ; New York, **2003**.

[120] P. T. Callaghan, *Principles of nuclear magnetic resonance microscopy*, Clarendon Press; Oxford University Press, Oxford [England] New York, **1991**.

[121] P. J. Hore, *Nuclear magnetic resonance*, Oxford University Press, Oxford; New York, **1995**.

[122] E. M. Haacke, Magnetic resonance imaging : physical principles and sequence design, Wiley, New York, **1999**.

[123] D. Canet, *Nuclear magnetic resonance : concepts and methods*, Wiley, Chichester; New York, **1996**.

[124] E. L. Hahn, *Physical Review* **1950**, *80*, 580.

[125] H. Y. Carr, E. M. Purcell, *Physical Review* **1954**, *94*, 630.

[126] S. Meiboom, D. Gill, *Review Of Scientific Instruments* **1958**, *29*, 688.

[127] E. O. Stejskal, J. E. Tanner, *Journal Of Chemical Physics* **1965**, *42*, 288.

[128] J. D. Seymour, P. T. Callaghan, *Aiche Journal* **1997**, *43*, 2096.

[129] J. Hennig, A. Nauerth, H. Friedburg, *Magnetic Resonance in Medicine* **1986**, *3*, 823.

[130] R. B. Lauffer, *Chemical Reviews* **1987**, *87*, 901.

[131] H. Gries, in *Contrast Agents I, Vol. 221*, **2002**, p. 1.

[132] M. M. Britton, *Chemical Society Reviews* **2010**, *39*, 4036.

[133] M. Bottrill, L. K. Nicholas, N. J. Long, *Chemical Society Reviews* **2006**, *35*, 557.

[134] A. Haase, J. Frahm, *Journal of Magnetic Resonance* **1985**, *64*, 94.

[135] A. Haase, J. Frahm, W. Hanicke, D. Matthaei, *Physics in Medicine and Biology* **1985**, *30*, 341.

[136] R. Rodriguez, S. Vargas, D. A. Fernandez-Velasco, *Journal of Colloid and Interface Science* **1998**, *197*, 21.

[137] A. Salabat, J. Eastoe, K. J. Mutch, R. F. Tabor, *Journal Of Colloid And Interface Science* **2008**, *318*, 244.

[138] R. Finsy, *Advances In Colloid And Interface Science* **1994**, *52*, 79.

# 2 The bromate-sulfite reaction in a water-in-oil microemulsion

## 2.1 Introduction

There is great interest in the coupling of nonlinear autocatalytic reactions with microscopically heterogeneous media such as microemulsions. The structure of the microemulsion can be adjusted by altering the composition with which it is made, thus presenting the ability to "fine-tune" the medium in which the reaction is studied. Investigations of the non-linear, oscillatory Belousov-Zhabotinksy reaction in AOT based microemulsions has produced a variety of complex patterns and waves[1] that arise from the synergy between the reaction kinetics and the diffusion of the autocatalyst. The interest in reaction-diffusion fronts stems from their prevalence in nature; for example, they occur as calcium waves in cells[2] and as heat autocatalysed flame fronts[3].

Recently, McIlwaine *et al.*[4] were the first to investigate a nonlinear, pH clock reaction in water-in-oil (w/o) microemulsion (μE) systems. The effect of changing the water-to-surfactant ratio $\omega_0$, and the droplet fraction $\phi_d$, was investigated and the results for both stirred and unstirred experiments reported; the reaction behaviour was found to be dependent on the microstructure of the system. Reaction-diffusion fronts were observed for stationary experiments performed in capillaries with inner diameters of 1 and 2.6 mm, with the front behaviour being sensitive to the microemulsion structure. The fronts observed in the larger tubes demonstrated

convective instabilities[5], displaying features that have not been observed in the aqueous phase such as turbulent wake, an extinguishing finger and spiral motion[4].

The findings of the study were limited to the optical visualisation of the fronts; the effect of the reaction on the microemulsion structure was not probed and a charge-coupled device camera was used to acquire images of the sample. It was thus necessary to use a colour indicator and the acquired images were an integrated measure of the sample. The acquisition of a single image that displays the entire system hinders the ability to accurately and fully describe the propagating fronts; for example, it is difficult to differentiate and describe the front edge separately to the centre of the front. Subsequently, a full understanding of the behaviour is restricted. Magnetic resonance imaging (MRI) is able to non-invasively probe and image selected slices of the whole system, thus allowing a profile to be built that describes the behaviour of the system at the centre, separately to that at the edge. The acquired image represents only the area of the slice acquired and is not integrated over the full width of the sample.

Magnetic resonance imaging, however, presents challenges; contrast between different chemical or physical regions of interest needs to be established, although, unlike optical imaging where this contrast comes from colour, MRI requires that this contrast comes from differences in the magnetic resonance (MR) properties of nuclear spins (typically, and for the course of this work, those of $^{1}H$). Similarly to optical imaging, where colour indicators can be used, magnetic resonance contrast agents can be used to enhance the differences in MR properties. The differences in MR properties are also manipulated through the selection of appropriate imaging

experimental parameters. Although the technical details of MRI will not be discussed further in this chapter it is important to note that MR images can display artefacts that manifest as regions of different signal intensity/contrast, and unlike optical imaging where one can compare the acquired image with what can be seen visually, there is no way to simultaneously acquire an MR image and physically "see" the differences in MR properties, or even see the sample which is in the magnetic resonance spectrometer and being imaged.

This chapter investigates the behaviour of the bromate-sulfite reaction performed in a cetyltrimethylammonium (CTAB) microemulsion system for a given concentration of reactants and a defined microemulsion composition. The front behaviour in capillaries of inner diameter (i.d.) up to 8.6 mm is investigated which corresponds to an NMR tube of outer diameter (o.d.) 10 mm. NMR tubes of o.d. 10 mm were used to aid the development of suitable MRI techniques. Previous investigations[4] were performed in capillaries of i.d. = 1 and 2.6 mm.

## 2.2 Experimental

### 2.2.1 Sample preparation

Reactant mixtures of the aqueous bromate-sulfite reaction were obtained by mixing two separate reagent solutions (solution 1 and solution 2); solution 1 contained bromate species whilst buffer solution 2 contained sulfite, sulfuric acid and the pH-indicator bromocresol purple. Reactant mixtures of the bromate-sulfite reaction in a water-in-oil microemulsion system were prepared by mixing equal volumes of two separate reagent microemulsions (μE 1 + μE 2) where μE 1 had an aqueous phase of solution 1 and μE 2 had an aqueous phase of solution 2.

*2.2.1.1 Aqueous solutions*

All stock solutions were prepared using high-purity water (Nanopure filtered, 18.0 MΩ cm).

*i. Preparation of 1 M $H_2SO_4$*

A stock solution of sulfuric acid (1 M) was prepared by diluting 27.2 mL concentrated sulfuric acid (18.4 M, Fisher) in a 500 mL volumetric flask with water.

*ii. Preparation of solution 1*

Solution 1 was prepared by dissolving sodium bromate (1.51 g, Aldrich) in 100 mL water to give a solution with a $BrO_3^-$ concentration of 0.1 M.

*iii. Preparation of solution 2*

Solution 2 was prepared by dissolving sodium sulfite (1.26 g, Sigma-Aldrich) in water, adding $H_2SO_4$ (1.5 mL from 1 M stock) and diluting to 100 mL with water. To this, bromocresol purple (0.05 g, Sigma-Aldrich) was added to act as a colour, pH indicator with a transition pH range of 5.2-6.8; the indicator is purple at a pH of 6.8 and above and yellow at a pH of 5.2 and below. This gave solution 2 with initial $[SO_3^{2-}] = 0.1$ M and $[H_2SO_4] = 0.015$ M. According to the following equilibria:

$$H_2SO_4 \rightleftharpoons H^+ + HSO_4^-$$

$$HSO_4^- \rightleftharpoons H^+ + SO_4^{2-}$$

$$SO_3^{2-} + H^+ \rightleftharpoons HSO_3^-$$

the overall reaction equilibrium for solution 2 is:

$$2SO_3^{2-} + H_2SO_4 \rightleftharpoons 2HSO_3^- + SO_4^{2-}$$

Thus, at equilibrium, the concentrations of sulfite and bisulfite present in buffer solution 2 are 0.07 M and 0.03 M respectively.

*iv. Preparation of bromate-sulfite reactant mixtures*

Aqueous reactant mixtures of the bromate-sulfite reaction were obtained by mixing equal volumes of solutions 1 and 2 such that the concentration of reactants in the system at time = 0 is equal to half the concentration of stock reactants. Therefore, aqueous reactant systems contained $[BrO_3^-]_0$ = 0.05 M, $[SO_3^{2-}]_0$ = 0.035 M and $[HSO_3^-]_0$ = 0.015 M where subscript 0 represents initial conditions.

*2.2.1.2 Microemulsions*

Much of the interest in reverse micelles is due to the effects of confined water. Since $\omega_0$ is proportional to the size of the water droplet core[6], with an increase in $\omega_0$ resulting in water behaving more bulk-like[7-9], a water-to-surfactant ratio of 8.3 was used and represents hydrated reverse micelles whose water properties are less like those of bulk free water than for larger possible $\omega_0$ values (Figure 2.1). CTAB-hexanol-aq microemulsions were prepared with $\omega_0$ = 8.3 and $\phi_d$ = 0.4 (see Appendix 1[10]). This microemulsion composition was chosen as stable pH fronts of the bromate-sulfite reaction have been demonstrated for this composition[4, 10] (the behaviour of the bromate-sulfite pH clock reaction differs as a function of the microemulsion composition). The formation of the microemulsions is endothermic and so time was allowed for them to equilibrate to room temperature before use.

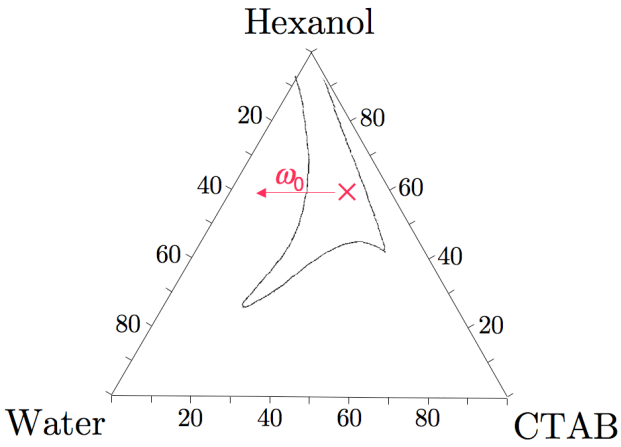


Figure 2.1: A phase diagram[11] for mixtures of CTAB, hexanol and water with the stable w/o μE region outlined. × represents $\omega_0 = 8.3$ and $\phi_d = 0.4$. The arrow indicates an increase in $\omega_0$ for the given droplet fraction.

*i. Preparation of μE 1*

Microemulsion 1 was prepared by dissolving CTAB (6.1 g, > 98%, Sigma) in 1-hexanol (14 mL, Acros). To this 2.5 mL of solution 1 (2.2.1.1ii) was added with stirring to give a colourless, macroscopically homogenous and optically transparent mixture.

*ii. Preparation of μE 2*

Microemulsion 2 was prepared by dissolving CTAB (6.1 g, > 98%, Sigma) in 1-hexanol (14 mL, Acros). To this 2.5 mL of solution 2 (2.2.1.1ii) was added with stirring to give a blue, macroscopically homogenous and optically transparent mixture.

*iii. Preparation of μE 3*

A third microemulsion (μE 3) was made by dissolving CTAB (6.1 g, > 98%, Sigma) in 1-hexanol (14 mL, Acros). To this 2.5 mL of 1 M $H_2SO_4$ was added with stirring to give a colourless, macroscopically homogenous and optically transparent mixture.

*iv. Preparation of reactant bromate-sulfite microemulsions*

Equal volumes of μE 1 and μE 2 were mixed to give reactant microemulsion mixtures with $\omega_0 = 8.3$ and $\phi_d = 0.4$. Since all reactant species of the bromate-sulfite reaction are polar they are expected to mostly reside within the reverse micelle droplet environment of the microemulsion. Consequently, reactant μEs had aqueous pseudophase concentrations of; $[BrO_3^-]_0 = 0.05$ M, $[SO_3^{2-}]_0 = 0.035$ M and $[HSO_3^-]_0 = 0.015$ M, where subscript 0 represents initial conditions. The sample preparation is represented schematically in Figure 2.2.

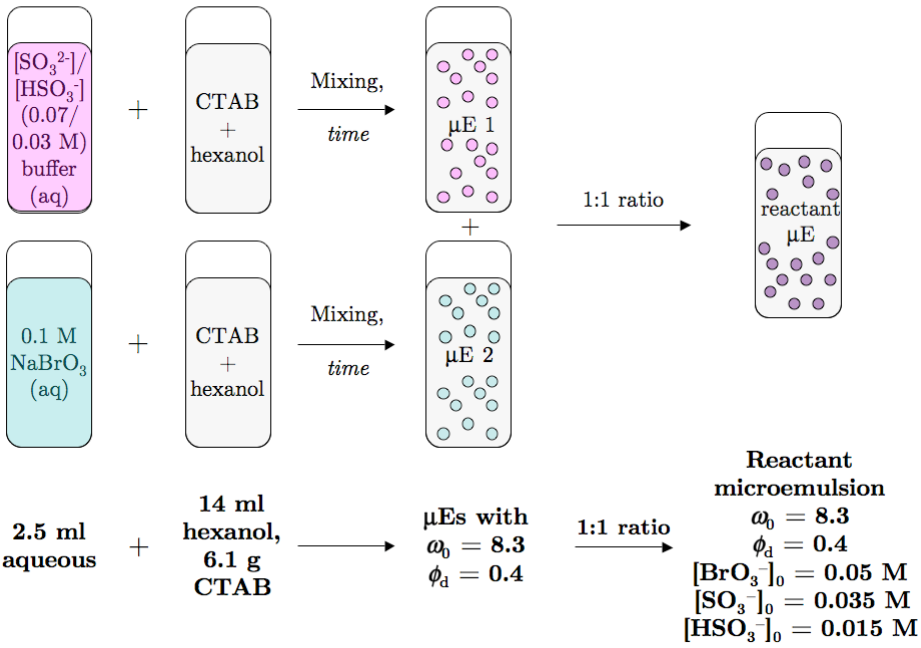


Figure 2.2: Schematic showing sample preparation for the bromate-sulfite reaction in a CTAB-hexanol-aq w/o microemulsion. Concentrations are those of the aqueous (pseudo)phase.

### 2.2.2 Techniques

*2.2.2.1 Stirred experiments*

Batch reactions were followed by recording the pH of the sample with time and observing a colour change. Solutions 1 and 2 were mixed in 250 mL beakers, and μEs

1 and 2 were mixed in 50 mL conical flasks, both were stirred at a constant rate of either 200, 600 or 1000 rpm using a magnetic stirrer bar and a stirrer-hotplate (Stuart CD162/1). The pH was recorded at 500 ms intervals using a computer running PicoLog technology[12] which was connected to a pH combination glass electrode (Radleys) via a data logger (DrDaq). The electrode and data logger were calibrated using pH 10, 7 and 4 standard buffers (Sigma-Aldrich) each day that they were used. The first measurement was taken immediately upon addition of the second solution/μE. All experiments were performed at a laboratory temperature of 21.6 ± 0.3 °C.

*2.2.2.2 Unstirred experiments*

Spatial behaviour of the w/o μE bromate-sulfite reaction was investigated in glass tubes of i.d. ≥ 2.3 mm. Aliquots of the reactant sample were transferred to cylindrical glass tubes suspended vertically to give a sample length of 50-55 mm. The reaction was initiated at the bottom of the closed tubes using μE 3 (0.02 mL) administered using a syringe and needle. Optical images were taken at least every 10 secs using a Canon EOS 1000D camera connected to a PC operating Canon EOS Utilities Capture Software. All experiments were performed at a laboratory temperature of 21.6 ± 0.3 °C. Images were analysed using Photoshop (Adobe). Distance calibration was achieved by capturing an image of the glass tube next to a ruler at the beginning and end of each experiment. A calibrated length and scale was then used in Photoshop and applied to all images for a given data set. The calibration was performed separately for each experiment.

## 2.3 Results

### 2.3.1 Stirred behaviour

The pH plots for both aqueous and microemulsion batch reactions are shown in Figure 2.3. The clock times were determined as the time at which the rate of change of pH is at a maximum (largest dy/dx). These were observed at 491 (18.7), 631 (9.0) and 658 (24.5) seconds for aqueous samples for stirring rates of 200, 600 and 1000 rpm respectively (bracketed values are standard deviations of 5 experimental repetitions). There was a large variation in the clock times of microemulsion samples with times ranging from 25 to 80 minutes. The initial and end pH of the microemulsion system was higher than the aqueous analogue.

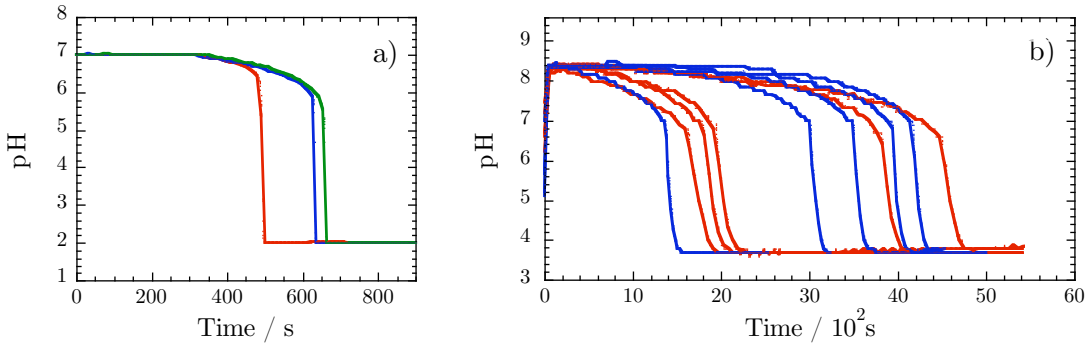


Figure 2.3: Clock reaction of the bromate-sulfite reaction in a) aqueous and b) microemulsion systems with initial aqueous concentrations of: $[BrO_3^-]$ = 0.05 M, $[SO_3^{2-}]$ = 0.035 M and $[HSO_3^-]$ = 0.015 M. Stirring rates of 200 (red line), 600 (blue line) and 1000 (green line) rpm were used.

### 2.3.2 Unstirred behaviour

Samples were initiated at the base of the capillaries; the bromocresol purple colour pH-indicator produced areas where the reaction had clocked within the sample to appear yellow, compared to blue regions where the reaction had not 'clocked'. Initiation was immediate and observed as a yellow/acidic region within the sample.

Acidic regions were next seen at the sample/air interface at the top of the tube. Fingers/plumes were seen to propagate from the product/reactant interface at both the top and bottom of the tube. Figure 2.4 shows optical images of propagating fronts of the bromate-sulfite-CTAB reaction for glass tubes of inner diameters 2.3 – 8.6 mm. For images shown in Figure 2.4a it can be seen that a front is formed which propagates at an approximate speed of 0.002 mm $s^{-1}$. A finger also forms that propagates upward with a speed greater than that of the front, the finger has an average speed of approximately 0.009 mm $s^{-1}$. Increasing the inner diameter of the cylindrical tubes resulted in the apparent absence of upward propagating fingering; all samples demonstrated downward propagating plumes. The plumes did not travel with a constant speed or constant waveform. Following observation of an upward and downward reaction front, reaction began to occur at the sample/glass interface. All front profiles were non-planar. Complete reaction, which was considered to be when the entire sample appeared yellow, exceeded the clock times of the stirred reactors.

## 2.4 Discussion

The experiments performed show good agreement with the findings of McIlwaine *et al.*[4] The induction period for the aqueous bromate-sulfite reaction with initial concentrations of bromate = 0.05 M, sulfite = 0.035 M and bisulfite = 0.015 M was between 8 and 11 minutes for the stirring rates investigated. A dependence of the clock time on the stirring rate was observed and has previously been reported[10, 13]. This dependence can be rationalised by consideration of the reaction mechanism; the reaction displays an initial induction period followed by a rapid autocatalytic change in pH. The autocatalysis thus occurs at a time whereby some critical $H^+$

concentration has been exceeded; larger domains of high acid concentration can accumulate at lower stirring rates. The microemulsion clock times were highly variable but tended to be approximately 5 times longer than the aqueous equivalent. The clock times of the microemulsion system were also sensitive to the batch volume, with a larger volume having a longer induction period. This variability has previously been observed[4, 14] and has been proposed as a possible demonstration of the sensitivity of the system to non-equilibrium concentration fluctuations[14].

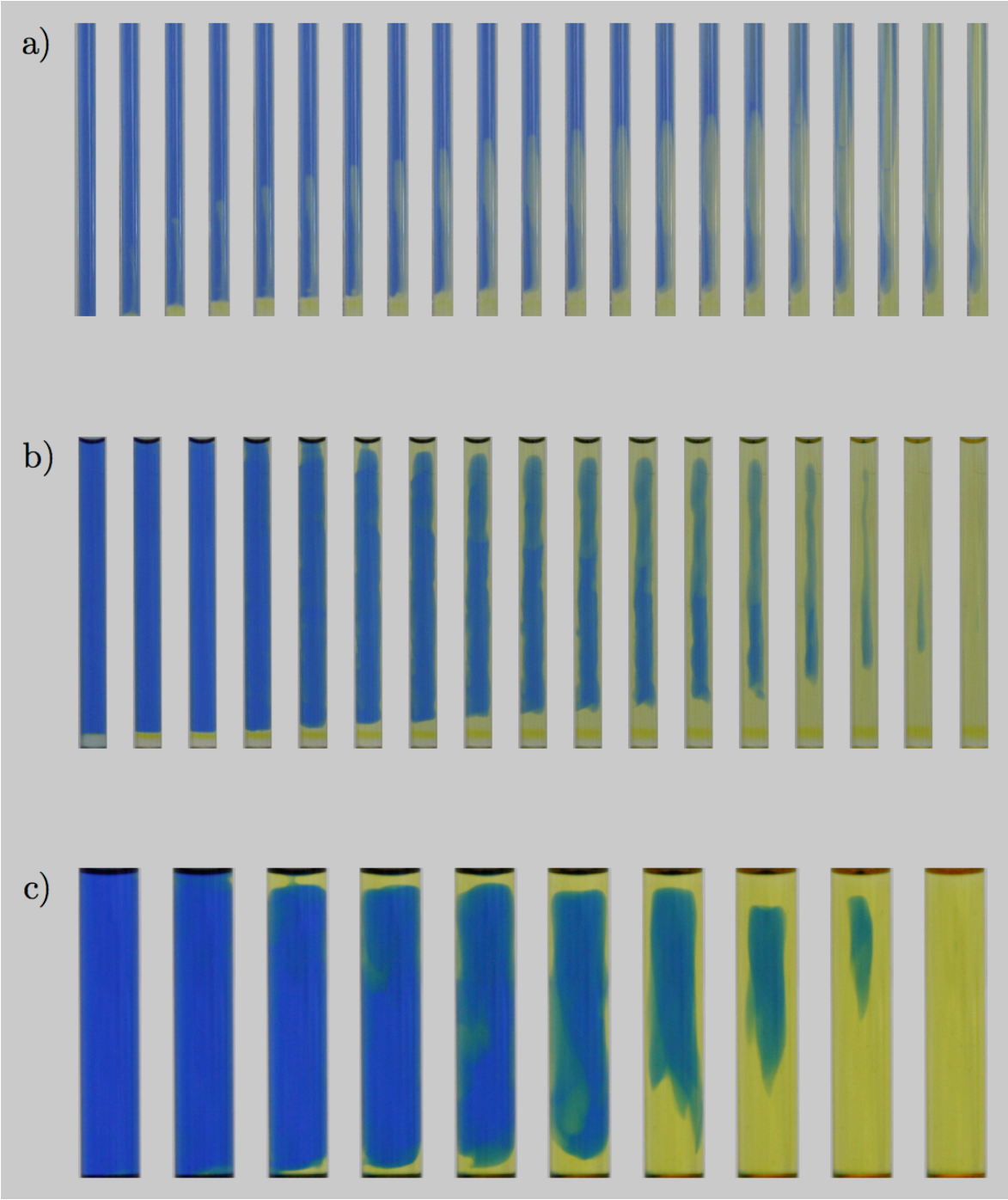


Figure 2.4: Optical images of the bromate-sulfite-CTAB reaction ($\omega_0$ = 8.3 and $\phi_d$ = 0.4) performed in glass tubes of i.d. a) 2.29 mm, b) 3.97 mm and c) 8.61 mm. Initial aqueous pseudophase concentrations were; [$BrO_3^-$] = 0.05 M, [$SO_3^{2-}$] = 0.035 M and [$HSO_3^-$] = 0.015 M. Images shown in a) show 50 × 3 mm and were acquired in 3 minute intervals, b) show 55 × 5 mm and were acquired in 10 minute intervals and c) show 50 × 10 mm and were acquired in 18 minute intervals.

The increase in the induction period and the measured pH has been rationalised through a description whereby the negatively charged reactant species reside at the positively charged interface of the droplet[4]. The decreased polarity at the interface favours ion association steps[15] such that the rate constant is reduced for the equilibrium:

$$HSO_3^- \rightleftharpoons SO_3^{2-} + H^+$$

which appears in the bromate-sulfite reaction mechanism[4]. It is important to note that there are uncertainties as to what the macroscopic measurement of pH in these systems represents. The structure of water confined in reverse micelles differs significantly to that of bulk water[16] and the disruption of the hydrogen-bonded network in reverse micelles has contributed to a decrease in the rate of proton-transfer processes[8] performed in such systems. Thus, water in these systems represent a new solvent for which pH calibration has not been performed[17].

A pure reaction-diffusion front in an aqueous-phase system typically travels with a constant waveform[18] and at a constant speed[19-21]. Deviation from this behaviour has previously been observed in the aqueous bromate-sulfite reaction[22] and the bromate-sulfite-CTAB system[4]. This deviation is due to convective effects in accord with the Pojman-Epstein model[5], which states that double-diffusive convection can occur for reactions where the change in enthalpy has the same sign as the change in the volume. The bromate-sulfite reaction is exothermic and has an isothermal decrease in volume[22]. Convective effects were observed in this study: unstirred reactors in tubes of i.d. 2.29 mm displayed upward fingering from the reaction front.

Upward fingering was not observed in tubes of a larger inner diameter. The effect of tube diameter on front behaviour has previously been studied in the aqueous bromate-sulfite reaction[22] and suppression of finger formation observed for larger tubes. This convective effect was considered to be a result of temperature distribution differences[22, 23] as the surface-area-to-volume ratio changed with tube diameter. The optical images taken for tubes of i.d. = 3.97 and 8.61 mm typically displayed downward propagating plumes, unstable fronts at the point of initiation and the inward propagation of reaction fronts from the tube walls. It is proposed that the reaction occurred quickly at the air/sample interface, and without initiation, due to the susceptibility of sulfur species to aerial oxidation, thus facilitating the breakdown of the sulfite/bisulfite buffer.

Complete reaction of the whole sample in the glass tubes did not occur before a time of 60 minutes and during this time both product and reactant regions coexisted within the sample. Propagating fronts, fingers and plumes were observed within the unstirred reactors. The complete description of the front behaviour and the direction of the front, particularly in larger tubes, remain difficult. The optical images present an integrated representation of the sample; although this allows for the description of upward and downward travelling fronts it is difficult to infer the direction of the front across the width of the tube. MR imaging can overcome this limitation. The investigation of front propagation in larger tubes thus allows for comparisons to be drawn between MR images acquired during the developmental process, and the observed/expected behaviour of the system.

## 2.5 Conclusion

The behaviour of the bromate-sulfite reaction of initial concentrations; $[BrO_3^-] = 0.05$ M, $[SO_3^{2-}] = 0.035$ M and $[HSO_3^-] = 0.015$, in a CTAB w/o microemulsion of $\omega_0 = 8.3$ and $\phi_d = 0.4$ has been investigated in capillaries of inner diameter up to 8.61 mm. The behaviour of the system shows good agreement with the findings of McIlwaine *et al.*[4] Larger capillaries did not support the upward fingering from the reaction front but did demonstrate downward propagating plumes, before reaction occurred at the sample/glass wall interface and proceeded to propagate inwardly. Having investigated the behaviour in 10 mm o.d. NMR tubes, MR imaging techniques can be developed and the images obtained compared directly to an expected behaviour. It is also anticipated that samples will display both product and reactant environments for a period of at least 60 minutes, thus development of MR contrast between the reactant and product environments can be investigated in that time.

## 2.6 References


[1] I. R. Epstein, V. K. Vanag, *Chaos* **2005**, *15*.

[2] L. F. Jaffe, *Proceedings of the National Academy of Sciences of the United States of America* **1991**, *88*, 9883.

[3] G. I. Sivashinsky, *Annual Review of Fluid Mechanics* **1983**, *15*, 179.

[4] R. E. McIlwaine, H. Fenton, S. K. Scott, A. F. Taylor, *Journal of Physical Chemistry C* **2008**, *112*, 2499.

[5] J. A. Pojman, I. R. Epstein, *Journal Of Physical Chemistry* **1990**, *94*, 4966.

[6] E. Rodenas, M. Valiente, *Colloids And Surfaces* **1992**, *62*, 289.

[7] R. E. Riter, D. M. Willard, N. E. Levinger, *Journal of Physical Chemistry B* **1998**, *102*, 2705.

[8] G. Angulo, J. A. Organero, M. A. Carranza, A. Douhal, *Journal of Physical Chemistry B* **2006**, *110*, 24231.

[9] A. M. Dokter, S. Woutersen, H. J. Bakker, *Journal Of Chemical Physics* **2007**, *126*.

[10] R. E. McIlwaine, *PhD Thesis* titled Nonlinear dynamics of acid- and base-regulated chemical systems, University of Leeds, School of Chemistry, **2007**.

[11] P. Ekwall, L. Mandell, K. Fontell, *Journal Of Colloid And Interface Science* **1969**, *29*, 639.

[12] PicoTechnology, http://www.picotech.com/data-logging-software.html.

[13] I. Nagypal, I. R. Epstein, *Journal Of Chemical Physics* **1988**, *89*, 6925.

[14] V. K. Vanag, D. P. Melikhov, *Journal of Physical Chemistry* **1995**, *99*, 17372.

[15] K. Bhattacharyya, *Accounts of Chemical Research* **2003**, *36*, 95.

[16] N. E. Levinger, L. A. Swafford, *Annual Review of Physical Chemistry* **2009**, *60*, 385.

[17] R. E. Smith, P. L. Luisi, *Helvetica Chimica Acta* **1980**, *63*, 2302.

[18] S. K. Scott, K. Showalter, *The Journal of Physical Chemistry* **1992**, *96*, 8702.

[19] R. Luther, *Zeitschrift Fur Elektrochemie Und Angewandte Physikalische* Chemie **1906**, *12*, 596.

[20] R. Luther, *Journal of Chemical Education* **1987**, *64*, 740.

[21] S. K. Scott, *Oscillations, waves, and chaos in chemical kinetics*, Oxford University Press, Oxford ; New York, **1994**.

[22] A. Keresztessy, I. P. Nagy, G. Bazsa, J. A. Pojman, *Journal Of Physical Chemistry* **1995**, *99*, 5379.

[23] I. P. Nagy, J. A. Pojman, *Journal Of Physical Chemistry* **1993**, *97*, 3443.

# 3 Magnetic resonance imaging of the aqueous bromate-sulfite reaction

## 3.1 Introduction

The bromate-sulfite reaction is an autocatalytic pH-clock reaction in which a weak acid (bisulfite) is converted to a strong acid (hydrogen sulfate). In stirred systems, the reaction mixture displays a sudden drop in the pH as acid autocatalysis occurs[1, 2], whilst in unstirred systems, the reaction displays propagating acidity fronts within the reaction mixture[3]. The propagating acidity fronts arise through the coupling of reaction with diffusion of the autocatalyst ($H^+$). Reaction-diffusion fronts are ubiquitous in nature and so the interest in such systems and their underlying mechanism spans many disciplines[4, 5]. Magnetic resonance imaging (MRI) is able to image selected slices of the reaction system. This is advantageous over previous studies[3] where a charge-coupled camera has been used; such optical imaging techniques produce images that are an integrated representation of the whole sample. The ability to image selected slices within the sample allows for a more thorough description of the front and it is intended that this will assist a better understanding of reaction-diffusion mechanisms.

MRI detects the signal from nuclei with a non-zero magnetic moment. Typically, that of the proton is used since the $^1H$ nuclei has a natural abundance of 99.9%, a high magnetic moment and is present in large concentrations in a number of physiological and chemical systems. The respective signal intensity from these protons in an imaging voxel results from a combination of their spin-density, spin-lattice ($T_1$) and

spin-spin ($T_2$) relaxation times and the parameters used in the imaging sequence. Commonly, inherent spin-density and relaxation time differences are insufficient in providing significant contrast between the regions of interest and, consequently, paramagnetic contrast agents are used. Both $T_1$ and $T_2$ are sensitive to the presence of paramagnetic species and so contrast agents (CA) are employed in MRI to enhance relaxation rates and contrast between different physiological and chemical environments[6-10]; a contrast agent may be chosen, for example, for its preference to reside in a given tissue type within the body and so reduce the relaxation times of protons within that region[8-10]. Since the products of the bromate-sulfite reaction are more acidic than the unreacted mixture, suitable pH-sensitive magnetic resonance (MR) active indicators were investigated to ensure contrast between the unreacted regions and the reaction fronts of the stationary system.

Typically, much of the research into contrast agents has been with a view to use them in medical applications and, subsequently, a main criterion has been the toxicity implications for patients. Complexes of $Gd^{III}$ are the most widely investigated and commonly used contrast agents since $Gd^{III}$ has seven unpaired electrons and has the greatest enhancement of magnetic resonance relaxivity ($1/T_1$ and $1/T_2$), whilst its ability to form chelates allows for the otherwise toxic $Gd^{3+}$ *aquo* ion to be safe for use *in vivo*[10, 11]. Similarly, much of the need for pH-sensitive contrast agents has focussed on the application towards pathological states that cause an imbalance between intra- and extra-cellular pH of tissues i.e. cancers and renal failure[12, 13]. For the purpose outlined here, physiological compatibility is not a requirement and the use of the most reported and somewhat more expensive gadolinium complexes is unnecessary.

The formation of transition metal complexes is known to be pH dependent[14, 15] and the access of solvent water protons to the metal ion is dependent upon the degree of complexation[6, 11, 14]. Thus, for paramagnetic metal ion chelates the relaxation rate of solvent water protons is lower than for solutions of the *aquo* metal. Evans and Hall[16, 17] have investigated a range of paramagnetic metal ions and chelating ligands for the measurement of pH in food systems by magnetic resonance techniques. A pH dependence on the $T_1$ and $T_2$ relaxation times of solutions containing the metal ions and ligands was observed, with several showing a significant change in $T_1$ for pH 2-8. In this chapter, the spin-lattice ($T_1$) and spin-spin ($T_2$) relaxation times for different pH solutions of 2 mM Cu(II)triethylenetetramine have been measured. Also, magnetic resonance techniques have been used to investigate the efficacy of Mn(II)- and Cu(II)-triethylenetetramine as suitable contrast agents in the aqueous bromate-sulfite reaction. It is hoped that the information obtained from this investigation will aid imaging of bromate-sulfite reaction fronts in the more complicated water-in-oil microemulsion system.

## 3.2 Experimental

### 3.2.1 Sample preparation

*3.2.1.1 Preparation of stock solutions*

All stock solutions were prepared using high-purity water (Nanopure filtered, 18.0 MΩ cm).

*i) Preparation of 1 M $H_2SO_4$*

Sulfuric acid (1 M) was prepared by diluting 27.2 mL concentrated sulfuric acid (18.4 M, Fisher) in a 500 mL volumetric flask with water.

*ii) Preparation of 1 M NaOH*

A 1 M solution of sodium hydroxide was prepared by dissolving 19.998 g NaOH pellets (≥ 98 %, Fluka) in a 500 mL volumetric flask.

*iii) Preparation of 0.125 M $MnCl_2$*

A 0.125 M manganese chloride solution was prepared by dissolving 2.475 g $MnCl_2.4H_2O$ (BDH) in a 100 mL volumetric flask.

*iv) Preparation of 0.125 M $CuSO_4$*

A 0.125 M copper sulfate solution was prepared by dissolving 1.994 g $CuSO_4$ (Sigma) in a 100 mL volumetric flask.

*v) Preparation of triethylenetetramine (trien) solution*

A solution of 0.0625 M minimum concentration trien was prepared by dissolving 1.219 g $NH_2CH_2CH_2(NHCH_2CH_2)_2NH_2.xH_2O$ (Aldrich) in 100 mL water. The trien was supplied as a hydrate with the molecular mass unknown; however, the specification sheet listed typically 19-24 % $H_2O$. An overestimation of the water content was used (25 %) to calculate a minimum concentration of the stock solution.

*3.2.1.2 Preparation of aqueous paramagnetic-metal chelate solutions*

*i) Preparation of acidic solutions*

An acidic (0.05 M $H_2SO_4$) solution of Cu(II)trien (2 mM) was prepared by diluting 5 mL $H_2SO_4$ (1 M stock), 3.2 mL trien (0.0625 M stock) and 1.6 mL $CuSO_4$ (0.125 M stock) with water up to 100 mL. An acidic (0.05 M $H_2SO_4$) solution of Mn(II)trien (0.5 mM) was prepared by diluting 5 mL $H_2SO_4$ (1 M stock), 0.8 mL trien (0.0625 M stock) and 0.4 mL $MnCl_2$ (0.125 M stock) with water up to 100 mL.

*ii) Preparation of basic solutions*

A basic (0.1 M NaOH) solution of Cu(II)trien (2 mM) was prepared by diluting 25 mL NaOH (1 M stock), 8 mL trien (0.0625 M stock) and 4 mL $CuSO_4$ (0.125 M stock) with water up to 250 mL. Attempts to make a basic (0.1 M NaOH) solution of Mn(II)trien (0.5 mM) by diluting 25 mL NaOH (1 M stock), 2 mL trien (0.0625 M stock) and 1 mL $MnCl_2$ (0.125 M stock) with water up to 250 mL were unsuccessful; a precipitate was formed on addition of $MnCl_2$ to the basic solution.

*iii)Preparation of solutions over a pH range*

Solutions of paramagnetic metal chelates of the multidentate ligand trien were made over a pH range of 1.1-10.0. The basic 2 mM Cu(II)trien solution was titrated against the acidic 2 mM Cu(II)trien solution and the pH measured using a combination glass electrode (purchased from Radleys) connected to a digital pH meter (Orion 720A). The electrode and pH meter were calibrated with pH 10, 7 and 4 standard buffers (Sigma-Aldrich) each day that they were used. Since the metal-chelate concentration was the same for both the titrate and titrand, the overall concentration of the metal-chelate remained the same throughout. At specific pH values (approximate integer values) an aliquot of the aqueous mixture was taken and used for $T_1$ and $T_2$ magnetic resonance relaxation time measurements. Basic solutions containing manganese resulted in the formation of a precipitate. Since this would affect the concentration of the paramagnetic metal ion in solution, the titration of basic Mn(II)trien solution against acidic Mn(II)trien solution would not produce solutions of a known metal ion concentration and was thus not performed. Aqueous samples of the manganese metal-chelate over a pH range were therefore not obtained.

*3.2.1.3 Preparation of paramagnetic bromate-sulfite reagent solutions*

Reagent mixtures of the aqueous bromate-sulfite reaction were made with either Cu(II)trien or Mn(II)trien present as a possible pH-sensitive MR-active indicator and are summarised in Table 2.

*i) Preparation of bromate reagent solutions*

Solution 1 was prepared by dissolving $NaBrO_3$ (1.51 g, Aldrich) in water, adding 3.2 mL trien (0.0625 M stock) and 1.6 mL $CuSO_4$ (0.125 M stock) and diluting to 100 mL. This gave solution 1 with a $BrO_3^-$ concentration of 0.1 M and a Cu(II)trien concentration of 2 mM. Solutions of Mn(II)trien were made in the same way using 0.4 mL $MnCl_2$ stock in place of the $CuSO_4$ and using 0.8 mL trien (0.0625 M stock); however this resulted in the formation of a precipitate. Bromate (0.1 M) solutions were also prepared in the absence of paramagnetic species and chelating ligands by dissolving $NaBrO_3$ (1.51 g) in 100 mL water (Solution 2).

*ii) Preparation of sulfite/bisulfite reagent solutions*

Solution 3 was prepared by dissolving sodium sulfite (1.26 g, Sigma-Aldrich) in water, adding 1 M stock sulfuric acid (1.5 mL), 3.2 mL trien (0.0625 M stock) and 1.6 mL $CuSO_4$ (0.125 M stock) and diluting to 100 mL. This gave solution 3 with a Cu(II)trien concentration of 2 mM. Solution 4 was prepared by dissolving sodium sulfite (1.26 g, Sigma-Aldrich) in water, adding 1 M stock sulfuric acid (1.5 mL), 1.6 mL trien (0.0625 M stock) and 800 mL $MnCl_2$ (0.125 M stock) with water up to 100 mL. This gave solution 4 with a Mn(II)trien concentration of 1 mM. Both buffer solutions 3 and 4 had equilibrium concentrations of sulfite and bisulfite equal to 0.07 M and 0.03 M respectively (see section 1.2.1.1iii).

Table 2: A summary of aqueous reagent solutions prepared.

| Solution | Bromate | Sulfite/Bisulfite buffer | Paramagnetic Metal and Ligand present |
|---|---|---|---|
| 1 | ✓ | × | 2 mM $Cu^{2+}$ and trien |
| 2 | ✓ | × | × |
| 3 | × | ✓ | 2 mM $Cu^{2+}$ and trien |
| 4 | × | ✓ | 1 mM $Mn^{2+}$ and trien |

*3.2.1.4 Preparation of paramagnetic bromate-sulfite reactant solutions*

Solutions 1 and 3 were mixed to give the aqueous bromate-sulfite system with initial $[Cu(trien)]^{2+}$ = 2 mM, $[BrO_3^-]$= 0.05 M, $[SO_3^{2-}]$= 0.035 M and $[HSO_3^-]$= 0.015 M. Equal volumes of solutions 2 and 4 were mixed to give the aqueous bromate-sulfite system with initial $[Mn(trien)]^{2+}$ = 0.5 mM, $[BrO_3^-]$= 0.05 M, $[SO_3^{2-}]$= 0.035 M and $[HSO_3^-]$= 0.015 M. The efficacy of 2 mM Cu(II)trien and 0.5 mM Mn(II)trien as suitable pH-sensitive MR indicators was investigated using relaxation time measurements and MRI following the immediate transfer of an aliquot of the reaction mixture to an NMR tube and placing in the bore of the magnetic resonance spectrometer. The pH change of the reaction mixtures was traced in batch and the time scale started at the point at which the two reagent solutions were mixed. For all measurements, the bromate and buffer solutions were freshly prepared and used immediately.

### 3.2.2 Techniques

*3.2.2.1 Magnetic resonance techniques*

All magnetic resonance (MR) measurements were performed on a Bruker DMX-300 spectrometer equipped with a 7 T vertical bore superconducting magnet and operating at a proton resonance frequency of 300 MHz. A 10 mm radiofrequency (rf)

saddle coil was used for relaxation measurements and a 25 mm rf birdcage coil for imaging experiments. The spectrometer was controlled using a Silicon Graphics workstation operating with XWIN-NMR software version 3.5 and ParaVision[18] version 2.1.1 software. All experiments were performed at a bore temperature of 289.7 ± 0.5 K which was measured using an *in situ* Eurotherm temperature probe.

*i) Relaxation time measurements*

The $T_1$ and $T_2$ relaxation times of 2 mM Cu(II)trien aqueous solutions were measured over a pH range of 1.2 – 10.0. $T_1$ relaxation times were measured using an inversion recovery sequence, $[180^\circ_x – \tau – 90^\circ_x – \text{acq}]_n$, performing $n = 16$ experiments with logarithmically-spaced variable delay times, $\tau$, ranging from 5 μs to 12 s. $T_2$ relaxation times were measured using a CPMG pulse program, $[90^\circ_x – (\tau – 180^\circ_y – \tau)_m – \text{acq}]_n$, performing $n = 19$ experiments, varying the number of echoes $m$ from 0 - 440 with a delay time, $\tau$, of 10 ms. Two signal averages were acquired for each experiment with a repetition time of 12 s. The 90° and 180° pulses were 12.5 μs and 25 μs, respectively at an attenuation of 6.0 dB. For all experiments a spectral width of 10 kHz was used and 16 k complex data points acquired. Both inversion recovery and CPMG pulse programs produced two-dimensional data sets with spectral data for each of the experiments within the sequence. A Fourier transform (FT) was performed on the 2D data sets and the peak amplitude used for analysis. Data processing and analysis was performed using both Prospa[19] and KaleidaGraph[20] software. $T_1$ and $T_2$ relaxation time constants were determined by fitting the acquired data to the exponential equations 1.28 and 1.25, respectively.

*ii) Rapid $T_2$ measurements*

$T_2$ was measured as a function of time for the aqueous paramagnetic bromate-sulfite reaction. To allow multiple $T_2$ measurements to be made during the course of the

reaction, a CPMG-train experiment was employed, $[90^{\circ}_{x}\text{–}(\tau\text{–}180^{\circ}_{y}\text{–}\tau\text{–acq})_{m}]$, rather than a CPMG pulse sequence. A CPMG-train does not acquire full spectral information for each echo; instead only 128 complex data points were acquired with a spectral width of 100 kHz. For reaction solutions of 2 mM Cu(II)trien, $m = 256$ echoes were performed with a delay time, $\tau$, of 10 ms and two signal accumulations were made with a repetition time of 12 s. For reaction solutions of 0.5 mM Mn(II)trien $m = 128$ echoes were performed with a delay time, $\tau$, of 0.5 ms and two signal accumulations were made with a repetition time of 2 s. The 90° and 180° pulses were 12 μs and 24 μs, respectively at an attenuation of 6.0 dB. The experiments were repeated continually for a period of 20 minutes. The 2D data sets were acquired for each experiment and did not have a FT operated on them. The data were processed and analysed using Prospa[19] to determine $T_2$ relaxation times.

*iii) Magnetic resonance imaging*

Magnetic resonance images of the aqueous bromate-sulfite reaction using Cu(II)trien as a contrast agent were obtained. A 10 mm o.d. NMR tube containing the sample was placed inside the probe of the magnetic resonance spectrometer and placed in the bore of the instrument. Images were obtained using the fast spin-echo imaging sequence RARE[21], $[90^{\circ}_{x}\text{–}(\tau\text{–}180^{\circ}_{y}\text{–}\tau\text{–acq})_{m}]_{n}$, where $m$ is the number of echoes acquired per excitation and $n$ is the number of excitations per imaging plane. Horizontal slices of 64 × 64 pixels for a 10 × 10 mm field of view were obtained using a RARE factor ($m$) of 16 ($n = 4$ per imaging plane), giving an effective echo time of 5.07 ms; a recovery time of 1000 ms was used between successive excitations. Vertical slices of 256 × 64 pixels for a 40 × 10 mm field of view were obtained again using a RARE factor of 16 and a recovery time of 600 ms. Slices were positioned at the centre of the sample and 0.5 mm in thickness. Two signal averages were acquired.

#### *3.2.2.2 Clock measurements*

The pH during the bromate-sulfite reaction, which contained paramagnetic metal chelate species, was followed as a function of time to determine the effect of paramagnetic species on the induction period of the reaction. The clock times were compared between reactions containing the paramagnetic species and reactions that did not contain the paramagnetic species. Reactant mixtures were prepared as described in section 1.2.1.4 by mixing aqueous reagent samples in 250 mL beakers. The aqueous reaction mixtures were stirred with constant stirring rates of 200, 600 and 1000 rpm using a magnetic stirrer bar and magnetic stirrer (Stuart CD162/1). The pH was recorded in 500 ms intervals using a pH combination glass electrode (Radleys) connected to a computer via a data logger (DrDaq), and using PicoLog technology[22]. The electrode and data logger had been calibrated with pH 10, 7 and 4 standard buffers (Sigma-Aldrich). The measurements were performed at room temperature (21.7 ± 0.5 °C).

#### *3.2.2.3 Optical imaging*

Optical images of the bromate-sulfite reaction containing 2 mM Cu(II)trien were obtained. An aliquot of reactant mixture solution was transferred to a 10 mm o.d. NMR tube to give a sample depth of 40 mm. The metal complex acted as a colour indicator, and was blue in the reactant environments (pH 7) and colourless in the product environments (pH 2). Images were taken every 5 seconds using a Canon EOS 1000D camera connected to a PC and controlled using Canon EOS utilities Capture Software.

## 3.3 Results and discussion

### 3.3.1 Relaxation times

The $T_1$ (spin-lattice) and $T_2$ (spin-spin) relaxation times of 2 mM Cu(II)triethylenetetramine solutions for a pH range are shown in Figure 3.1. The maximum error determined from two experimental repetitions was ± 26 ms.

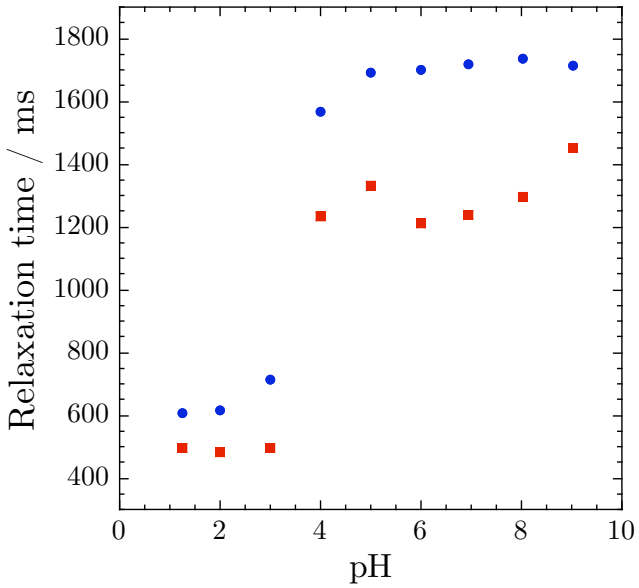


Figure 3.1: $T_1$ (blue circles) and $T_2$ (red squares) relaxation times of 2mM Cu(II)triethylenetetramine solutions for a pH range.

The Cu(II)trien is able to reduce the $T_1$ and $T_2$ of water (typically 2-3 seconds). For pH values ≥ 4 the relaxation times are approximately constant; however, as the pH decreases from 4 to 3 there is a significant increase in the rate of relaxation ($1/T_1$ and $1/T_2$). This change in the relaxation rate corresponds with a colour change from blue to colourless of the solutions at this pH. For pH values ≥ 4, the characteristically blue $[Cu(trien)]^{2+}$ complex (Figure 3.2) exists[23]; the complexation of the chelating ligand limits the amount of water able to enter the primary coordination sphere of the paramagnetic metal centre. However, for pH ≤ 3, the

$[Cu(trien)]^{2+}$ complex dissociates; water molecules are now in fast exchange between the bulk solvent and the primary coordination sphere of the paramagnetic metal ion. This close interaction with the paramagnetic metal ion further enhances relaxation rates.

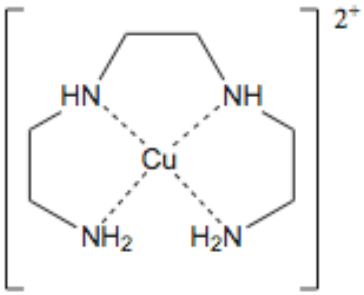


Figure 3.2: Bonding of copper(II) ion with the tetradentate ligand triethylenetetramine.

Since the aqueous bromate-sulfite reaction manifests as a pH clock, with a sharp change from pH 7 of the reactants to pH 2 of the products, the data in Figure 3.1 suggest that Cu(II)trien would be a suitable MR-active, pH indicator for investigation of this system. However, Cu(II) has only one unpaired electron and is thus a relatively weak paramagnetic contrast agent; solvent proton relaxation times remain longer than those in an environment containing more paramagnetic species of the same concentration[6]. Mn(II) complexes are commonly employed as contrast agents owing to the high magnetic moment[24] and five unpaired electrons of the metal ion. Mn(II) is thus able to significantly lower relaxation times and produce $T_2$ contrast. It would perhaps therefore, be of benefit to implement the pH dependent chelation of Mn(II) for investigation of the aqueous bromate-sulfite reaction, therefore enabling the use of a shorter $T_R$ and resulting in faster scans.

A plot of $T_1$ and $T_2$ relaxation data for Mn(II)trien could not be obtained owing to formation of a precipitate ($Mn(OH)_2$) in basic solutions. Hall and Evans impart that "the simplest way to map pH is via the relationship between metal ion solubility and pH"[16] since the more paramagnetic material in the aqueous solution the greater the enhancement of relaxation. This being true, it is important to remember that ultimately, contrast is required for the bromate-sulfite microemulsion system. The effect of the precipitate on both formation of the microemulsion and the microemulsion structure itself cannot be easily determined or understood. The reagents of the bromate-sulfite reaction, however, consist of a mixture of bromate solution and an *acidified* sulfite/bisulfite buffer solution. Addition of Mn(II)trien to the buffered solution did not result in the formation of $Mn(OH)_2$; a precipitate was formed on addition of Mn(II)trien to the bromate solution due to the basicity of the polyamine ligand. By adding double the required concentration of Mn(II)trien to buffered reagent solutions, the effect of the paramagnetic metal ion complex on transverse relaxation times was investigated during the progression of the bromate-sulfite clock reaction.

$T_2$ relaxation times of solvent protons were measured during the aqueous bromate-sulfite reaction with either Cu(II)- or Mn(II)-trien present as paramagnetic pH indicators; pH traces of the paramagnetic clock reaction were also recorded. Figure 3.3a and b show the $T_2$ constants as a function of time for the Cu(II) and Mn(II) systems respectively whilst figures c and d show typical pH traces against those of the non-paramagnetic bromate-sulfite reaction. Table 3 reports the average clock times of each aqueous bromate-sulfite reaction system calculated from the results of five experimental repeats.

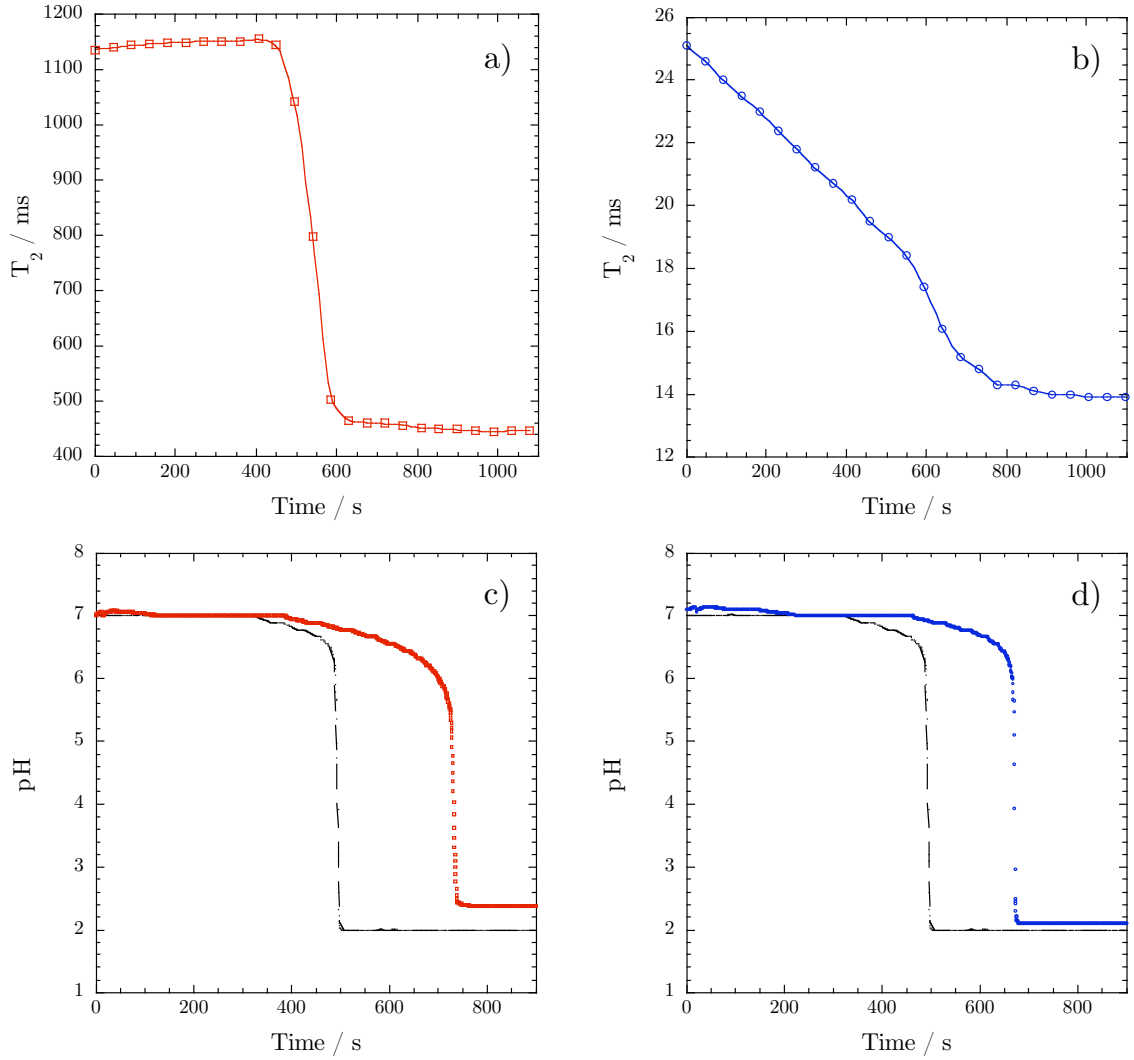


Figure 3.3: Figures a) and c) show the transverse relaxation times and pH trace respectively, for 2 mM $[Cu(trien)]^{2+}$ solutions of the bromate-sulfite reaction. Figures b) and d) show the transverse relaxation times and pH trace respectively, for 0.5 mM $[Mn(trien)]^{2+}$ solutions of the bromate-sulfite reaction. Initial concentrations were; $[BrO_3^-] = 0.05$ M, $[SO_3^{2-}] = 0.035$ M, $[HSO_3^-] = 0.015$ M. Time 0 in each case is the time at which the first data point was acquired. The black line represents the typical aqueous bromate-sulfite reaction without paramagnetic species or chelating ligands being present.

Figure 3.3a initially displays a constant $T_2$ relaxation time that rapidly drops at time $\approx$ 580 secs and then remains constant. The $T_2$ relaxation time changes from a maximum of 1150 ms to a minimum of 446 ms. Comparison of these $T_2$ values with

those determined in Figure 3.1 indicate a pH change of approximately 7 to ≤ 3. We can therefore deduce that the different stages in the $T_2$ trace reflect the induction period, the clocking of the reaction and the product environment of the reaction, respectively. This is supported by the pH trace of the reaction in figure c) where the induction period is shown to be approx 750 secs and a pH change of 7 to 2.4 occurs. The difference between the apparent induction periods may be due to how time = 0 was defined; for CPMG-train experiments, time zero was taken as the time at which the first experiment was performed and thus does not include the time taken to place the sample in the bore of the spectrometer, tune/shim etc. prior to performing the experiments. There may also be the additional effect of stirring rates; $T_2$ times were measured for stationary samples, compared to stirred batch samples for the pH traces. The induction period is dependent on stirring rates for reasons previously discussed.

Table 3: Clock times for aqueous samples of the bromate-sulfite reaction with and without paramagnetic metal-complexes (initial concentrations of $[BrO_3^-]$ = 0.05 M, $[SO_3^{2-}]$ = 0.035 M and $[HSO_3^-]$ = 0.015 M). Bracketed numbers show the standard deviation of data from 5 experimental repetitions.

| **Sample (aqueous)** | **Clock time / s** | | |
|---|---|---|---|
| | **200 rpm** | **600 rpm** | **1000 rpm** |
| Bromate-sulfite + 2 mM Cu(II)trien | 731 (16.4) | 743 (14.7) | 749 (41.8) |
| Bromate-sulfite + 0.5 mM Mn(II)trien | 669 (28.9) | 766 (60.5) | 735 (43.0) |
| Bromate-sulfite | 491 (18.7) | 631 (9.0) | 658 (24.5) |

Figure 3.3b shows the $T_2$ relaxation times as a function of time for the Mn(II)trien analogue; the relaxation times are much lower than those of the Cu(II) system, as anticipated. From time 0 secs, the $T_2$ continually decreases in an approximately linear fashion until t = 800 secs where the $T_2$ then remains constant at 14 ms. The

absence of an induction period followed by a rapid change in the relaxation times therefore does not represent clock behaviour; the pH trace in figure d and the clock times in Table 3 however, do display clock behaviour. The induction period is again longer than the standard bromate-sulfite reaction and a sudden change in pH from 7 to 2.1 at t ≈ 650 secs can be seen. The data therefore show that the change in $T_2$ is not pH dependent but due to a degradation of the metal complex with time. The manganese complex was investigated due to the greater efficacy of $Mn^{2+}$ as a paramagnetic CA; however, the results here demonstrate the instability of the Mn(II) complex when compared to the Cu(II) complex analogue. This is due to the larger size of the $Mn^{2+}$ ion and a lack of ligand field stabilisation energy in its complexes[25].

The results presented demonstrate the unsuitability of Mn(II)trien as a CA for MR imaging of the aqueous bromate-sulfite system. The percentage difference between relaxation times of the reactant and product environments in the Cu(II) system of ~ 60 % is a positive indicator that MR imaging would be possible, at least for the aqueous system. It is important to consider that an increase in observed induction times for this system reflects that the metal and/or ligand species affects the reaction kinetics. It is likely that the polyamine ligand acts with a buffering capacity, with the amine groups becoming protonated as $H^+$ ions are produced[26, 27]. The final pH increases with increasing concentration of trien due to the basicity of this ligand; the same trend is not observed in reagent conditions due to the presence of the sulfite/bisulfite buffer. Despite this effect on the reaction kinetics, the non-linear properties of interest remain and thus further investigation of the system was valid.

MR images of the aqueous bromate-sulfite reaction with Cu(II)trien (2 mM) employed as a CA were obtained. Figure 3.4a and Figure 3.4b show, respectively, horizontal and vertical MR images for two separate samples in 10 mm NMR tubes. The acidic product regions of the system are easily identifiable as red (high signal intensity) parts of the image whilst green reflects the unreacted species. The images in a) were acquired from t = 468 s and b) t = 474 s where t = 0 was the time at which the sample aliquot was taken from the mixed reagent solution. Optical images were also taken and are shown in Figure 3.5; here, Cu(II)trien acts as a colour indicator. This is advantageous as it allows for comparison to be made between MR images and those obtained optically and confirms that features observed in the MR images are true and are not the result of image artefacts. Both sets of images acquired i.e. optical and MR, display the same features; all images show multiple fronts and a greater rate of product formation at the base of the NMR tube. As anticipated from the relaxation data, MR contrast was easily achievable in the presence of Cu(II)trien.

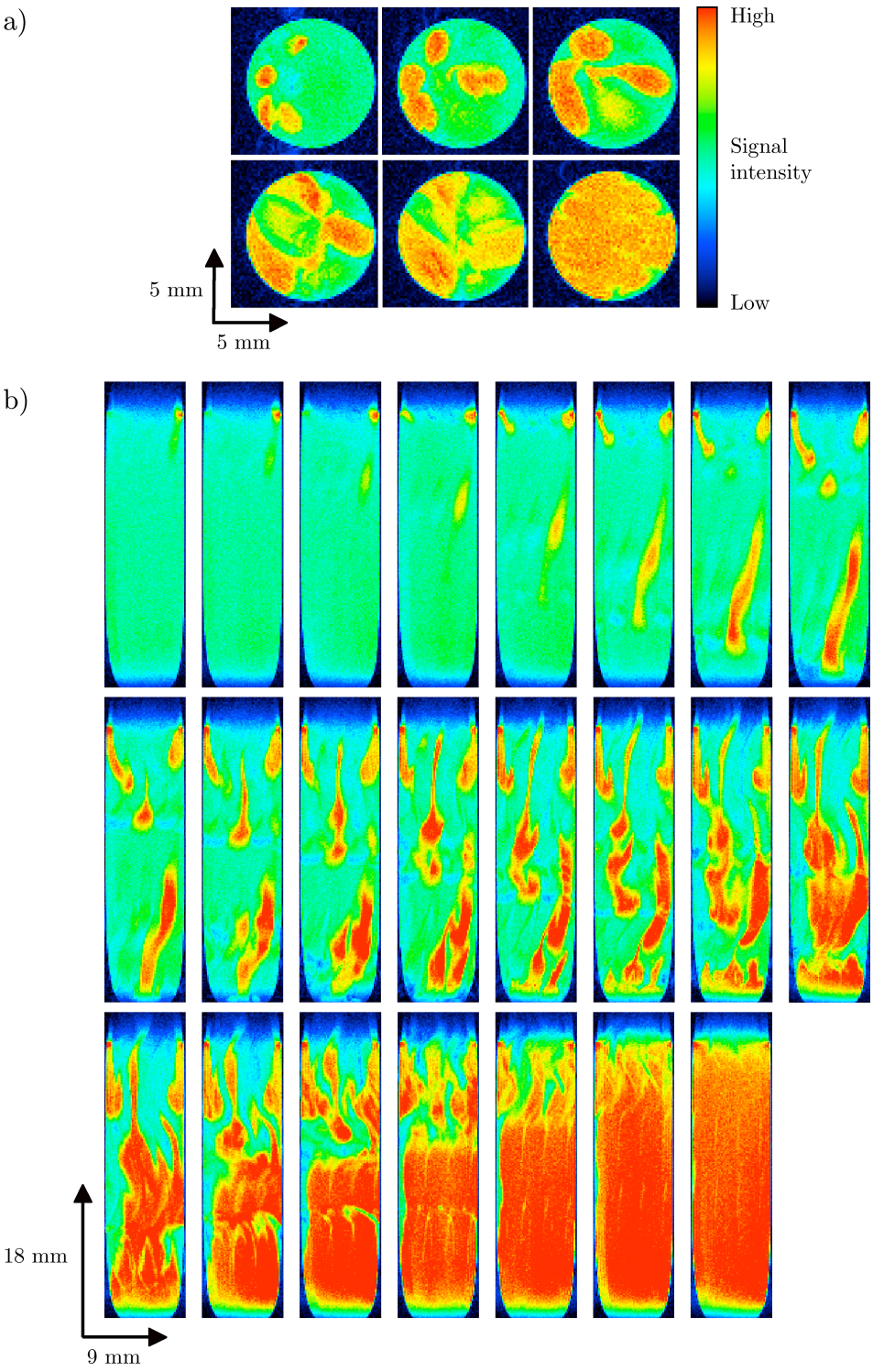


Figure 3.4: RARE images of the aqueous bromate-sulfite reaction ($[BrO_3^-]_0$ = 0.05 M, $[SO_3^{2-}]_0$ = 0.035 M and $[HSO_3^-]_0$ = 0.015 M) with 2 mM Cu(II)trien acting as a contrast agent. Images in a) of are of horizontal slices acquired every 8 secs. Images shown in b) are of vertical slices taken every 10 secs. Slice thickness is 0.5 mm at centre of sample for all images.

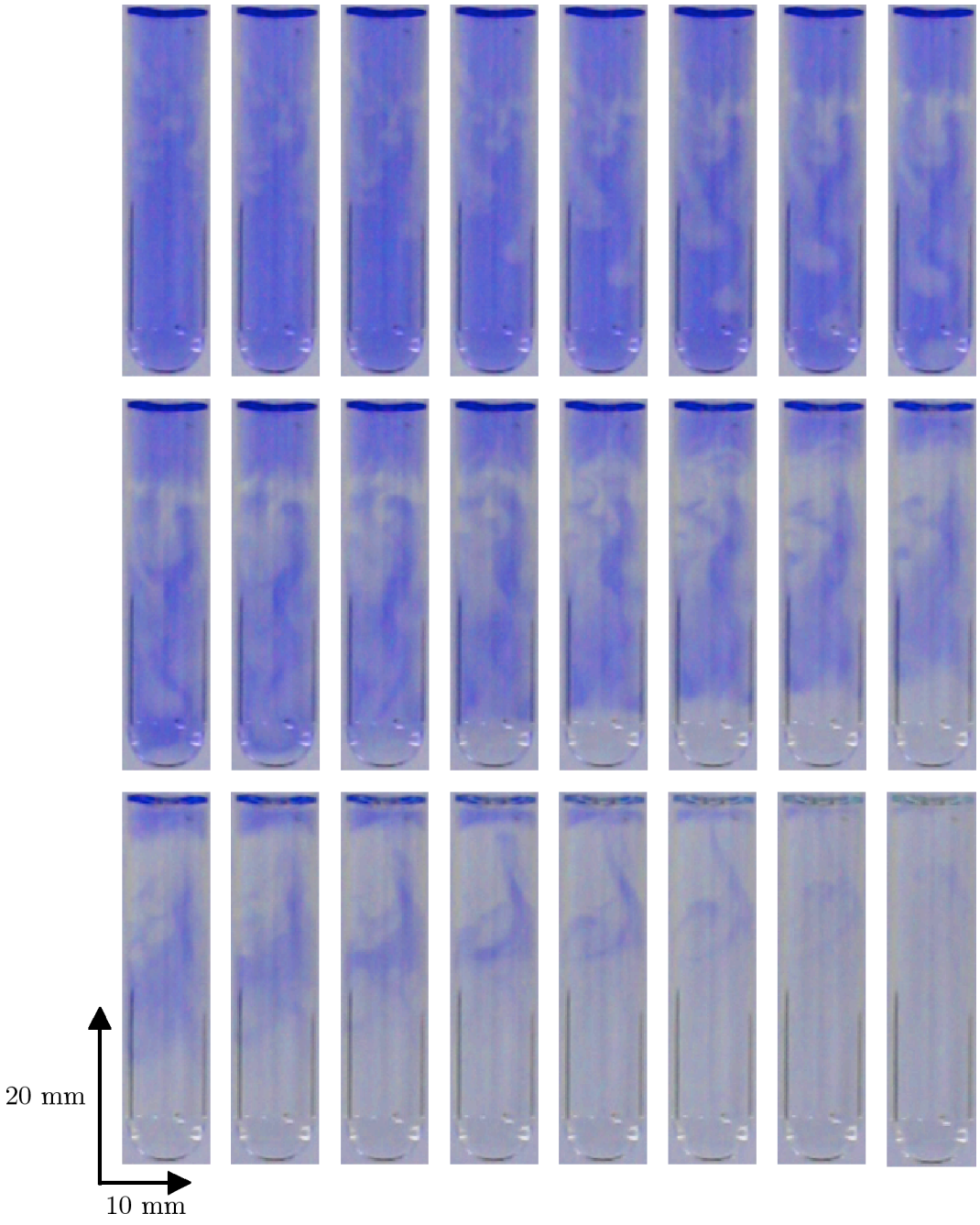


Figure 3.5: Optical images of the aqueous bromate-sulfite reaction ($[BrO_3^-]_0$ = 0.05 M, $[SO_3^{2-}]_0$ = 0.035 M and $[HSO_3^-]_0$ = 0.015 M) with 2 mM Cu(II)trien acting as a colour indicator. Images shown are taken every 5 seconds from t = 440 secs.

## 3.4 Conclusions and further work

NMR relaxation times of 2 mM Cu(II)trien solutions have been recorded as a function of pH. The relaxation times of solvent water protons changed significantly at a pH of 3-4; both $T_1$ and $T_2$ relaxation times were higher at pH values of 4 and above. This was explained by considering the pH dependent chelation of the metal complex and the relaxation mechanisms that occur. For pH values $\geq$ 4, the aqueous solutions were blue owing to the presence of the metal-complex; this chelation of the metal ion restricts solvent water entering the primary coordination sphere of the paramagnetic metal ion. For low pH values however, the metal exists as the hexa-hydrate ion where the primary coordination sphere comprises solvent water. The close proximity of the water to the paramagnetic ion enhances relaxation processes of the solvent protons and thus the relaxation time is reduced. This pH dependent chelation and the subsequent effect on relaxation times has then been successfully utilised to provide MR contrast in the aqueous bromate-sulfite reaction. MR images were acquired using a RARE imaging pulse sequence and using Cu(II)trien as an MR-active pH indicator.

The effect of Cu(II)trien on the bromate-sulfite reaction kinetics has also been investigated. The pH was found to be higher in the product state and the induction period was longer. Both of these observations have been rationalised by considering the buffering capacity of the basic polyamine ligand. Further investigations (Chapter 5) will see the effect of Cu(II)trien on the bromate-sulfite reaction when performed in a water-in-oil microemulsion.

Although the main remit for the work in this thesis is the investigation of acidity fronts in heterogeneous media, there is an ongoing interest and development in non-linear kinetics of aqueous systems under flow[28-30]. Recently, MR imaging has been used to visualise propagating wave behaviour of the Belousov-Zhabotinsky (BZ) reaction in a Couette cell, with the images being used to develop a suitable model to describe the behaviour[31]. Since the BZ reaction is an example of an oscillatory reaction that displays multiple waves, it would be intuitive to image the behaviour of a *single* reaction front in such flow environments. The bromate-sulfite reaction in a Couette cell was briefly investigated using optical techniques with bromocresol purple as a colour indicator (Appendix 2). MR imaging of this system is a logical development of the work and would require a suitable CA: Cu(II)trien (2 mM), although suitable for imaging of the stationary system, has a relatively long relaxation time and hence presents problems for imaging of samples under flow, which would require short repetition times to remove flow artefacts. The investigation into pH-dependent chelation of paramagnetic metal ions can thus be continued for the development of suitable CAs for imaging of this system. It is suggested that the focus would be on stable manganese chelates.

## 3.5 References


[1] T. G. Szanto, G. Rabai, *Journal of Physical Chemistry A* **2005**, *109*, 5398.

[2] E. C. Edblom, Y. Luo, M. Orban, K. Kustin, I. R. Epstein, *Journal of Physical Chemistry* **1989**, *93*, 2722.

[3] A. Keresztessy, I. P. Nagy, G. Bazsa, J. A. Pojman, *Journal Of Physical Chemistry* **1995**, *99*, 5379.

[4] S. Anita, V. Capasso, *Mathematical Methods in the Applied Sciences*, *33*, 1235.

[5] V. Volpert, S. Petrovskii, *Physics of Life Reviews* **2009**, *6*, 267.

[6] R. B. Lauffer, *Chemical Reviews* **1987**, *87*, 901.

[7] M. M. Britton, *Chemical Society Reviews* **2010**, *39*, 4036.

[8] Y. Okuhata, *Advanced Drug Delivery Reviews* **1999**, *37*, 121.

[9] A. E. Merbach, É. Tóth, *The chemistry of contrast agents in medical magnetic resonance imaging*, Wiley, Chichester; New York, **2001**.

[10] H. Gries, in *Contrast Agents I, Vol. 221*, **2002**, p. 1.

[11] E. Toth, L. Helm, A. E. Merbach, in *Contrast Agents I, Vol. 221*, **2002**, p. 61.

[12] R. J. Gillies, N. Raghunand, M. L. Garcia-Martin, R. A. Gatenby, *Ieee Engineering in Medicine and Biology Magazine* **2004**, *23*, 57.

[13] E. Perez-Mayoral, V. Negri, J. Soler-Padros, S. Cerdan, P. Ballesteros, *European Journal of Radiology* **2008**, *67*, 453.

[14] A. E. Martell, R. D. Hancock, *Metal complexes in aqueous solutions*, Plenum Press, New York, **1996**.

[15] J. Kragten, *Atlas of metal-ligand equilibria in aqueous solution*, E. Horwood; Halsted Press, Chichester, Eng. New York, **1978**.

[16] S. Evans, L. Hall, *AIChE Journal* **2005**, *51*, 1541.

[17] S. Evans, L. Hall, Canadian Journal of Chemical Engineering **2005**, *83*, 73.

[18] Bruker, *ParaVision* http://www.bruker-biospin.com/paravision-dir.html.

[19] Magritek, *Prospa*, http://www.magritek.com/prospa.html.

[20] Synergy software, *Kaleidagraph* http://www.synergy.com/.

[21] J. Hennig, A. Nauerth, H. Friedburg, *Magnetic Resonance in Medicine* **1986**, *3*, 823.

[22] Pico Technology, *PicoLog* http://www.picotech.com/data-logging-software.html.

[23] J. M. Baker, J. E. Teggins, J. W. Hoffman, *JAWRA Journal of the American Water Resources Association* **1971**, *7*, 1246.

[24] J. Lewis, R. G. Wilkins, *Modern coordination chemistry: principles and methods*, Interscience Publishers, New York, **1960**.

[25] F. A. Cotton, *Advanced inorganic chemistry*, 6th ed., Wiley, New York, **1999**.

[26] G. R. Hedwig, H. K. J. Powell, *Journal of the Chemical Society-Dalton Transactions* **1973**, *793*.

[27] W. A. E. McBryde, H. K. J. Powell, *Canadian Journal of Chemistry-Revue Canadienne De Chimie* **1979**, *57*, 1785.

[28] M. S. Paoletti, T. H. Solomon, *Physical Review E* **2005**, *72*.

[29] A. Pocheau, F. Harambat, *Physical Review E* **2008**, *77*.

[30] J. R. Boehmer, T. H. Solomon, *Epl* **2008**, *83*.

[31] B. W. Thompson, J. Novak, M. C. T. Wilson, M. M. Britton, A. F. Taylor, *Physical Review E* **2010**, *81*.

# 4 Investigation of pH in water-in-oil microemulsions using magnetic resonance techniques

## 4.1 Introduction

The reagents of the bromate-sulfite reaction can be included in a water-in-oil (w/o) microemulsion (μE) that subsequently displays propagating acidity fronts with interesting features[1]. Along with the desire to visualise these fronts 3-dimensionally, the incorporation of a pH-clock reaction in a w/o microemulsion introduces the need and want to probe and understand pH in the microemulsion system itself.

Water-in-oil microemulsions consist of hydrated reverse micelles (RMs) that are sequestered from the continuous oil phase by a layer of surfactant, and frequently, co-surfactant molecules. Within the RMs, a "bound"[2] layer of water exists which is associated with the polar moieties of the surfactant molecules, whilst the remaining water forms a pool in the centre of the droplet. The properties of water within this so called "water pool"[3] are known to differ from those of bulk water, with the effective polarity[4, 5] and microviscosity being affected[4, 6, 7]. As the size of the water pool increases, the water begins to behave more like bulk "free" water[2, 8]; the size of the water pool is determined by the water content[9] and the water-to-surfactant ratio[10], $\omega_0$, (equation 4.1) where an increase in $\omega_0$ correlates to an increase in the diameter of the droplet.

$$\omega_0 = [H_2O]/[\text{surfactant}] \quad (4.1)$$

Whether the macroscopic definition of pH is applicable to water in the restricted microenvironment of such systems is uncertain[11] and there continues to be debate about the nature of pH inside RMs. Even so, the ability to measure pH in RMs and to understand its effect is important in acid-base[12], biochemical and electron-transfer[13] reactions. Previously, the characterisation of pH in w/o microemulsions has relied on the use of spectroscopic measurements of pH-sensitive probe molecules[3, 14-17]. Several studies have used adsorption and fluorescence spectroscopy of organic dyes[18] or $^{51}V$ NMR of oxovanadate probes[19] to measure pH. However, when a probe molecule is used, an important variable in determining the pH inside the water droplets is the location of this molecule. Measurements using optical spectroscopy typically rely on the shifts of spectral peaks to explain molecular locations[20, 21]. The location of probe molecules have also been determined using NMR experiments that look at chemical shift changes or NOE interactions[19]. It has been found that there is a tendency for probe molecules to reside either in the surfactant layer or at the water droplet interface and that it is difficult to get a probe molecule to reside in the core of the micellar droplet. In addition to issues related to probe location, there are also questions about whether probe molecules change the structure of the RMs[20, 22]. For example, Rack *et al.*[20] discovered that the chromophore probe molecule $Ru(bpy)_3^{2+}$ was able to dramatically change the water content and distribution of droplet sizes in CTAB RMs. Consideration of these problems leads to the conclusion that an ideal method of study would be to measure the aqueous core directly. Experiments have been performed which achieve this by measuring the $^{31}P$ NMR chemical shifts of phosphate buffers contained in the RM[11, 15]. However, the

limitations with this approach include the need for a phosphate buffer to be used as the aqueous core, and for the assumption to be made that the p$K_a$ of phosphate ions remains the same in the water pools as they were in bulk water[11].

NMR techniques have been widely used to investigate and characterise microemulsion systems[23-25] and depend only on the signal of protons or, for example, $Na^+$ ions inherently present[26, 27]. NMR relaxation times have been measured as a function of increasing water content in anionic and non-ionic microemulsions[27-29] and have been used to provide information regarding the mobility of hydrophobic regions of surfactant molecules[30]. Similarly, diffusion measurements have been used to investigate phase changes for varying oil-water-(co-)surfactant compositions[31, 32]. The effect of pH on the NMR properties of microemulsion systems however, has not previously been investigated. The work in this chapter reports the investigation of water-in-oil microemulsions as a function of pH using magnetic resonance techniques. The investigation here is two-fold: firstly, the determination of pH in the microemulsion system is probed without introducing additional probe molecules. Secondly, the application to NMR investigations of the bromate-sulfite-CTAB system is approached.

## 4.2 Experimental

### 4.2.1 Sample preparation

#### *4.2.1.1 Preparation of stock solutions*

All stock solutions were prepared using high-purity water (Nanopure filtered, 18.0 MΩ cm).

*i) Preparation of 1 M $H_2SO_4$*

Sulfuric acid (1 M) was prepared by diluting 27.2 mL concentrated sulfuric acid (18.4 M, Fisher) in a 500 mL volumetric flask with water.

*ii) Preparation of 1 M NaOH*

A 1 M solution of sodium hydroxide was prepared by dissolving 19.998 g NaOH pellets (≥ 98 %, Fluka) in a 500 mL volumetric flask.

*iii) Preparation of 0.5 M LiCl*

A 0.5 M lithium chloride solution was prepared by dissolving 2.120 g LiCl (98 %, Fluka) in a 100 mL volumetric flask.

#### *4.2.1.2 Aqueous phase sample preparation*

Aqueous phase solutions were prepared for a range of pH values and differing ionic strengths prior to uptake in the microemulsion systems.

*i) Preparation of aqueous phase solutions over a pH range*

A 0.1 M sodium hydroxide solution was prepared by diluting 25 mL stock NaOH (1 M) in 250 mL with water. A 0.05 M $H_2SO_4$ solution was prepared by diluting 5 mL stock $H_2SO_4$ (1 M) in 100 mL with water. Aqueous solutions were prepared for a pH range of 1.1 – 9.4 by titrating the basic NaOH solution against 100 mL of the acidic $H_2SO_4$ solution. The pH was measured using a combination glass electrode (Radleys) connected to a digital pH meter (Orion 720A) that had been calibrated with pH 10, 7 and 4 standard buffers (Sigma-Aldrich). The ionic strength was calculated throughout the titration using the molar concentrations of all species present, assuming complete dissociation into ions. The total change in ionic strength was thus determined to be 0.025 M (Figure 4.1).

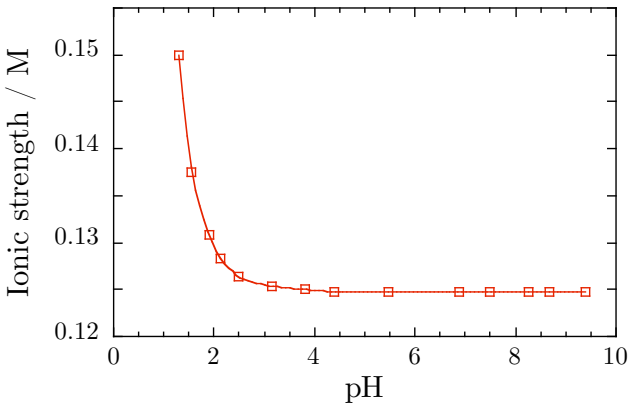


Figure 4.1: A plot to show the change in ionic strength versus pH for the titration of 0.1 M NaOH against 0.05 M $H_2SO_4$. The ionic strength was calculated using the molar concentrations of species and assuming complete dissociation into ions.

*ii) Preparation of aqueous phase samples with differing ionic strengths*

The sample preparation described above (4.2.1.2i) was repeated using different initial concentrations of acid and base. Thus, 0.2, 0.3 and 0.5 M solutions of NaOH and 0.10, 0.15 and 0.25 M solutions of $H_2SO_4$ were prepared by the appropriate dilution of 1 M stock solutions. The 0.2 M, 0.3 M and 0.5 M basic solutions were then titrated against 100 mL of 0.10, 0.15 and 0.25 M acidic solutions, respectively and, again, the pH measured. Maximum ionic strengths were thus double, triple and pentuple that determined in 4.2.1.2i accordingly. Lithium chloride solutions with a concentration of 0.3, 0.15 and 0.075 M were also prepared by the appropriate dilution of stock LiCl (0.5 M) to give neutral solutions with ionic strengths of 0.3, 0.15, and 0.075 M, respectively.

*iii)Preparation of aqueous bromate-sulfite reagents*

Details regarding the preparation of bromate-sulfite reagent solutions can be found elsewhere (Chapter 2, section 2.2.1). Briefly, two separate reagent solutions were prepared (solutions 1 and 2). Solution 1 was prepared by dissolving sodium bromate

(1.51 g, Sigma-Aldrich) in 100 mL water and solution 2 was prepared by dissolving sodium sulfite (1.26 g, Sigma-Aldrich) in 100 mL water with 1 M $H_2SO_4$ (1.5 mL).

#### *4.2.1.3 Preparation of microemulsions*

Four separate water-in-oil microemulsion systems were used;

(1) A ternary w/o μE consisting of 1-hexanol, aqueous phase and cationic surfactant cetyltrimethylammonium bromide (CTAB, Figure 4.2a).

(2) A quaternary w/o μE consisting of hexane, 1-pentanol, aqueous phase and cationic surfactant CTAB.

(3) A quaternary w/o μE consisting of cyclohexane, 1-hexanol, aqueous phase and nonionic surfactant Triton X-100 (TX, Figure 4.2b).

(4) A ternary w/o μE consisting of octane, aqueous phase and anion surfactant sodium bis(2-ethylhexyl) sulfosuccinate (AOT, Figure 4.2c).

CTAB-hexanol-aq[33], CTAB-hexane-pentanol-aq[34] and TX-cyclohexane-hexanol-aq[35, 36] mixtures are known to form water-in-oil microemulsions where the alcohol acts as a co-surfactant and stabilises formation of reverse micelles through its presence in the micellar interface[34, 37, 38]. AOT-octane-aq mixtures are known to form microemulsions in the absence of a co-surfactant[39].

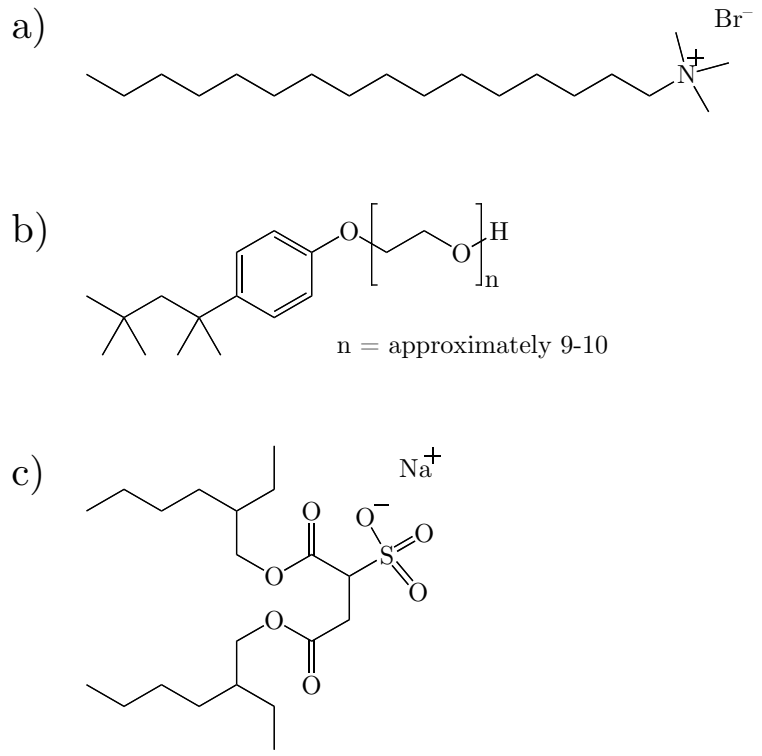


Figure 4.2: Structure of a) cationic surfactant CTAB b) nonionic surfactant TX and c) anionic surfactant AOT.

*i) Preparation of CTAB-hexanol-aq μEs*

Microemulsions were formed by adding aqueous phase (section 4.2.1.2) to mixtures of CTAB (> 98 %, Sigma) and 1-hexanol (Acros) to give w/o μE with $\omega_0$ = 5.3, 8.3 and 16.4, and a droplet fraction $\phi_d$ = 0.4. Table 4 provides a summary of the composition of each microemulsion and a phase diagram[33] illustrating these parameters within the w/o region is shown in Figure 4.3. Microemulsions were thus obtained for a range of aqueous phase pH values and ionic strengths. Reactant microemulsions of the bromate-sulfite reaction were also prepared with $\omega_0$ = 8.3 and $\phi_d$ = 0.4. Firstly, two separate microemulsions were prepared as described (microemulsions 1 and 2). Microemulsion 1 contained an aqueous phase of solution 1 and microemulsion 2 contained an aqueous phase of solution 2 (4.2.1.2iii). Equal

volumes of microemulsion 1 and 2 were then mixed to give the reactant bromate-sulfite-CTAB system. The formation of the microemulsion was endothermic and thus time was allowed for the preparations to warm to room temperature before use.

Table 4: Preparation of w/o microemulsions.

| $\omega_0$ | **Hexanol / mL** | **CTAB / g** | **Aqueous phase / mL** |
|---|---|---|---|
| 5.3 | 6.2 | 3.05 | 0.80 |
| 8.3 | 7.0 | 3.05 | 1.25 |
| 16.4 | 9.0 | 3.05 | 2.50 |

Mixtures of hexanol, CTAB and aqueous phase solutions with an ionic strength of approximately 0.7 M remained opaque and thus did not form microemulsions; ionic strength is known to have an effect on the size and structure of microemulsion[40, 41]. Kinematic viscosity measurements were obtained for microemulsions with $\omega_0 = 8.3$ using a reverse-flow glass viscometer (Cannon-Fenske). The viscosity did not change for the pH range investigated.

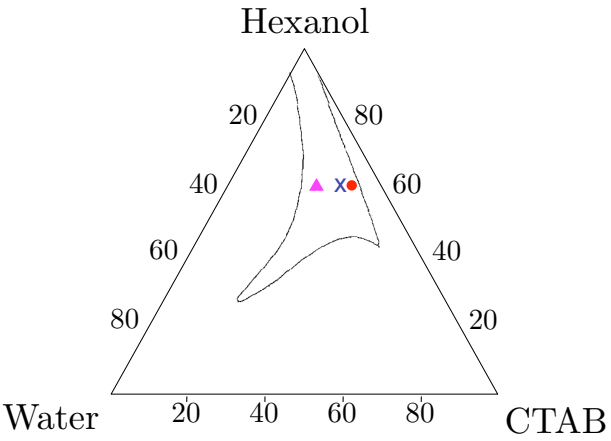


Figure 4.3: A phase diagram[33] for mixtures of CTAB, hexanol and water with the stable w/o μE region outlined and showing compositions that give $\phi_d = 0.4$ and $\omega_0 = 5.3$ (▲), 8.3 (x) and 16.4 (●).

*ii) Preparation of quaternary CTAB μEs*

Quaternary CTAB microemulsions were prepared for a pH range by dissolving 3.65 g CTAB (> 98 %, Sigma) in 13 mL 1-pentanol (Acros) and 10 mL hexane (Acros) and adding 1.5 mL of aqueous phase solutions (section 4.2.1.2.i). This gave w/o μEs with $\omega_0 = 8.3$ and a molar ratio of cosurfactant/surfactant, $P_0 = 0.3$ (Appendix 3).

*iii)Preparation of TX μEs*

Nonionic microemulsions were prepared for a pH range by adding aqueous phase samples (0.670 mL, section 4.2.1.2.i) to a mixture of TX (2.65 mL, Sigma), cyclohexane (5.00 mL, Fisher) and hexanol (2.7 mL, Acros). The mixture was left for a period of 24 hours to ensure an optically transparent, macroscopically homogenous phase was produced. This gave w/o μEs with $\omega_0 = 8.2$ and $\phi_d = 0.3$ (Appendix 4).

*iv) Preparation of AOT μEs*

Anionic microemulsions were prepared for a pH range. Firstly, a 1.5 M solution of AOT was prepared by dissolving 111.14 g AOT (Fluka) in 70 mL octane (Acros). Aqueous phase samples (2 mL, section 4.2.1.2.i) were added to the 1.5 M AOT solution (9 mL) and shaken vigorously. 6 mL of this solution was then diluted with 4 mL octane to give w/o μE with $\omega_0 = 8.2$ and $\phi_d = 0.4$[42] (Appendix 5).

*4.2.1.4 Preparation of hexanol and aqueous mixtures*

Mixtures of hexanol and water were also prepared by adding 1 mL of pH-adjusted aqueous stock solution (4.2.1.2i) to 5 mL hexanol and shaking for 10 minutes. The mixture was allowed to rest for 10 minutes and a sample taken from the hexanol layer.

### 4.2.2 Techniques

#### *4.2.2.1 Magnetic resonance experiments*

A Bruker DMX-300 spectrometer equipped with a 7 T vertical bore superconducting magnet operating at a proton resonance frequency of 300 MHz was used for all magnetic resonance (MR) experiments. The spectrometer was controlled using a Silicon Graphics workstation operating with XWIN-NMR version 3.5 and ParaVision version 2.1.1 software. Microemulsions were studied in 5 mm o.d. NMR tubes (Wilmad Economy NMR tubes) and were equilibrated to a bore temperature of 295 ± 0.1 K for 15 minutes prior to measurements. The temperature of the bore was measured and controlled using an *in situ* heater/air flow apparatus and using a Eurotherm temperature controller. The probe was tuned and matched and shimming was performed for all samples.

*i) Spectral measurements*

Spectra were collected for all non-reactive microemulsions using a pulse-acquire sequence, [90°-acq], using a 10 mm $^{1}$H birdcage transmit-detect radiofrequency (rf) coil. A spectral width of 20 kHz was used and 16k complex data points acquired. Two signal averages were acquired per experiment with a repetition time of 7 seconds. For bromate-sulfite reactant microemulsions, multiple spectra were recorded as a function of time using a 2D pulse acquire sequence, $[90°\text{-acq}]_m$, performing $m = 64$ experiments. Eight signal averages were acquired per experiment with a repetition time of 10 s. A spectral width of 10 kHz was used and 8k data points were acquired. The total pulse sequence time was 88 minutes and was repeated such that data were acquired for a 172 minute period. Two-dimensional data sets were obtained with spectral data for each experiment within the sequence. The data were processed and analysed using Prospa software.

*ii) Relaxation time measurements*

Relaxation time measurements were performed using a 10 mm $^1$H birdcage rf coil. $T_1$ relaxation times were measured using an inversion recovery sequence, [180°–$\tau$–90°–acq]$_n$, performing $n$ = 20 experiments with logarithmically-spaced variable delay times, $\tau$, ranging from 5 × $10^{-6}$ – 7 s. $T_2$ relaxation times were measured using a CPMG pulse program, [90°–($\tau$–180°–$\tau$)–acq$_m$]$_n$, performing $n$ = 28 experiments, varying the number of echoes $m$ from 0 - 2400 with a delay time, $\tau$, of 1 ms (the delay time affected the absolute $T_2$ values measured, Appendix 6). A delay time, $\tau$, of 2 ms was used for measurements of AOT microemulsions. Two signal averages were acquired per experiment with a repetition time of 7 s. The 90° and 180° pulses were 11.5 μs and 23 μs, respectively at an attenuation of 6.0 dB. For all experiments a spectral width of 10 kHz was used and 16 k complex data points acquired. Both inversion recovery and CPMG pulse programs produced two-dimensional data sets with spectral data for each of the experiments within the sequence. The 2D data sets were processed and analysed using both Prospa and KaleidaGraph software. $T_1$ and $T_2$ relaxation time constants were determined by fitting the data to equations 1.28 and 1.25 respectively.

*iii) Diffusion measurements*

Diffusion measurements were performed using a 10 mm $^1$H saddle transmit-detect radiofrequency coil. The rf coil was surrounded by linear magnetic field gradients in three orthogonal directions ($x$, $y$ and $z$) each with a maximum gradient strength of 140 G cm$^{-1}$. A pulsed field gradient spin echo (PGSE) sequence was employed using 16 different $z$-gradient strengths, $\boldsymbol{G}_z$, between – 120 and + 120 G cm$^{-1}$, a pulsed gradient duration, $\delta$, of 1-2 ms, and a time interval between two gradient pulses, $\Delta$,

of 150-250 ms. Eight signal averages were acquired for each experiment with a repetition time of 5 seconds. The echo attenuation was acquired as a function of gradient amplitude. The 2D data sets were processed and analysed using Prospa software and the diffusion coefficient $D$ determined by fitting the data to equation 1.33.

*4.2.2.2 Dynamic light scattering (DLS) experiments*

The hydrodynamic size of reverse micelles in CTAB and AOT microemulsions ($\omega_0$ = 8.3 and $\phi_d$ = 0.4) were measured as a function of pH using DLS. All DLS measurements were performed using a HPP5001 (Malvern instruments) particle sizer that operated using a He-Ne laser (3.0 mW, 633 nm) as a light source. Samples were used within two hours of preparation and were equilibrated to a temperature of 20 °C in the temperature-controlled chamber of the instrument, for 5 minutes prior to measurements being made. The viscosities and refractive indices of the continuous oil phase medium was used for each microemulsion, thus, for CTAB microemulsions a hexanol[43] viscosity and refractive index of 5.40 cP and 1.418 was used and for AOT microemulsions an octane viscosity and refractive index of 0.542 cP and 1.398 was used, respectively[44]. Each sample was measured three times and the data analysed by the instrument's software, which used the cumulants method of analysis to fit the intensity of scattered light to a correlation function. A report was produced by the software providing the details regarding the reliability of the fit. This report was used to test the validity of all results obtained. Measurements of CTAB microemulsions were repeated for μEs with $\phi_d < 0.4$, i.e. following dilution with the continuous oil phase hexanol.

## 4.3 Results

Figure 4.1 shows the numbering schemes for protons of hexanol and the surfactants CTAB and Triton X-100, and the $^1$H NMR spectra for CTAB-hexanol-aq and TX-cyclohexane-hexanol-aq microemulsions. Peak assignments for the CTAB microemulsion are given in Table 5 and those for the TX microemulsion are given in Table 6. The chemical shifts for peaks in the CTAB microemulsion spectra were calibrated using the chemical shift of the $H_l$ peak in CTAB from a spectrum of the same system using $D_2O$ as the aqueous phase and TMP as the reference. The chemical shifts for peaks in the Triton X-100 microemulsion spectra were calibrated using a literature value for the $H_8$ peak in Triton X-100 from a reference spectrum found in the literature for Triton X-100[45].

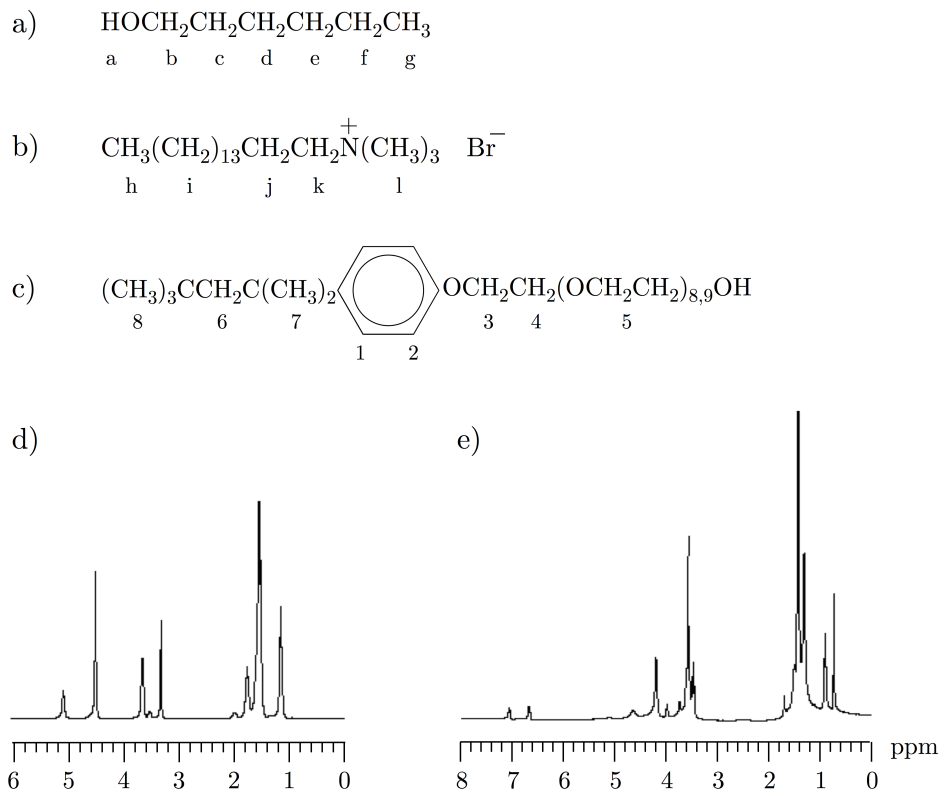


Figure 4.4: Molecular structure and numbering scheme for protons of a) 1-hexanol, b) CTAB and c) TX and $^1$H NMR spectra for neutral pH d) CTAB-hexanol-aq and e) TX-cyclohexane-hexanol-aq microemulsions.

Table 5: $^1$H NMR peak assignments for CTAB-hexanol-aq microemulsion with $\omega_0 = 8.3$ and $\phi_d = 0.4$.

| **δ / ppm** | **Assignment** |
|---|---|
| 5.12 | $H_a$ |
| 4.50 | $H_2O$ |
| 3.70 | $H_b$ |
| 3.54 | $H_k$ |
| 3.35 | $H_l$ |
| 1.98 | $H_j$ |
| 1.70 | $H_c$ |
| 1.56 – 1.42 | $H_i$, $H_d$, $H_e$, $H_f$ |
| 1.08 – 1.02 | $H_h$, $H_g$ |

Table 6: $^1$H NMR peak assignments for TX-cyclohexane-hexanol-aq microemulsion with $\omega_0 = 8.2$ and $\phi_d = 0.3$.

| **δ / ppm** | **Assignment** |
|---|---|
| 7.13 | $H_1$ |
| 6.76 | $H_2$ |
| 4.66 | $H_a$ |
| 4.23 | $H_2O$ |
| 4.00 | $H_3$ |
| 3.60 | $H_5$ |
| 3.47 | $H_b$ |
| 1.42 | Cyclohexane |
| 1.58 – 1.22 | $H_7$, $H_d$, $H_e$, $H_f$ |
| 0.84 | $H_g$ |
| 0.64 | $H_8$ |

Relaxation times of water (δ = 4.50 ppm) in the reverse micellar core of the CTAB microemulsion system were measured as a function of pH and are shown in Figure 4.5 (see Appendix 7 for relaxation times performed using 95% CTAB (Aldrich)). The $T_1$ relaxation times are unaffected by a change in pH, however, the $T_2$ relaxation times are found to be sensitive to pH at values lower than 6. For pH values greater

than 6, $T_2$ relaxation times are roughly constant; however, as the pH decreases from 6 to pH 3 the $T_2$ relaxation time decreases. A further decrease in the pH corresponds to a rapid increase in $T_2$. The proton relaxation times for hexanol and CTAB spectral peaks of the system are given in Table 7; there is no change in $T_1$ or $T_2$ relaxation times of these protons with pH.

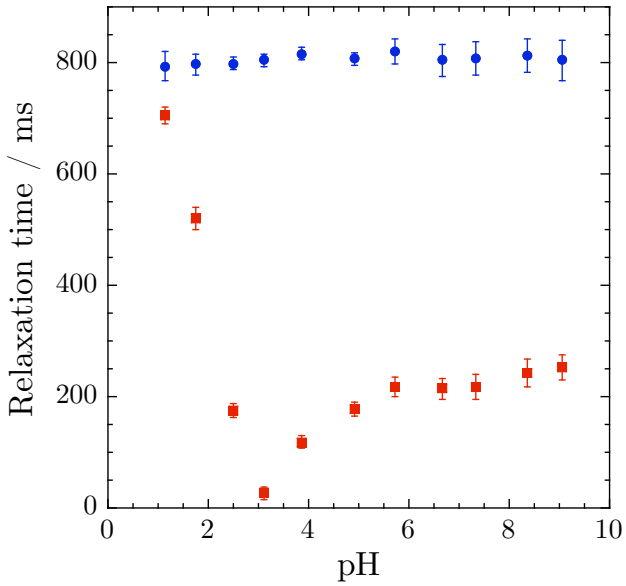


Figure 4.5: $T_1$ (●) and $T_2$ (■) relaxation times of water in CTAB-hexanol-aq microemulsions ($\omega_0$ = 8.3 and $\phi_d$ = 0.4) for a pH range of 1.2 – 9.3. The pH here is the measured pH of the aqueous stock solution prior to uptake in the microemulsion. Error bars represent the standard deviation from four experimental repeats.

Table 7: Proton relaxation times of selected peaks in the CTAB-hexanol-aq μE spectrum ($\omega_0$ = 8.2 and $\phi_d$ = 0.4). Bracketed values are the standard deviation of the mean calculated for two separate data sets corresponding to 24 data points.

| | **Chemical shift / ppm** | | | | |
|---|---|---|---|---|---|
| | **3.70** | **3.35** | **1.70** | **1.48** | **1.05** |
| $T_1$ / ms | 797 (22) | 410 (13) | 834 (14) | 927 (27) | 1370 (25) |
| $T_2$ / ms | *274 (51)<br>*27.3 (3.8) | 291 (14) | 744 (29)<br>13.3 (1.4) | 613 (14)<br>53.1 (6.9) | 880 (36) |

* pH range 1.2 – 8.0. Analysis of data for pH values > 8.0 did not produce acceptable $T_2$ fits.

The underlying origins for the pH-dependency of water $T_2$ relaxation times were investigated by probing the effects of ionic strength, proton exchange and $\omega_0$. As the pH of the aqueous stock phase was varied there was an associated change in ionic strength, with a minimum value of ≈ 0.125 M at pH 4 and above, and a maximum value of 0.15 M at pH 1. To test the effect of ionic strength, microemulsions were prepared with aqueous phase solutions of LiCl, whose concentrations gave neutral solutions with ionic strengths over and exceeding the range achieved during the variation in pH. The relaxation times of water in the microemulsion were found to remain constant for the ionic strengths investigated.

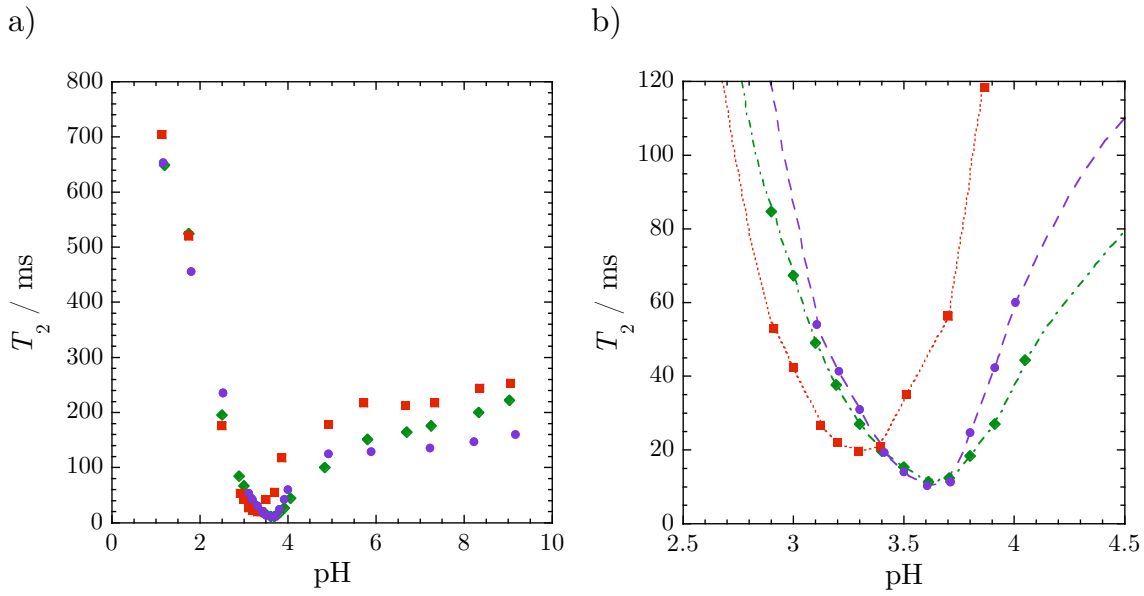


Figure 4.6: $T_2$ relaxation times of water in CTAB-hexanol-aq microemulsions ($\omega_0$ = 8.3 and $\phi_d$ = 0.4) for aqueous ionic strengths of 0.15 M (■), 0.30 M (◆) and 0.45 M (●) and for a) a pH range of 1.2 to 9.4 and b) a larger-scale graph showing the pH range 2.5 – 4.5 only. The pH is the measured pH of the aqueous stock phase prior to uptake in the microemulsion.

The sensitivity of the pH dependent behaviour to ionic strength was further tested by performing a series of relaxation time measurements for samples whose aqueous phase solutions had been prepared using an increased concentration of acid and

base, thus increasing the ionic strength of the aqueous solutions over a pH range. The $T_2$ relaxation times are shown in Figure 4.6 for three separate ionic strength solutions ranging from the maximum value at pH 1 of 0.15 M to 0.45 M. The same trend in relaxation behaviour is observed for all three experiments although there is a shift in the minimum to higher pH as the ionic strength is increased. $T_1$ relaxation times were the same for all samples (Appendix 8).

Ionic strength is known to affect the formation and size of reverse micelles[40, 41]. Attempts were thus made to determine the effect on the size of the reverse micelles as a function of pH using diffusion measurements and DLS; both techniques use the Stokes-Einstein equation to relate the hydrodynamic radius, $R_h$, to the diffusion coefficient, $D$:

$$D = \frac{k_B T}{6\pi\eta R_h} \tag{4.3}$$

where $k_B$ is the Boltzmann constant, $T$ is the temperature and $\eta$ is the dynamic viscosity of the medium in which the droplets exist. Diffusion measurements for water of the CTAB-hexanol-aq μE system are shown in Figure 4.7 and can be seen to be constant, within the margins of error, for the pH range investigated. Reliable droplet sizing could not be performed using DLS; the polydispersity index was high ($> 0.4$) for the majority of samples and the quality report produced by the software stated that the "result does not meet criteria" for all samples.

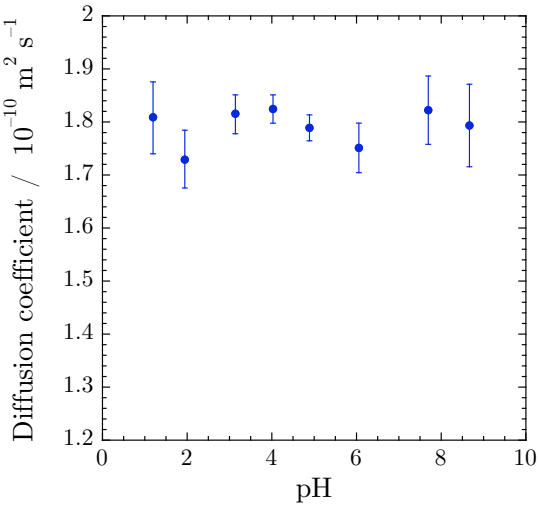


Figure 4.7: Diffusion coefficients of water in reverse micelles of CTAB-hexanol-aq microemulsions ($\omega_0 = 8.3$ and $\phi_d = 0.4$) for a pH range.

The occurrence of proton exchange between hydroxyl protons in alcohol and water is a well-known phenomenon and is found to be catalysed by acid or base[46-53]. Proton exchange has also been observed between hydroxyl protons of butanol and water molecules in a quaternary N-octylribonamide-brine-decane-butanol microemulsion[25]; the rate of proton exchange was found to be dependent upon the composition of the microemulsion. Accordingly, the exchange phenomenon was investigated between the hydroxyl groups of hexanol and water in the CTAB-hexanol-aq microemulsion as a function of pH; a series of $^1$H NMR spectra, over a range of pHs, are shown in Figure 4.8. At pH 3.8 two peaks are observed, one for water ($\delta_{H_2O}$) and one for the hydroxyl group of hexanol ($\delta_{H_a}$). As the pH is decreased these two peaks become broader and move together until, at an approximate pH of 3.4, these peaks coalesce. The pH at which coalescence occurs corresponds to the pH at which the minimum $T_2$ relaxation time is recorded. As the pH drops further, the linewidth of the coalesced peak continues to decrease.

The same effect is observed in $^1$H NMR spectra for mixtures of hexanol and water over a similar pH range and is shown in Figure 4.9. Again, at higher pH (pH 4) two peaks are observed, one for water ($\delta_{H_2O}$ = 4.60 ppm) and one for the hydroxyl group of hexanol ($\delta_{H_a}$ = 5.38 ppm). These peaks merge at approximately pH 3.7, following which the peak linewidth continues to decrease as the concentration of acid increases.

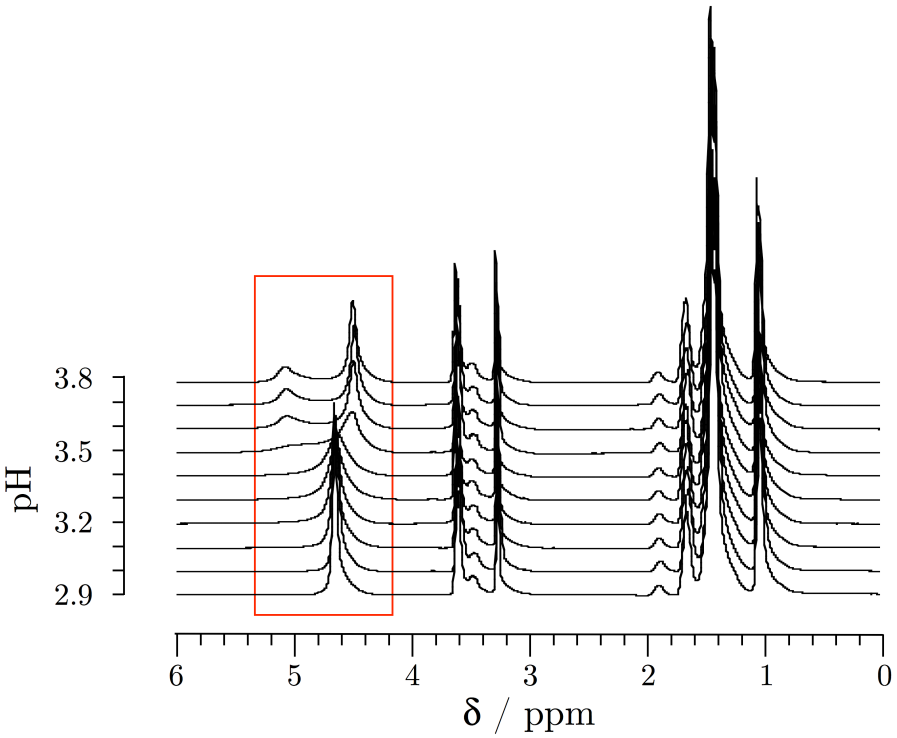


Figure 4.8: $^1$H NMR spectra of CTAB-hexanol-aq microemulsions ($\omega_0$ = 8.3 and $\phi_d$ = 0.4) over an aqueous pseudophase pH range of 2.9 -3.8. The hydroxyl peaks are outlined in red.

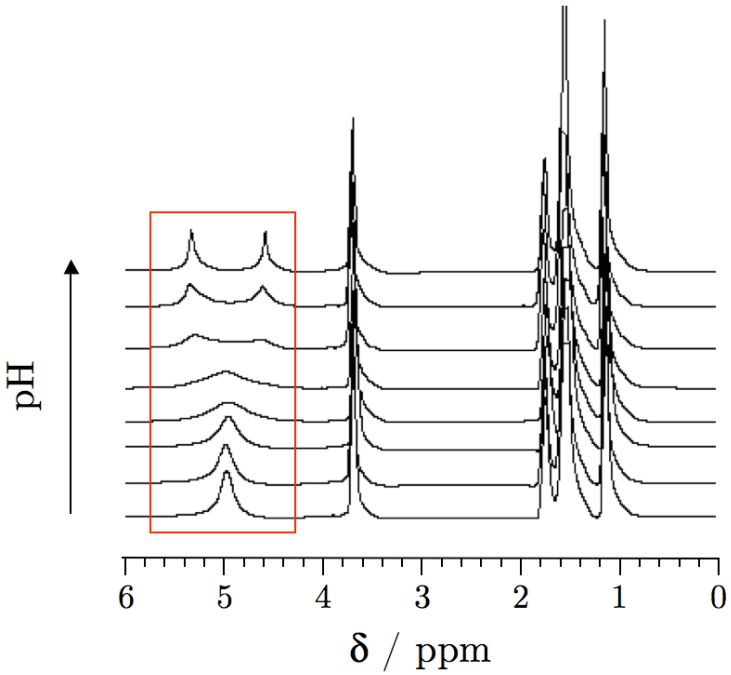


Figure 4.9: $^{1}$H NMR spectra for mixtures of hexanol and water solutions over an aqueous pH range of 3.3 to 4.0. The hydroxyl peaks are outlined in red.

Finally, the effect of $\omega_0$ was investigated on the pH-dependent relaxation behaviour of water in CTAB-hexanol-aq droplets. Figure 4.10 shows the relaxation times for water as a function of pH for three $\omega_0$ values. Whilst the same trend is observed for $T_2$ relaxation times, the pH at which the minimum appears shifts with $\omega_0$, and can be seen to increase with increasing $\omega_0$. As $\omega_0$ increases the hydroxyl peaks were also seen to shift further downfield; the change in chemical shift of the water peak following coalescence was smaller for larger $\omega_0$ whilst the chemical shift difference between the hexanol-hydroxyl and coalesced resonances increased with $\omega_0$ (Appendix 9). For each $\omega_0$, the $T_1$ values remain constant but the $T_1$ decreases with a decreasing $\omega_0$.

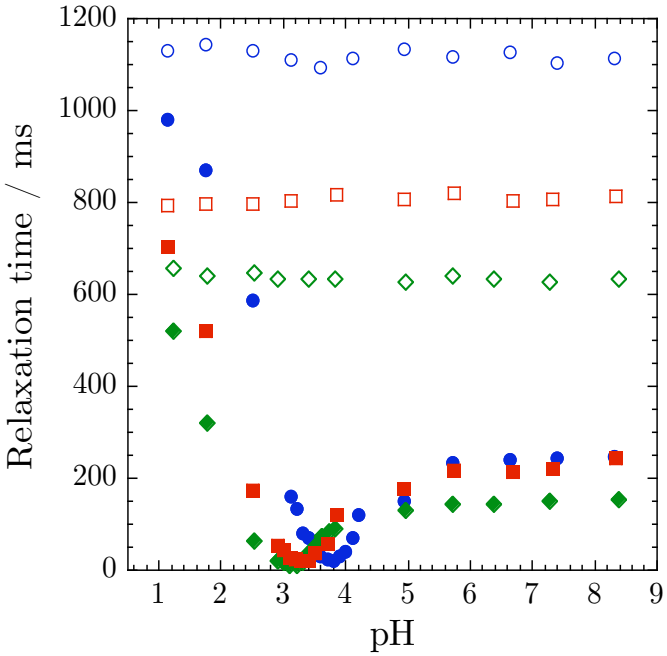


Figure 4.10: $T_1$ (hollow shapes) and $T_2$ (filled shapes) relaxation times of water in CTAB-hexanol-aq microemulsions of $\phi_d = 0.4$ and $\omega_0 = 16.4$ (blue circles), $\omega_0 = 8.3$ (red squares) and $\omega_0 = 5.3$ (green diamonds). The measured pH is that of the aqueous stock solution prior to uptake into the reverse micelles of the microemulsion.

The $^1$H NMR spectra of a quaternary CTAB microemulsion system were also acquired as a function of pH. In this system pentanol was employed as the cosurfactant. The same trend in coalescence was observed (Appendix 10) with the point of coalescence occurring at an aqueous phase pH of 3.4. Having investigated the change in relaxation times of water for CTAB RMs a non-ionic based microemulsion was investigated. Reverse micelles composed of the non-ionic surfactant Triton X-100 (TX) were investigated in the quaternary system TX-cyclohexane-hexanol-aq. Relaxation times for the droplet water (4.23 ppm), as a function of pH, are shown in Figure 4.11. As seen in the CTAB systems, the $T_1$ values remain constant whilst the $T_2$ relaxation times decrease as the pH decreases below ≈ pH 3, to a minimum at pH 1.9 before a rapid increase in $T_2$ occurs as the pH drops further to pH 1. $^1$H NMR

spectra for the same system, over the pH range 1.8 – 2.5, are shown in Figure 4.12; the water peak appears at a chemical shift of 4.23 ppm, with the alcoholic hydroxyl group at 4.66 ppm. As the pH decreases, these two peaks move together and start to merge at a pH of approximately 1.9, following which the peak linewidth continues to decrease.

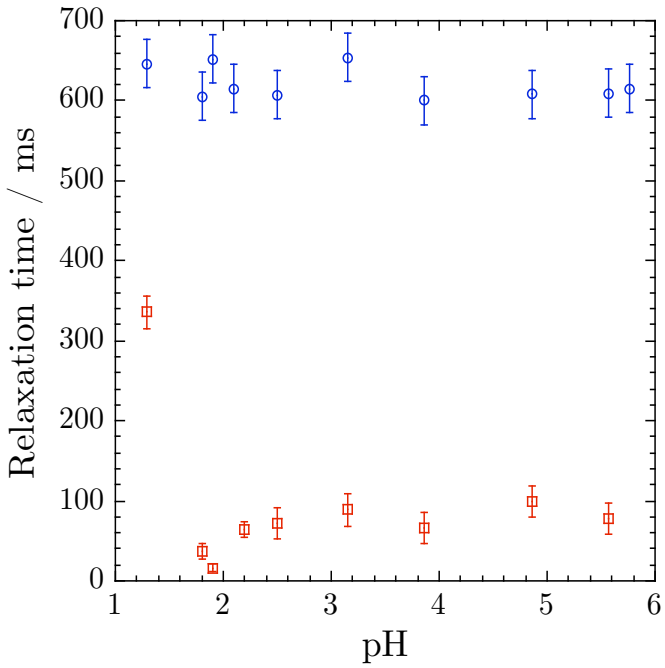


Figure 4.11: $T_1$ (○) and $T_2$ (□) relaxation times of water in TX-cyclohexane-hexanol-aq microemulsions ($\omega_0 = 8.2$ and $\phi_d = 0.3$) for a pH range. The pH is the measured pH of the aqueous stock solution prior to uptake in the microemulsion. Error bars represent the standard deviation from three experimental repeats.

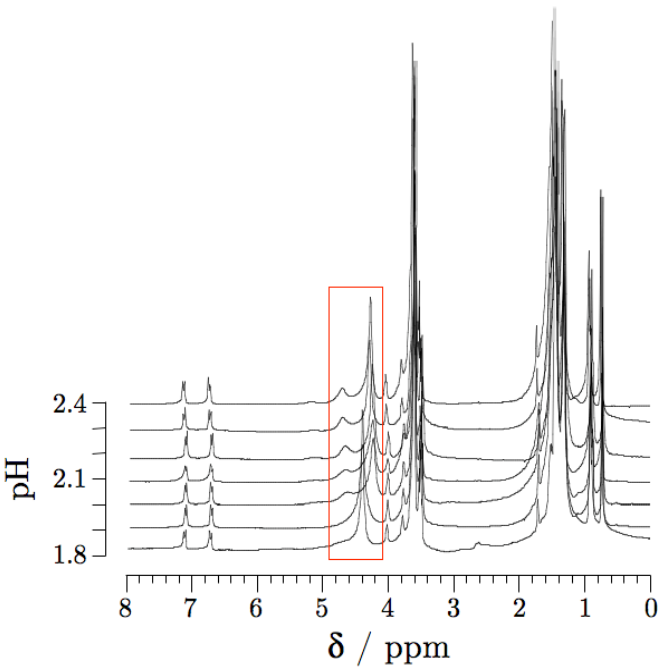


Figure 4.12: $^{1}$H NMR spectra of TX-cyclohexane-hexanol-aq microemulsions ($\omega_0$ = 8.2 and $\phi_d$ = 0.3) over an aqueous stock solution pH range 1.8 -2.4. The hydroxyl peaks are outlined in red. The cyclohexane peak has been cropped in the images.

Relaxation times of water confined in RMs that do not utilise an alcohol co-surfactant were also investigated. Reverse micelles of AOT were formed in an AOT-octane-aq w/o μE; the relaxation times of water confined in these droplets are shown in Figure 4.13 as a function of pH. Both $T_1$ and $T_2$ relaxation times remain unaffected by a change in the pH. DLS experiments were also performed and the data, which, unlike the CTAB data, were suitable for use according to the sample report, are shown in Figure 4.14. The hydrodynamic diameter was found to be approximately 9 nm with no significant change observed with pH.

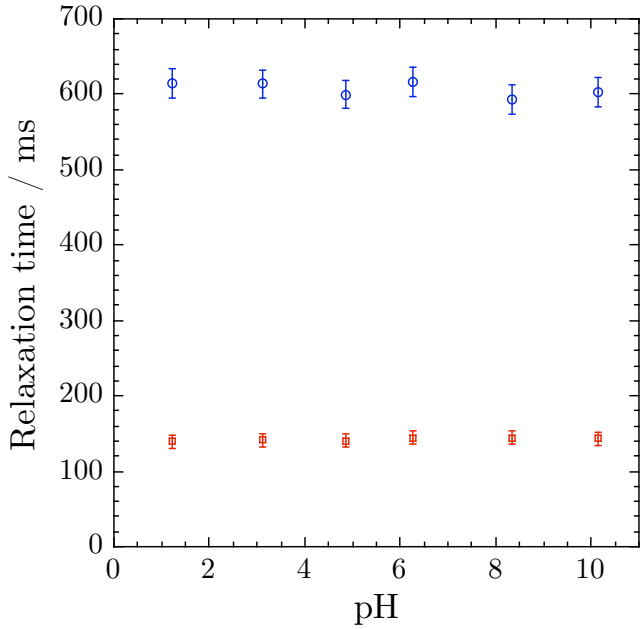


Figure 4.13: $T_1$ (○) and $T_2$ (□) relaxation times of water in AOT-octane-aq microemulsions ($\omega_0$ = 8.2 and $\phi_d$ = 0.4) for a pH range. The pH is the measured pH of the aqueous stock solution prior to uptake in the microemulsion. Error bars represent the standard deviation from 3 experimental repeats.

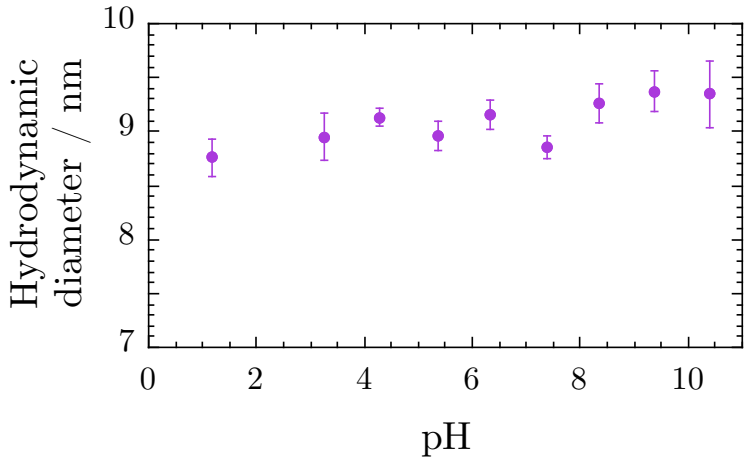


Figure 4.14: A graph to show the hydrodynamic radius determined by DLS measurements of AOT-octane-aq microemulsions ($\omega_0$ = 8.2 and $\phi_d$ = 0.4) as a function of pH. The pH is the measured pH of the aqueous stock prior to uptake into reverse micelles. The error bars show the standard deviation of five experimental repeats.

In order to determine whether the exchange process between the water and hexanol hydroxyl protons could be used to monitor pH changes during the bromate-sulfite reaction a series of spectra were collected over time, three of which are shown in Figure 4.15.

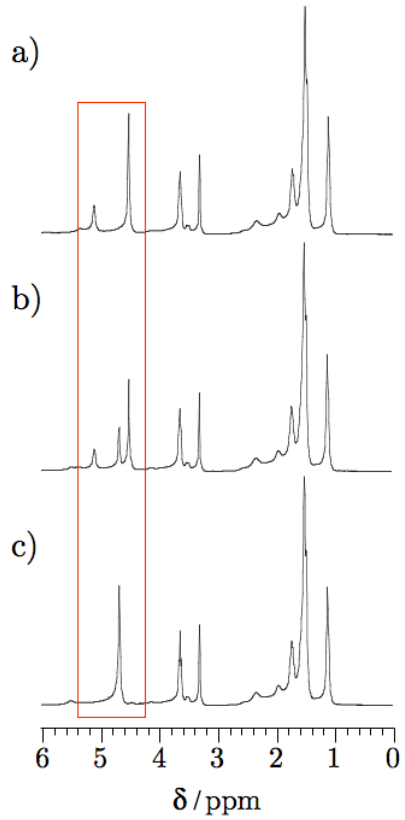


Figure 4.15: $^{1}$H NMR spectra for a bromate-sulfite-CTAB reaction system at time intervals of a) 80 mins, b) 90 mins and c) 110 mins following the mixing of reagent microemulsions.

The spectrum in Figure 4.15a was taken at the start of the reaction during the induction period, when, in aqueous solution, the pH is 7. Two hydroxyl resonances are observed, one for the $H_2O$ (4.50 ppm) protons and one for the $H_a$ (5.12 ppm) hydroxyl protons. The next spectrum (Figure 4.15b), taken mid-way through the reaction, displays a third peak at a chemical shift, δ, of 4.68 ppm in addition to the peaks for the $H_2O$ and $H_a$ hydroxyl protons. At this point in the reaction there will

be regions of the sample that have clocked and regions of the sample that have not clocked. The sample in the magnet is unstirred and thus propagating acidity fronts will be present within the sample; there will be signal contribution from the reactant microemulsion environment and from the acidic product environment. The final spectrum (Figure 4.15c) was collected once the system had fully clocked. In aqueous solution this corresponds to a final pH of 2. The $T_2$ relaxation time for $H_2O$ protons at the start of the reaction was found to be 172 ms and the $T_2$ relaxation time of the coalesced peak at the end of the reaction was found to be 88 ms.

## 4.4 Discussion

The NMR relaxation times of water have been investigated in RMs of the CTAB-hexanol-aq microemulsion system as a function of pH. $T_2$ relaxation times were found to be sensitive to pH values below 6 whilst $T_1$ values remained unaffected for the pH range studied (Figure 4.5). The origins of the $T_2$ pH-dependence were investigated, looking at the influence of proton exchange, ionic strength and $\omega_0$. The $T_2$ relaxation time sensitivity to pH was found to be a result of acid-catalysed proton exchange between protons in the water and alcohol hydroxyl groups in the microemulsion system (Figure 4.8). Acid-catalysed proton exchange is well known in mixtures of water and alcohol[46-53] and was also observed in mixtures of hexanol and water, as a function of pH (Figure 4.9). The comparison of $T_2$ relaxation times in the CTAB microemulsion with the corresponding spectra demonstrated that the minimum $T_2$ relaxation time correlates to the pH at which the water and alcohol proton resonances coalesced and the coalesced peak is broadest.

### 4.4.1 Chemical exchange

The presence of chemical exchange between protons in the water and the hydroxyl groups of hexanol, and its sensitivity to pH, was investigated. Where acid, which acts as a catalyst, is present in solutions of water and alcohol, fast exchange occurs between the protons in the water and the hydroxyl group of the alcohol, leading to a single peak in the NMR spectrum. If all the acid is rigorously excluded, separate resonances are observed for these protons[54]. Separate resonances have been observed for the hydroxyl proton in pentanol and water in a non-ionic microemulsion[29], where no catalyst was present. In an investigation of the N-octylribonamide-brine-decane-butanol microemulsion, the composition of the microemulsion was found to control the rate of proton exchange between the water and hexanol[25]. In the experiments reported here on the CTAB microemulsion, a change in the rate of proton exchange between the water and hydroxyl groups of hexanol was observed as a function of pH; at a pH of 3.6 and higher, separate resonances were clearly observed for the water and hydroxyl groups of hexanol (Figure 4.8), indicating slow exchange. As the pH decreased, the rate of exchange increased, until, at a pH of 3.4, a single resonance was observed. As the rate of exchange continued to increase with an increase in the acid concentration (decrease in pH) the linewidth of this single hydroxyl resonance became narrower. The minimum $T_2$ relaxation time was observed to occur at the pH value where the coalesced peak was broadest.

The observed linewidth broadening and narrowing of the hydroxyl peak(s) in the spectra is coupled to the measured $T_2^*$ relaxation time through the inverse relationship:

$$\Delta\nu = \frac{1}{\pi T_2^*} \tag{4.4}$$

where $\Delta\nu$ is the linewidth associated with relaxation processes and $T_2^*$ is the spin-spin relaxation time. Thus, the observations noted above can be related to the rate of proton exchange through consideration of the spin-spin relaxation mechanism. For pH values greater than 3.4, the rate of proton exchange between the two sites (water and hexanol-OH) is in the slow intermediate regime[55]. In this regime, the transition of spins from one site to another causes the precessional frequency of these spins to suddenly change and a subsequent enhanced decay of the transverse magnetisation occurs, which leads to a decrease in their $T_2$ relaxation time. As the pH decreases from 6 to 3.4, the proton exchange is facilitated by the increased acid concentration, which results in an increased number of transitions between the two sites and subsequent enhancement of transverse magnetisation decay. The associated decrease in the relaxation time thus correlates with a broadening of the hydroxyl proton resonances ($H_a$ and $H_2O$). In this slow intermediate regime the linewidth broadenings, $\Delta\nu_X$, are given by;

$$\Delta\nu_X = \frac{k_X}{\pi} = \frac{1}{\pi\tau_X} \tag{4.5}$$

where subscript X denotes the spin site of interest (i.e. either that of water or that of hexanol), $\tau$ is the average lifetime of the spin at that site and $k$ is the first-order rate constant associated with the exchange mechanism;

$$HX + Y \underset{k_Y}{\overset{k_X}{\rightleftharpoons}} HY + X \tag{4.6}$$

As the pH decreases further still, the exchange rate continues to increase and enters into the fast intermediate regime; a single, coalesced resonance is observed at the crossover point between the two regimes[55] (pH 3.4). In the fast intermediate exchange regime, the decay of the transverse magnetisation gets slower as the exchange rate continues to increase, reflecting the more effective averaging of the precessional frequencies as the number of transitions between the two sites increases ($\tau$ decreases). In this regime the linewidth broadenings are given by:

$$\Delta\nu = \frac{4\pi p_X p_Y (\delta\nu)^2}{k_X + k_Y} \tag{4.7}$$

where $p_X$ and $p_Y$ are the relative populations of sites X and Y, $k$ is again the first-order rate constant associated with the exchange and $\delta\nu$ is the difference in resonance frequencies of the two sites for X and Y. The change in pH from 3.4 to 1.1 therefore demonstrates linewidth narrowing due to the enhanced acid facilitated proton exchange.

### 4.4.2 Ionic strength

Figure 4.1 shows that a change in the ionic strength of the aqueous phase coincides with a change in pH. Ionic strength was calculated as a function of the concentration of all the ions present in solution by assuming complete dissociation, and was found to vary from a minimum value of 0.125 M at pH $\geq$ 4, to a maximum of 0.15 M at pH 1. Ionic strength, $I$, is known to have an effect on the size and structure of droplets inside a microemulsion[40, 41], consequently the effect of $I$ on the properties of water within the droplets of the system were investigated.

Attempts were made to investigate the size of the RMs using DLS and diffusion measurements. DLS techniques have frequently been used to investigate microemulsions, particularly of well-characterised AOT based μE systems[39, 56], however DLS measurements of the CTAB-hexanol-aq μE were inconclusive. An average hydrodynamic diameter of 1.31 ± 0.3 nm was reported for the majority of samples but the software reported that the results did "not meet quality criteria" for all samples. The experiments were repeated for diluted samples in an attempt to remove interactions between droplets of the μEs and thus aid the analysis of the scattered light; these experiments also produced data that did "not meet quality criteria". The unsuitability of the data is most likely to be a consequence of polydispersity within the droplets. Polydispersion of spherical droplets has previously been reported for an analogous dodecyltrimethylammonium chloride microemulsion system[57] and CTAB based RMs with lengths between 100 and 1000 nm have been found to coexist togther[58].

Diffusion measurements were also performed for water within the μE system and were constant, within the margins of error, for the pH range investigated. The measured water diffusion coefficient was found to be relatively low ($1.8 \pm 0.16 \times 10^{-10}$ $m^2$ $s^{-1}$). This measured diffusion coefficient has contributions arising not only from water confined within the droplets but also from the fraction of water dissolved in the oil continuum, and from the exchange processes of water between these media[31, 59]. The presence of "free" water in the continuous oil phase prevents the determination of droplet size from these measurements. Although absolute sizing of the RMs cannot be achieved using PGSE data, the constancy of the diffusion

coefficients indicates that the structure of the μE is not significantly altered as a function of pH. This proposal supports the $T_1$ data acquired.

$T_1$ relaxation times are related to molecular motion through the rotational correlation time, $\tau_c$. The rotational correlation time is regarded as the average time taken for a molecule to tumble through one radian[54] and is inversely proportional to the $T_1$ relaxation time. NMR relaxation times have been measured for increasing water content in w/o microemulsions[27-29, 60, 61]. As the water content of the droplets decreases, $T_1$ is reduced, showing that the water molecules are less mobile $T_1$[27-29, 60, 61]. The mono-exponential behaviour of $T_1$ data for water is a weighted average of the relaxation time of all water within the microemulsion i.e. "bound" water associated with the interface, and bulk water in the droplet core. The simple mono-exponential relaxation behaviour indicates rapid exchange between these environments. A decrease in $T_1$ with a decrease in $\omega_0$ thus reflects an increase in "bound" water and the restricted mobility thereof, and was observed for the measurements performed in this study (Figure 4.10). NMR relaxation times have also been used to investigate packing of hydrophobic surfactant chains in micelles[30]. The results presented for the CTAB μE show that $T_1$ relaxation times were unaffected by a change in the pH and the associated change in ionic strength and therefore demonstrate that the water mobilities remain unaffected.

Investigations were then performed for samples with ionic strength adjusted aqueous phases. Firstly, microemulsions were prepared with neutral aqueous phase stock solutions that were ionic strength adjusted using LiCl. The relaxation times for these microemulsions were constant over the range of $I$ investigated. The ionic

strength was also increased by increasing the concentration of the acid and base used to vary the pH of the aqueous phase. Again, $T_1$ relaxation times were constant for all samples. A change in the absolute $T_2$ relaxation time, at a given pH, was observed but the same trend in behaviour was still found. The pH-dependent relaxation time behaviour therefore cannot be explained by a change in ionic strength, but the coalescence point and hence rate of exchange is affected by ionic strength. An increase in $I$ correlated to an increase in the pH at which coalescence occurred i.e. with increasing $I$, a lower acid concentration was required in order for proton exchange to enter the fast intermediate regime. This may be due to a decreased $pK_a$ of the alcohol and water with an increase in $I$.

### 4.4.3 Coalescence point

The pH at which coalescence occurred was found to be dependent on the system. The coalescence pH in the hexanol/water mixture was found to be higher than the CTAB microemulsion, at a pH of 3.7 compared to pH 3.4. This difference could be due to how the pH was defined, which was as the pH of the aqueous phase prior to formation of RMs or mixture preparation. Whether the macroscopic definition of pH remains valid following the encapsulation of water is unknown. The effect of inherent differences between the mixtures, such as those of the water environment i.e. the presence of a charged interface in the RMs, and the relative concentrations are also unquanitifed and will contribute to the rate of proton exchange and hence the coalescence point. The sensitivity of the coalescence point to ionic strength has already been discussed (section 4.4.2) and was found to move to higher pH with increasing ionic strength. The point at which coalescence occurs also changed with $\omega_0$ and was observed to shift to higher pH as $\omega_0$ increased.

### 4.4.4 Effects of $\omega_0$

An increase in $\omega_0$ correlated to an increase in the pH at which coalescence occurred. The first-order reaction rates of the proton exchange mechanism in equation 6 is concentration dependent and thus this shift in the coalescence point could be a consequence of a change in the proportions of hexanol and water. However, the change in the electrostatic nature of the interface with $\omega_0$ may also contribute to the kinetics of the reaction. The chemical shifts of the hydroxyl resonances also change with $\omega_0$ and are observed to shift downfield as $\omega_0$ increases. This has been observed in w/o microemulsions and has been explained by considering not only concentration effects but also the increased hydrogen bonding of the bulk-like water as $\omega_0$ increases[61]. The breaking of the hydrogen-bonding network of water in the interfacial region would result in an upfield shift of the water proton resonance.

The chemical shift position of the coalesced peak was also affected by $\omega_0$; an increase in $\omega_0$ reduced the change in the resonance frequency of water and increased the change in the resonance frequency of the hexanol-OH proton spin. In the fast intermediate exchange regime, the single resonance of the coalesced peak is observed at a weighted average of the chemical shifts for the two separate resonances (i.e. $\delta_{H_2O} = 4.50$ ppm, $\delta_{H_a} = 5.12$ ppm for microemulsions with $\omega_0 = 8.3$ and $\phi_d = 0.4$) and is dependent upon the relative populations, $p$, of the spin resonances (equation 4.8).

$$\nu_{average} = p\nu_{H_2O} + p\nu_{H_a} \qquad (4.8)$$

The observed difference in the position of the coalesced peak is thus indicative of an increase in the population of water protons undergoing exchange, relative to the

population of hexanol-OH protons. Proton exchange between water and hexanol can occur only where the hydroxyl moieties of the molecules are in close proximity, thus exchange occurs mainly at the interface within the RMs. Here, water at the interface neighbours the hydrophilic alcohol group of the co-surfactant hexanol molecules. As $\omega_0$ increases the radius of the RM increases and the surface area-to-volume ratio of the spherical droplets decreases, effectively increasing the relative population of water to hexanol at the interface.

### 4.4.5 Exchange rates

Whilst the variations in coalescence-pH with $\omega_0$ and $I$ are relatively small, they currently prevent a measure of pH inside the RM with absolute certainty. However, by looking at relaxation times or spectra, it remains possible to closely monitor variations in pH. A thorough evaluation of the $T_2$ relaxation times and rate of proton exchange as a function of pH also remains challenging: NMR lineshapes and relaxation times cannot be related in a simple way to the rate of proton exchange in the highly complex μE systems since too many unknown parameters remain. The exchange rate of hexanol between the micelle interface and continuous phase, and the relative proportion of hexanol in the interface are two examples of current uncertainties. Certainly, the use of equation 4.8 is not possible; the populations of both hexanol and water participating in the hydroxyl-proton exchange mechanism remain unknown. Further information is required regarding the size of the RMs and the structure of the interface before this equation (and others of its type) can be used to provide quantitative measures.

### 4.4.6 pH in the bromate-sulfite system

Although challenges remain defining pH within a microemulsion droplet, the results here demonstrate that by following the relationship between proton exchange and pH, for a microemulsion of known composition, it becomes possible to observe the variation of pH inside the droplet, without the need for a probe molecule. This was demonstrated in the study of the bromate-sulfite-CTAB reaction. By acquiring spectra over time, and using one of the calibration plots of $T_2$ against pH from Figure 4.6, it was possible to monitor the pH change during the reaction. Using the calibration plot at an ionic strength of 0.3 M (which closely corresponds to the ionic strength of the reaction[1]) the initial and final $T_2$ relaxation values (172 ms and 88 ms) were found to relate to pH values of 7.1 and 2.8, respectively. The final and initial pH values in aqueous solution, for this reaction, are typically 7 and 2, respectively. Measurements of the pH change in this reaction have been made previously using a glass pH electrode[1], and were also found to be higher in the CTAB microemulsion than in aqueous solution. The measured pH of the bromate-sulfite-CTAB system in chapter 2 showed a pH change from 8.2 to 3.6; again, these measurements were made with a glass electrode and therefore cannot preferentially probe the microscopic pH. The origins of these differences remain uncertain and require further investigation.

For the relaxation versus pH plots presented in this chapter the measured pH has been that of the aqueous stock prior to uptake into the RMs. Thus, if the aqueous product environment of the bromate-sulfite reaction has a pH of two, one may expect that the measured relaxation time of the bromate-sulfite-CTAB system corresponds to a pH of two as defined for the experiments presented here, and not a

pH = 2.8. However, the bromate-sulfite reaction is exothermic ($\Delta H$ = –1070 ± 10 kJ $mol^{-1}$) and has an isothermal density change (+ 2.40 × $10^{-4}$ g $cm^{-3}$) between products and reactants[62]. Temperature is known to affect the structure of microemulsions[63, 64] thus the apparent difference in pH may be due to temperature effects on both the microemulsion structure and/or the relaxation processes within the microemulsion ($T_1$ is temperature dependent[55]). The work presented in this chapter demonstrates that a change in pH does not affect the structure of the microemulsion but does have an effect on proton-transfer reaction kinetics. Changes in the structure of the microemulsion therefore, that may occur as a consequence of the bromate-sulfite reaction cannot be attributed to a change in the pH.

### 4.4.7 Applicability

The wider applicability of this technique as a means to probe pH was tested by investigating a non-ionic microemulsion system (Triton X-100-cyclohexane-hexanol-aq) which uses an alcohol as a co-surfactant. It was found that the same pH-dependent exchange behaviour was observed, providing a means to probe the pH for water inside RMs of this system. In the Triton X-100 system the same trend in $T_2$ relaxation time was observed but the coalescence pH occurred at a higher acid concentration than the CTAB microemulsion (Figures 4.11 and 4.12). It is likely that the highly charged interface of the CTAB RM facilitates the proton exchange mechanism, compared to the non-ionic TX RM interface, by polarising the hydroxyl moiety and thus assisting proton dissociation. Again, however, more information is required regarding the structure of the system to allow for a more complex analysis of the exchange kinetics within the system. A control experiment was performed whereby the relaxation times of water were measured for a w/o μE that does not

have an alcohol in its composition; $T_1$ and $T_2$ relaxation times remained constant for the pH range as did the measured size of the droplets (Figures 4.13 and 4.14).

## 4.5 Conclusions and further work

NMR relaxation times have been used to probe pH in RMs of the w/o CTAB-hexanol-aq microemulsion system. $T_1$ relaxation times were found to be unaffected by a change in pH but $T_2$ relaxation times were found to be sensitive to pH values below 6. The origins of this pH-dependent behaviour were investigated; it was found that $T_2$ relaxation times changed as a function of the rate of proton exchange between water and hydroxyl groups of the cosurfactant alcohol. A minimum $T_2$ relaxation time corresponded to the pH at which the exchange rate entered the fast intermediate regime and where the two separate hydroxyl proton resonances coalesced to give a single broad resonance. The position of the $T_2$ minimum was then investigated as a function of $\omega_0$ and ionic strength; it was found that there was a small shift to higher pH with increasing ionic strength and $\omega_0$. This increase to a higher pH infers that an increase in $\omega_0$ and ionic strength favours the proton exchange mechanism, since a lower concentration of acid is required for the exchange to be in the fast intermediate regime. Spectra have been acquired for w/o μEs as a function of pH and have demonstrated linewidth broadening and narrowing of hydroxyl peaks. The relationship between peak linewidths and kinetics of the proton exchange mechanism has been discussed; however, fully quantitative analysis of the data is not possible at this time. Further information regarding the size of RMs and the structure of the interface in the system is required before thorough analyses of kinetic data can be performed. Although the data have shown that pH has an effect on the kinetics of proton exchange within the system, the data have demonstrated

that the structure of the microemulsion remains unaffected by a change in pH; $T_1$ values and diffusion measurements remain constant over a pH range.

Although the question of how to precisely define pH within the water core of the reverse micelles has not been addressed, these experiments demonstrate a unique way to monitor pH changes for a given microemulsion system without the need to include additional probe molecules in the RM composition. An application of this was demonstrated in the investigation of pH changes produced during the bromate-sulfite-CTAB reaction. The measured pH was determined using a calibration curve plotted for relaxation measurements versus pH of a w/o microemulsion having the same water-to-surfactant ratio and droplet fraction as that used for the reaction. It is anticipated that this method can be applied to most microemulsions that utilise an alcohol as a cosurfactant, thus eliminating the need for a probe molecule. The findings discussed in this chapter and the conclusions that have been drawn have been presented in the Journal of Physical Chemistry B (Appendix 11).

## 4.6 References


[1] R. E. McIlwaine, H. Fenton, S. K. Scott, A. F. Taylor, *Journal of Physical Chemistry C* **2008**, *112*, 2499.

[2] K. Bhattacharyya, B. Bagchi, *Journal of Physical Chemistry A* **2000**, *104*, 10603.

[3] F. M. Menger, G. Saito, *Journal of the American Chemical Society* **1978**, *100*, 4376.

[4] K. M. Manoj, R. Jayakumar, S. K. Rakshit, *Langmuir* **1996**, *12*, 4068.

[5] S. M. Andrade, S. M. B. Costa, *Photochemical & Photobiological Sciences* **2002**, *1*, 500.

[6] N. E. Levinger, *Science* **2002**, *298*, 1722.

[7] M. Hasegawa, T. Sugimura, Y. Shindo, A. Kitahara, *Colloids and Surfaces a-Physicochemical and Engineering Aspects* **1996**, *109*, 305.

[8] R. E. Riter, D. M. Willard, N. E. Levinger, *Journal of Physical Chemistry B* **1998**, *102*, 2705.

[9] E. Rodenas, M. Valiente, *Colloids And Surfaces* **1992**, *62*, 289.

[10] R. Bru, A. Sanchezferrer, F. Garciacarmona, *Biochemical Journal* **1995**, *310*, 721.

[11] R. E. Smith, P. L. Luisi, *Helvetica Chimica Acta* **1980**, *63*, 2302.

[12] M. D. Miguel, H. D. Burrows, M. A. E. Pereira, A. P. Varela, in *12th International Symposium on Surfactants in Solution (SIS)*, Elsevier Science Bv, Stockholm, Sweden, **1998**, p. 85.

[13] M. Aoudia, M. A. J. Rodgers, *Journal of Physical Chemistry B* **2003**, *107*, 6194.

[14] O. A. El Seoud, A. M. Chinelatto, M. R. Shimizu, *Journal of Colloid and Interface Science* **1982**, *88*, 420.

[15] H. Fujii, T. Kawai, H. Nishikawa, *Bulletin of the Chemical Society of Japan* **1979**, *52*, 2051.

[16] M. Hasegawa, *Langmuir* **2001**, *17*, 1426.

[17] M. B. Lay, C. J. Drummond, P. J. Thistlethwaite, F. Grieser, *Journal of Colloid and Interface Science* **1989**, *128*, 602.

[18] S. Biswas, S. C. Bhattacharya, B. B. Bhowmik, S. P. Moulik, *Journal of Colloid and Interface Science* **2001**, *244*, 145.

[19] D. C. Crans, C. D. Rithner, B. Baruah, B. L. Gourley, N. E. Levinger, *Journal of the American Chemical Society* **2006**, *128*, 4437.

[20] J. J. Rack, T. M. McCleskey, E. R. Birnbaum, *Journal of Physical Chemistry B* **2002**, *106*, 632.

[21] M. Saez, E. A. Abuin, E. A. Lissi, *Langmuir* **1989**, *5*, 942.

[22] B. Baruah, L. A. Swafford, D. C. Crans, N. E. Levinger, *Journal of Physical Chemistry B* **2008**, *112*, 10158.

[23] *Micelles*, Springer-Verlag, Berlin ; New York, **1980**.

[24] B. Lindman, U. Olsson, *Berichte Der Bunsen-Gesellschaft-Physical Chemistry Chemical Physics* **1996**, *100*, 344.

[25] F. Bastogne, B. J. Nagy, C. David, *Colloids and Surfaces a-Physicochemical and Engineering Aspects* **1999**, *148*, 245.

[26] J. B. Nagy, I. Bodartravet, E. G. Derouane, A. Gourgue, J. P. Verfaillie, *Colloids And Surfaces* **1989**, *36*, 229.

[27] M. Wong, J. K. Thomas, T. Nowak, *Journal of the American Chemical Society* **1977**, *99*, 4730.

[28] A. Llor, P. Rigny, *Journal of the American Chemical Society* **1986**, *108*, 7533.

[29] D. Waysbort, S. Ezrahi, A. Aserin, R. Givati, N. Garti, *Journal of Colloid and Interface Science* **1997**, *188*, 282.

[30] S. Zhao, H. Z. Yuan, J. Y. Yu, Y. R. Du, *Colloid and Polymer Science* **1998**, *276*, 1125.

[31] J. Xu, G. Z. Li, Z. Q. Zhang, G. W. Zhou, K. J. Ji, *Colloids And Surfaces A-Physicochemical And Engineering Aspects* **2001**, *191*, 269.

[32] C. J. Ko, Y. J. Ko, D. M. Kim, H. J. Park, *Colloids And Surfaces A-Physicochemical And Engineering Aspects* **2003**, *216*, 55.

[33] P. Ekwall, L. Mandell, K. Fontell, *Journal Of Colloid And Interface Science* **1969**, *29*, 639.

[34] G. Colafemmina, G. Palazzo, E. Balestrieri, M. Giomini, M. Giustini, A. Ceglie, in *Trends in Colloid and Interface Science Xi, Vol. 105* (Eds.: J. B. Rosenholm, B. Lindman, P. Stenius), **1997**, p. 281.

[35] H. Wei, L. L. Zhou, J. Li, J. F. Liu, E. K. Wang, *Journal Of Colloid And Interface Science* **2008**, *321*, 310.

[36] J. M. Wu, H. Yan, X. H. Zhang, L. Q. Wei, X. G. Liu, B. S. Xu, *Journal Of Colloid And Interface Science* **2008**, *324*, 167.

[37] P. Stilbs, K. Rapacki, B. Lindman, *Journal Of Colloid And Interface Science* **1983**, *95*, 583.

[38] Y. Bayrak, M. Iscan, *Colloids And Surfaces A-Physicochemical And Engineering Aspects* **2005**, *268*, 99.

[39] T. K. De, A. Maitra, *Advances In Colloid And Interface Science* **1995**, *59*, 95.

[40] P. Guering, B. Lindman, *Langmuir* **1985**, *1*, 464.

[41] K. Hamada, T. Ikeda, T. Kawai, K. Kon-No, *Journal of Colloid and Interface Science* **2001**, *233*, 166.

[42] V. K. Vanag, *Physics-Uspekhi* **2004**, *47*, 923.

[43] E. W. Flick, *Industrial solvents handbook*, 5th ed., Noyes Data Corp., Westwood, N.J., **1998**.

[44] R. C. Weast, *CRC handbook of chemistry and physics*, 1st Student ed., CRC Press, Boca Raton, FL, **1988**.

[45] H.-z. Yuan, X.-j. Miao, S. Zhao, L.-f. Shen, J.-y. Yu, Y.-r. Du, *Magnetic Resonance in Chemistry* **2001**, *39*, 33.

[46] T. Fukumi, Y. Fujiwara, Y. Arata, S. Fujiwara, *Bulletin of the Chemical Society of Japan* **1968**, *41*, 41.

[47] J. Oakes, *Journal of the Chemical Society-Faraday Transactions Ii* **1973**, *69*, 1311.

[48] W. G. Paterson, *Canadian Journal of Chemistry-Revue Canadienne De Chimie* **1963**, *41*, 2472.

[49] A. Coccia, P. L. Indovina, F. Podo, V. Viti, *Chemical Physics* **1975**, *7*, 30.

[50] B. P. Hills, *Journal of the Chemical Society-Faraday Transactions* **1990**, *86*, 481.

[51] J. R. Kuppers, N. E. Carriker, *Journal of Magnetic Resonance* **1971**, *5*, 73.

[52] Z. Luz, D. Gill, S. Meiboom, *Journal Of Chemical Physics* **1959**, *30*, 1540.

[53] M. D. Bruch, *NMR spectroscopy techniques*, 2nd ed., M. Dekker, New York, **1996**.

[54] P. J. Hore, *Nuclear Magnetic Resonance* Oxford University Press, Oxford, **1995**.

[55] M. H. Levitt, *Spin dynamics*, John Wiley and Sons Ltd, Chichester, **2001**.

[56] A. Salabat, J. Eastoe, K. J. Mutch, R. F. Tabor, *Journal Of Colloid And Interface Science* **2008**, *318*, 244.

[57] C. Petit, A. S. Bommarius, M. P. Pileni, T. A. Hatton, *Journal Of Physical Chemistry* **1992**, *96*, 4653.

[58] X. L. Fang, C. F. Yang, *Journal of Colloid and Interface Science* **1999**, *212*, 242.

[59] M. Giustini, G. Palazzo, G. Colafemmina, M. DellaMonica, M. Giomini, A. Ceglie, *Journal of Physical Chemistry* **1996**, *100*, 3190.

[60] L. J. Schwartz, C. L. DeCiantis, S. Chapman, B. K. Kelley, J. P. Hornak, *Langmuir* **1999**, *15*, 5461.

[61] J. R. Hansen, *Journal Of Physical Chemistry* **1974**, *78*, 256.

[62] A. Keresztessy, I. P. Nagy, G. Bazsa, J. A. Pojman, *Journal Of Physical Chemistry* **1995**, *99*, 5379.

[63] L. K. Shrestha, T. Sato, K. Aramaki, *Journal of Physical Chemistry B* **2007**, *111*, 1664.

[64] A. Merdas, M. Gindre, R. Ober, C. Nicot, W. Urbach, M. Waks, *Journal Of Physical Chemistry* **1996**, *100*, 15180.

# 5 Magnetic resonance imaging of the bromate-sulfite reaction in a CTAB microemulsion

## 5.1 Introduction

The coupling of non-linear reaction kinetics with heterogeneous media is an area of great interest to scientists[1]. The heterogeneous medium can allow for greater control over the reaction; diffusive properties of the system can be altered and compartmentalisation of reactants can be achieved. The synergy between the nonlinear reaction and the medium in which the reaction is performed can create a diverse range of waves and patterns that mimic phenomena observed in the natural world[2]. Investigations by McIlwaine *et al.*[3] of an autocatalytic pH reaction performed in water-in-oil microemulsions (w/o μEs) have demonstrated propagating acidity fronts with structures that are not observed in the homogeneous aqueous phase[3, 4]. A possible feedback mechanism between the nonlinear chemical reaction and changes in thermodynamic structure of microemulsions with the evolution of heat and acid during the reaction is proposed[3]. The understanding of reaction-diffusion fronts and their structures is important due to their universal presence in nature[5], for example, calcium waves in cells[6] and heat autocatalysed flame fronts[7].

The investigation by McIlwaine *et al.*[3] used a charge-coupled device camera to image fronts within the system. The limitation with this technique is that acquired images show an integrated measurement of the sample that represents the sample width.

This limitation hinders the characterisation of front behaviour and may also result in features at the centre of larger samples being masked by the surrounding sample. Magnetic resonance imaging (MRI) is an ideal technique with which to observe these fronts; the technique is able to non-invasively probe the sample and image through the sample by the acquisition of multiple narrow slices. It is thus possible to distinguish between behaviour at the edge of the sample and the centre of the sample: This allows for a more detailed and thorough description of the front behaviour. MRI has previously been used to provide insight into chemical waves in various systems[8-14], although to date, pH fronts in heterogeneous media have not been investigated using this technique.

Magnetic resonance image contrast allows regions of different chemical and physical composition to be distinguished and arises from variations of signal intensity between neighbouring pixels in the image. Variation in signal intensity can arise through differences in spin-density or when the magnetic resonance (MR) properties of protons in separate chemical or physical environments differ; these properties include $T_1$ and $T_2$ relaxation times and resonance frequencies. By utilising pulse programs and experimental parameters that exploit these differences, image contrast can be obtained. Often, paramagnetic contrast agents are employed[14-17] to enhance the differences in relaxation rates between separate chemical environments. Image contrast in the autocatalytic oscillatory Belousov-Zhabotinsky reaction has been achieved via the presence of transition metal-ions that catalyse the reaction and oscillate between two oxidation states during the reaction[8]. Similarly, imaging of the travelling wave formed during the reaction of a cobalt(II)-ligand complex with hydrogen peroxide was achieved due to the conversion of paramagnetic cobalt(II)-

complex ions to diamagnetic cobalt(III)-complex ions[9]. In the aqueous bromate-sulfite reaction the pH dependent chelation of paramagnetic metal ions and chelating ligands was used to provide image contrast (Chapter 3).

The examples listed above used MRI to investigate aqueous reaction systems, however, in the bromate-sulfite microemulsion system, although reaction occurs in the aqueous pseudophase, signal intensity contributions arise from protons in the surfactant and oil molecules, in addition to those contributions from water protons. As was discussed in the previous chapter, the relaxation times of CTAB and hexanolic protons in the CTAB microemulsion are mainly unaffected by pH changes; this indifference to pH has significant implications for obtaining contrast between the reactant and product bromate-sulfite-CTAB environments. Certainly, the RARE imaging sequence utilised to image the aqueous bromate-sulfite reaction (Chapter 3) is unsuitable for imaging the bromate-sulfite-CTAB system; the signal would be dominated by contributions from CTAB and hexanol nuclear spins. It may thus be necessary to suppress the contribution of these spins to allow investigation of the nuclei of interest, i.e. those of water and hexanol-hydroxyl (hexanol-OH) protons, whose magnetic resonance properties are affected by pH. Signal suppression is commonly used in medical MRI where it is often necessary to discriminate between water and adipose tissue[18]. The electronic shielding of protons in oil molecules is greater than that experienced by protons in water molecules, which results in different microscopic magnetic fields and subsequently, different proton resonances. In 1985, Haase *et al.*[19, 20] reported a chemical shift selective (CHESS) pulse sequence that selectively excited a predetermined frequency range of spins. These spins were then suppressed prior to use of an imaging sequence. MR images were thus obtained

where the spin-density contribution resulted from only protons of the chemical shift, δ that was not suppressed. Similarly, a chemically selective excitation radiofrequency (rf) pulse can be used with images obtained that show spin-densities of only those excited nuclei[21].

The work presented in the previous chapter probed the pH in μEs using NMR techniques; the magnetic resonance properties of the oil and surfactant component remained largely unaffected whilst a change in MR properties of the water signal were observed resulting from acid catalysed proton exchange between water and hexanol-OH protons. The work presented in this chapter investigates the use of MRI techniques to image propagating reaction-diffusion fronts in the bromate-sulfite-CTAB system. The studies presented in chapter 2 will be continued to investigate the effect of a pH-dependent paramagnetic metal–complex on the microemulsion. Also, the efficacy of a chemically selective excitation pulse sequence for the imaging of propagating acidity fronts in the bromate-sulfite-CTAB system will be investigated.

## 5.2 Experimental

### 5.2.1 Sample preparation

#### *5.2.1.1 Stock solution preparation*

All stock solutions were prepared using high-purity water (Nanopure filtered, 18.0 MΩ cm).

*i) Preparation of 1 M $H_2SO_4$*

Sulfuric acid (1 M) was prepared by diluting 27.2 mL concentrated sulfuric acid (18.4 M, Fisher) in a 500 mL volumetric flask with water.

*ii) Preparation of 1 M NaOH*

A 1 M solution of sodium hydroxide was prepared by dissolving 19.998 g NaOH pellets (≥ 98 %, Fluka) in a 500 mL volumetric flask.

*iii) Preparation of 0.125 M $CuSO_4$*

A 0.125 M copper sulfate solution was prepared by dissolving 1.994 g $CuSO_4$ (Sigma) in a 100 mL volumetric flask.

*iv) Preparation of triethylenetetramine (trien) solution*

A solution of trien was prepared with a minimum concentration of 0.0625 M by dissolving 1.219 g $NH_2CH_2CH_2(NHCH_2CH_2)_2NH_2.xH_2O$ (Aldrich) in 100 mL water. The trien was supplied as a hydrate with the molecular mass unknown, however, the specification sheet listed typically 19-24 % $H_2O$. An overestimation of the water content was used (25 %) to calculate a minimum concentration of the stock solution.

*5.2.1.2 Preparation of aqueous phase solutions*

Again, all solutions were prepared using high-purity water (Nanopure filtered, 18.0 MΩ cm).

*i) Preparation of 2 mM Cu(II)trien solutions over a pH range*

An acidic (0.05 M $H_2SO_4$) solution of Cu(II)trien (2 mM) was prepared by diluting 5 mL $H_2SO_4$ (1 M stock), 3.2 mL trien (0.0625 M stock) and 1.6 mL $CuSO_4$ (0.125 M stock) with water up to 100 mL. A basic (0.1 M NaOH) solution of Cu(II)trien (2 mM) was also prepared by diluting 25 mL NaOH (1 M stock), 8 mL trien (0.0625 M stock) and 4 mL $CuSO_4$ (0.125 M stock) with water up to 250 mL. Solutions of 2 mM Cu(II)trien were made over a pH range of 1.1-10.0 by titrating basic 2 mM Cu(II)trien solution was against acidic 2 mM Cu(II)trien solution. The pH was

measured using a combination glass electrode (purchased from Radleys) connected to a digital pH meter (Orion 720A). The electrode and pH meter were calibrated with pH 10, 7 and 4 standard buffers (Sigma-Aldrich) each day that they were used. Since the metal-chelate concentration was the same for both the titrate and titrand, the overall concentration of the metal-chelate remained the same throughout.

*ii) Preparation of bromate-sulfite reagent solutions*

Solution 1 was prepared by dissolving $NaBrO_3$ (1.51 g, Aldrich) in 100 mL water to give a $BrO_3^-$ concentration of 0.1 M. Solution 2 was prepared by dissolving sodium sulfite (1.26 g, Sigma-Aldrich) in water and adding 1 M stock sulfuric acid (1.5 mL), before diluting to 100 mL. This gave buffer solution 2 with equilibrium concentrations of sulfite and bisulfite equal to 0.07 M and 0.03 M respectively (please see Chapter 2, section 2.2.1.1iii).

*iii) Preparation of 2 mM Cu(II)trien bromate-sulfite reagent solutions*

Paramagnetic bromate solution (solution 3) was prepared by dissolving $NaBrO_3$ (1.51 g, Aldrich) in water, adding 3.2 mL trien (0.0625 M stock) and 1.6 mL $CuSO_4$ (0.125 M stock) and diluting to 100 mL. This gave solution 3 with a $BrO_3^-$ concentration of 0.1 M and a Cu(II)trien concentration of 2 mM. Paramagnetic buffer solution (solution 4) was prepared by dissolving sodium sulfite (1.26 g, Sigma-Aldrich) in water, adding 1 M stock sulfuric acid (1.5 mL), 3.2 mL trien (0.0625 M stock) and 1.6 mL $CuSO_4$ (0.125 M stock) and diluting to 100 mL. This gave solution 3 with a Cu(II)trien concentration of 2 mM and equilibrium concentrations of sulfite and bisulfite equal to 0.07 M and 0.03 M, respectively.

*5.2.1.3 Preparation of CTAB microemulsions*

Hexanol-aq-CTAB microemulsions were prepared by dissolving 6.1 g CTAB (> 98%, Sigma) in 14 mL 1-hexanol (Acros) to which 2.5 mL aqueous solution was added. This gave μEs with a water-to-surfactant ratio, $\omega_0$, of 8.3 and a droplet fraction, $\phi_d$, of 0.4. Formation of the microemulsions was endothermic and so sufficient time was allowed for the μEs to reach room temperature before use (approximately 25 minutes). For spectral and relaxation time investigations an aliquot of the μEs was transferred to a 5 mm o.d. NMR tube and placed in the bore of the magnetic resonance spectrometer. For imaging experiments phantom samples were made and used (see section 5.2.1.4).

*i) Preparation of μEs with an aqueous pseudophase over a pH range 1.1–10 and 2 mM Cu(II)trien*

The aqueous solution was taken from the titrand (Section 5.2.1.2i) at approximate integer pH values.

*ii) Preparation of bromate-sulfite reactant μEs*

The preparation of reagent bromate-sulfite μEs samples has been described elsewhere and the reader is referred to section 2.2.1 for details. Two reagent μEs were prepared; μE 1 had an aqueous phase of solution 1 (5.2.1.2ii) and μE 2 had an aqueous phase of solution 2 (5.2.1.2ii). The two separate reagent μEs were mixed to give the bromate-sulfite CTAB (bromate-sulfite-CTAB) system with an aqueous pseudophase $[BrO_3^-]$ = 0.05 M, $[SO_3^{2-}]$ = 0.035 M and $[HSO_3^-]$ = 0.015 M. Reactant bromate-sulfite-CTAB samples were used immediately. Product state microemulsions were obtained by allowing the reaction to proceed in a closed vessel, and were used within 24 hours of the reaction occurring.

*iii) Preparation of bromate-sulfite reactant μEs with 2 mM Cu(II)trien aqueous pseudophase*

Two paramagnetic reagent μEs were prepared (μE 3 and μE 4): μE 3 had an aqueous phase of solution 3 (5.2.1.2iii) and μE 4 had an aqueous phase of solution 4 (5.2.1.2iii). The two separate reagent μEs were mixed to give the bromate-sulfite CTAB (bromate-sulfite-CTAB) system with aqueous pseudophase concentrations of; $[BrO_3^-]$ = 0.05 M, $[SO_3^{2-}]$ = 0.035 M, $[HSO_3^-]$ = 0.015 M and 2 mM Cu(II)trien. Reactant bromate-sulfite-CTAB samples were used immediately.

*iv) Preparation of μEs with an aqueous phase of pure water*

Microemulsions were also prepared using an aqueous phase of pure water (Nanopure filtered, 18.0 MΩ cm).

### *5.2.1.4 Preparation of phantom samples*

Phantom samples (phantoms) are often used in the determination of appropriate imaging parameters to not only simplify and assist the process by allowing for a known expected result/observation, but also to remove time constraints caused by, for example, sample degradation. The phantoms used consisted of two concentric tubes with each tube containing a different species that represent the two distinct chemical environments for which contrast is to be obtained (Figure 5.1). Phantoms were used to aid the development of suitable CHESS imaging parameters and to prevent time constraints caused by reaction of bromate-sulfite reactants. All phantoms that were used consisted of a 5 mm o.d. NMR tube filled with solution a placed in a 10 mm o.d. NMR tube filled with solution b using a Teflon spacer (Figure 5.2).

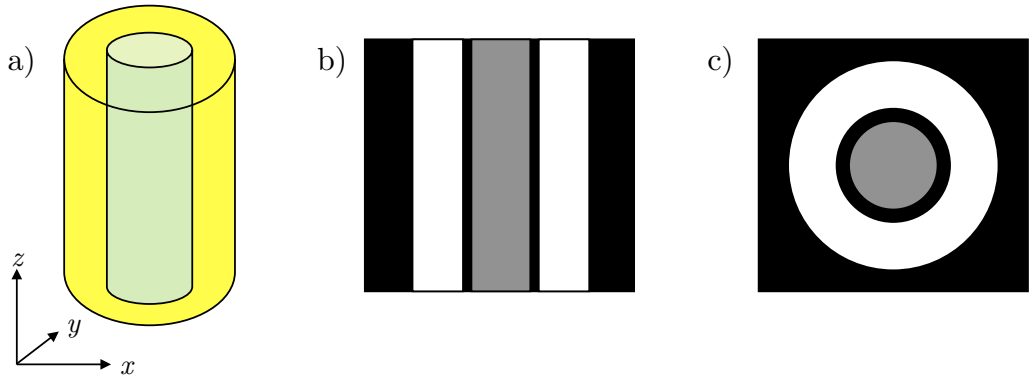


Figure 5.1: Schematic to illustrate a) a phantom consisting of two concentric tubes containing different chemical species, and ideal MR images for b) a vertical slice ($xz$ plane) and c) a horizontal slice ($xy$ plane) through the centre of the sample. Signal intensity is 0 for regions outside of the sample and for glass, and is illustrated here to be greater (brighter) for the species in the outer tube.

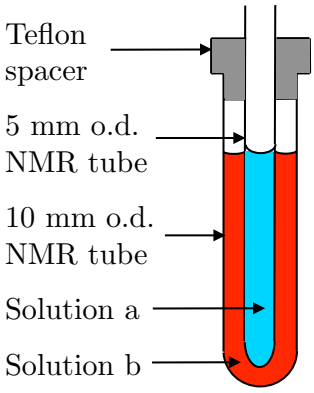


Figure 5.2: Schematic of a phantom.

Three separate phantoms were used and are summarised in Table 8: Phantom 1 consisted of water (solution a) and hexanol (solution b), Phantom 2 consisted of bromate-sulfite-CTAB product state system (solution a) and CTAB microemulsion (μE) with an aqueous phase of pure water (solution b), Phantom 3 consisted of bromate-sulfite-CTAB product state system (solution a) and reactant bromate-

sulfite-CTAB microemulsion (solution b). Once suitable imaging parameters had been determined, an aliquot of the bromate-sulfite-CTAB reactant system was transferred to a 10 mm o.d. NMR tube and placed in the bore of the magnetic resonance spectrometer.

Table 8: Summary of phantom systems.

| | **Phantom 1** | **Phantom 2** | **Phantom 3** |
|---|---|---|---|
| **Solution a** | water | μE (bromate-sulfite-CTAB product state) | μE (bromate-sulfite-CTAB product state) |
| **Solution b** | hexanol | μE (aq phase = water) | μE (bromate-sulfite-CTAB reactant state) |

### 5.2.2 Techniques

*5.2.2.1 pH measurement using a combination glass electrode*

The pH of the bromate-sulfite-CTAB system that contained Cu(II)trien was followed as a function of time to determine the effect of paramagnetic species on the induction period of the reaction. Reagent mixtures were prepared as described in section 5.2.1.3iii) by mixing μEs 3 and 4 in 50 mL conical flasks. The μE mixtures were stirred with a constant stirring rate of 200 rpm using a magnetic stirrer bar and magnetic stirrer (Stuart CD162/1). The pH was recorded in 500 ms and 1000 ms intervals using a pH combination glass electrode (Radleys) connected to a computer via a data logger (DrDaq), and using PicoLog technology. The electrode and data logger were calibrated with pH 10, 7 and 4 standard buffers (Sigma-Aldrich) prior to each set of experiments. The measurements were performed at room temperature (21.7 ± 0.5 °C).

*5.2.2.2 Magnetic resonance techniques*

All magnetic resonance (MR) experiments were performed on a Bruker DMX-300 spectrometer equipped with a 7 T vertical bore superconducting magnet operating at a proton resonance frequency of 300 MHz. A 10 mm $^1$H radiofrequency (rf) saddle coil was used for spectral investigations and a 25 mm diameter $^1$H rf birdcage coil was used for imaging experiments. The rf coil was surrounded by a triple-axis ($x$, $y$ and $z$) gradient system and a gradient strength of 45 G cm$^{-1}$ was used for all axes. The spectrometer was controlled using a Silicon Graphics workstation operating with XWIN-NMR software version 3.5 and ParaVision version 2.1.1 software. The temperature of the bore was measured and controlled using an *in situ* heater/air flow apparatus and a Eurotherm temperature controller. Microemulsion samples were equilibrated to a bore temperature of 295 ± 0.1 K and maintained at that temperature for the duration of the experiments.

*i) Relaxation time measurements*

Proton relaxation times were measured for μEs with a 2 mM Cu(II)trien aqueous pseudophase as a function of pH. A 5 mm o.d. NMR tube containing the μE sample was placed in the bore of the magnetic resonance spectrometer and equilibrated to a probe temperature of 295 ± 0.1 K before the probe was tuned. An inversion recovery sequence, $[180^\circ_x – \tau – 90^\circ_x – \text{acq}]_n$, was employed to measure the $T_1$, performing $n = 20$ experiments with logarithmically-spaced variable delay times, $\tau$, ranging from $5 \times 10^{-6}$ – 7 s, and a CPMG pulse program, $[90^\circ_x – (\tau – 180^\circ_y – \tau)_m – \text{acq}]_n$, used to measure $T_2$ performing $n = 28$ experiments, varying the number of echoes $m$ from 0 - 2400 with a delay time, $\tau$, of 1 ms. Two signal averages were acquired for each experiment with a repetition time of 7 s. The 90° and 180° pulses were 12 μs and 24 μs, respectively

at an attenuation of 6.0 dB. Both inversion recovery and CPMG pulse programs produced two-dimensional data sets with spectral data for each of the experiments within the sequence. A Fourier transform (FT) was performed on the 2D data sets and the peak amplitude used for analysis. The 2D data sets were processed and analysed using both Prospa and KaleidaGraph software. $T_1$ and $T_2$ relaxation time constants were determined by fitting the acquired data to the exponential equations 1.28 and 1.25, respectively.

*ii) Chemical shift investigations*

1D spectra were acquired during the course of the bromate-sulfite-CTAB reaction to investigate the chemical shift of water proton resonance frequencies in the system. A 5 mm o.d. NMR tube containing the bromate-sulfite-CTAB sample was placed in the bore of the magnetic resonance spectrometer and equilibrated to a probe temperature of 295 ± 0.1 K. Multiple spectra were recorded as a function of time using a 2D pulse-acquire sequence, $[90°\text{-acq}]_m$, performing $m = 64$ experiments. The 90° pulse was 11.5 μs at an attenuation of 0.0 dB. Eight signal averages were acquired per experiment with a repetition time of 10 s. A spectral width of 10 kHz was used and 8k data points were acquired. The total pulse sequence time was 88 minutes and data was acquired for a 172 minute period. Two-dimensional data sets were obtained and the data was processed and analysed using Prospa software.

*iii)Imaging experiments*

Phantoms were prepared as described in section 5.2.1.4 and placed in the bore of the magnetic resonance spectrometer. Samples were equilibrated to a probe temperature of 295 ± 0.1 K. The probe was tuned and matched and the magnet shimmed for

each phantom. The Paravision one-pulse sequence was used to acquire a 1D spectrum for each phantom, 2k complex data points were acquired for a spectral bandwidth of 10 kHz. The Paravision m_CHESS pulse sequence was employed for all imaging experiments (a schematic representing this pulse sequence is shown in Chapter 1, section 1.10.7.3). Images were acquired of vertical and horizontal slices through the sample; the slices were typically 1 or 0.5 mm thick. Contrast was optimised for each sample, whilst aiming to keep the experiment time (number of signal averages) low, by adjusting the pulse sequence parameters: repetition time $T_R$, echo time $T_E$, rf pulse length, excitation pulse bandwidth, pixel size and slice thickness.

*i. Phantom 1*

The spectrometer was set on-resonance for the water proton signal and a 1D spectrum recorded. Images were obtained for horizontal slices in the centre of the sample with a 10 × 10 mm field of view (FOV) (64 × 64 pixel matrix size). This gave a pixel size of 0.156 × 0.156 $mm^2$. Parameters were optimised and the excitation pulse bandwidth and excitation pulse offset adjusted to give different signal intensities and contrast for different resonance frequencies. The 90° pulse attenuation was 11.7 dB and the 180° pulse attenuation was 5.7 dB. An excitation pulse bandwidth of 350 Hz was found to provide optimum contrast giving a $T_E$ of 20.1 ms. A spectral width of 50 kHz and a $T_R$ of 1000 ms was used. One signal average was acquired to keep the experiment time low. The total experiment time was approximately 64 seconds.

*ii. Phantom 2*

The spectrometer was set on-resonance for the hexanol-hydroxyl proton signal of solution b and a 1D spectrum recorded. Parameters were first optimised for horizontal slices with a 10 × 10 mm FOV and a 64 × 64 pixel matrix size acquired

through the centre of the sample. Again, a spectral width of 50 kHz and $T_R$ of 1000 ms was used. Maximum signal was obtained for a 90° pulse attenuation of 11.0 dB and a 180° pulse attenuation of 5.0 dB. An excitation pulse bandwidth of 300 Hz, giving a $T_E$ of 36.8 ms, and an excitation pulse offset of 210 Hz were found to give optimum contrast. Vertical planar images were acquired with a 30 × 10 mm FOV for a 128 × 64 pixel matrix size using the same pulse lengths, repetition time and spectral bandwidth as used for horizontal image acquisition. One signal average was acquired for each image giving a total experiment time of 64 secs.

*iii. Phantom 3*

The spectrometer was set on-resonance for the coalesced hydroxyl peak of solution a and a 1D spectrum recorded. Contrast was achieved using an excitation pulse offset of both 0 and 300 Hz. Transverse and longitudinal images were obtained using an excitation pulse bandwidth of 350 Hz, a $T_E$ of 31.8 ms, a spectral width of 50 kHz, a $T_R$ of 1000 ms, a matrix size of 128 × 128 and a FOV of 10 × 10 mm and 25 × 25 mm respectively. The pulse attenuation was found to be 19.4 dB and 13.4 dB for the 90° and 180° pulse respectively. The slice thickness was 0.5 mm. The total experiment time was 128 seconds, double that of previous phantom imaging experiments due to doubling of the number of phase data points in the matrix pixel array. Once contrast had been obtained between bromate-sulfite-CTAB product and reactant solutions within the phantom the sample was removed and replaced with a 10 mm o.d. NMR tube containing freshly prepared reactant bromate-sulfite-CTAB. Care was taken when removing and replacing the probe of the spectrometer and the spectrometer was not re-tuned, -shimmed etc. Multiple images were acquired using the same parameters as had been determined to give contrast in the Phantom 3 system.

*iv. Bromate-sulfite-CTAB system*

A 10 mm o.d. NMR tube containing reactant bromate-sulfite-CTAB sample was placed in the bore of the magnetic resonance spectrometer and equilibrated to a bore temperature of 295 ± 0.1 K. The spectrometer was set on-resonance for the hexanol-OH peak and a 1D spectrum recorded. Maximum signal was obtained for a 90° pulse attenuation of 18.4 dB and a 180° pulse attenuation of 12.4 dB. An excitation pulse offset of 0 Hz was used for image acquisition with all other parameters matching those defined in 5.2.2.2iii for Phantom 3. Images were acquired for a vertical slice taken through the centre of the sample and were acquired consecutively for a period of approximately 90 minutes. Images were processed using the software package Prospa.

## 5.3 Results and discussion

The remit for the work reported in this chapter was to image the bromate-sulfite-CTAB system using MRI. Two separate approaches have been investigated; the first approach has investigated the application of a pH-dependent MR-active contrast agent whose efficacy to image the aqueous bromate-sulfite reaction has been proven (Chapter 3). The second approach has investigated the use of chemically selective excitation rf pulses that utilise the change in hydroxyl proton resonances as the acid concentration increases in the system.

### 5.3.1 Cu(II)trien as a pH-dependent MR active indicator in a CTAB w/o μE system

The paramagnetic metal ion $Cu^{2+}$ and the tetradentate ligand trien exist as a metal complex, $[Cu(trien)]^{2+}$, in aqueous solutions ≥ pH 4[22]. The dissociation of this metal-chelate for pH values less than 4 further enhances the relaxation rates of solvent proton spins and it is through this pH-dependent chelation that MR contrast was obtained for imaging of the aqueous bromate-sulfite reaction (Chapter 3). Cu(II)trien was then studied in a CTAB-hexanol-aq w/o μE system. Although changes in the $T_2$ relaxation time of water have been observed inherently in the w/o μE as a function of pH (Chapter 4), the metal-complex was studied to elucidate the potential of using such compounds in microemulsions, and to see if the behaviour provides a more favourable means with which potentially to image the system using MRI. Microemulsions were thus formed using aqueous solutions of 2 mM Cu(II)trien; macroscopically homogeneous and optically transparent mixtures were formed, confirming the formation of a microemulsion. The course of the bromate-sulfite-CTAB reaction with Cu(II)trien present was then investigated by following the pH as a function of time with a typical pH trace shown in Figure 5.3.

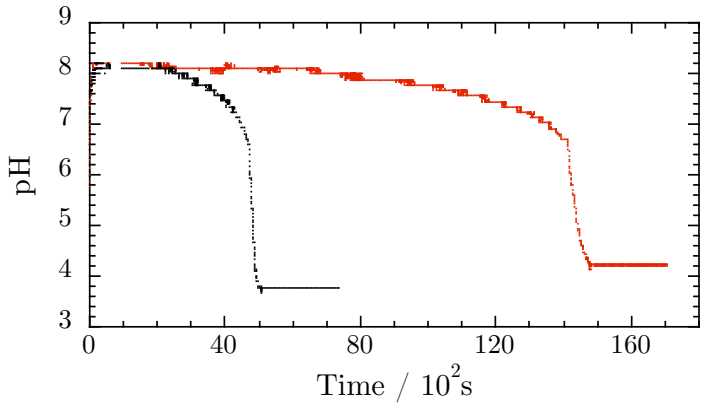


Figure 5.3: A typical pH trace of the bromate-sulfite reaction in a CTAB w/o μE with initial aqueous pseudophase reagent concentrations of bromate = 0.05 M, sulfite = 0.035 M and bisulfite = 0.015 M (black data) and, additionally, 2 mM Cu(II)trien (red data). The mixtures were stirred at a constant rate of 200 rpm.

The pH of the post-clock microemulsion system containing the paramagnetic metal ion and the chelating ligand species is greater than the post-clock pH of the microemulsion that does not contain the metal and ligand species. This was also observed for the analogous aqueous system (Chapter 3) and is associated with the basicity of the polyamine ligand. Again, the induction period is greater for the paramagnetic system, being in the range of $1.31 - 1.45 \times 10^4$ s. The induction period for the paramagnetic analogue illustrated is approximately 3.5 times greater than the standard microemulsion, compared to only approximately 1.5 times greater in the aqueous examples. Microemulsions are known to affect reaction rates[23, 24] for reasons that depend on both the composition of the microemulsion (ionic/non-ionic surfactant, $\omega_0$ etc) and the reaction type (i.e. ion forming); attempts to justify the relative greater increase in induction time for the microemulsion than that of the aqueous system were not made.

The pH of the product microemulsion (post-clock) measured using a combination glass electrode is $> 4$. This has possible implications for the use of Cu(II)trien as a contrast agent for the bromate-sulfite-CTAB system since relaxation rates for the paramagnetic solutions were increased for pH $\leq 4$ when the complex was shown to breakdown. However, the pH reported in this work is the macroscopically measured pH i.e. the pH glass electrode was unable to probe only the aqueous environment of the μE. In the previous chapter the bromate-sulfite-CTAB system was shown to have an end pH of 2.8 using calibration plots of $T_2$ versus pH *c.f.* that of 3.6 that was measured using a glass electrode (Chapter 2). Since questions regarding the definition of pH within a microemulsion remain[25], NMR investigations of the complex in a CTAB microemulsion, as a function of pH, were considered valid to

evaluate its viability as a contrast agent for MRI of the bromate-sulfite-CTAB. Also, the preparation and investigation of reaction kinetics of the paramagnetic bromate-sulfite microemulsion system demonstrated two important factors; that the presence of the metal and ligand ions does not prevent formation of a microemulsion and that the bromate-sulfite reaction is not inhibited by the MR indicator species. Subsequently, the acquisition of relaxation data as a function of pH was made for the microemulsion system.

Figure 5.4 shows the relaxation times of water protons in CTAB-hexanol-aq w/o μEs as a function of pH, the maximum error was ± 21 ms and was determined from the data acquired for 3 experimental repetitions. The relaxation times of other protons within the system were constant for the pH range investigated and differed by less than 5 % of those previously reported for the microemulsion (Chapter 4). The highest $T_1$ and $T_2$ values of water in the paramagnetic microemulsion samples are approximately equal to or less than the lowest $T_1$ and $T_2$ values of the 2 mM Cu(II)trien aqueous samples. Cu(II)trien samples gave $T_1$ values that increase from ≈ 400 to ≈ 650 ms with an increase in pH from 1 to 4, before remaining constant as the pH continues to increase; μEs that do not contain Cu(II)trien have a constant $T_1$. The analogous $T_2$ relaxation times mimic the trend previously observed for CTAB-hexanol-aq μEs for pH values from 2 and above but the minimum has shifted to pH 4 (again, this corresponded to pH at which coalescence of the hydroxyl proton resonances occurred).

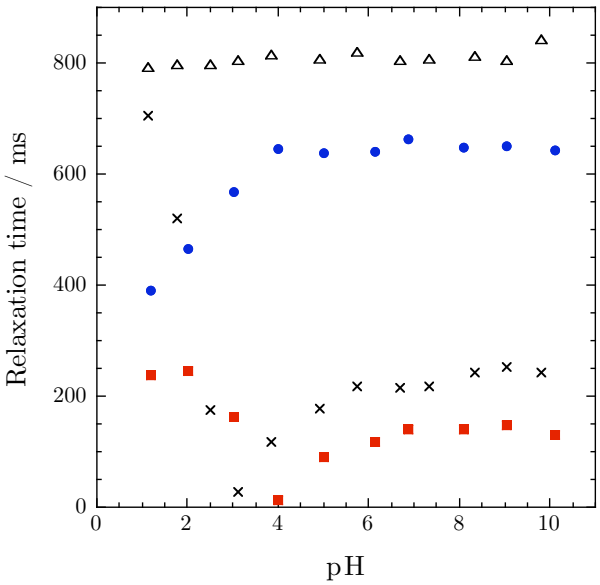


Figure 5.4: $T_1$ (●) and $T_2$ (■) relaxation times of water in CTAB-hexanol-aq w/o μEs of $\omega_0$ = 8.3 and $\phi_d$ with 2 mM Cu(II)trien aqueous pseudophase concentrations. $T_1$ (△) and $T_2$ (×) relaxation times of water in CTAB-hexanol-aq w/o μEs of $\omega_0$ = 8.3 and $\phi_d$ without the addition of paramagnetic species or chelating ligands are also shown. The reported pH is the measured pH of the aqueous stock solution prior to uptake into the microemulsion.

The decrease in $T_1$ below pH 4 reflects a change in the rotational correlation time of the water molecules. Assuming that the complexation of $Cu^{2+}$ with the tetradentate ligand has the same pH dependence in the microemulsion as in aqueous solutions then for pH values below 4 the complex has dissociated. This dissociation will result in free $Cu^{2+}$ ions for the water to coordinate to thus affecting the structure of water. However, this behaviour would also occur in aqueous solutions, yet the $T_1$ relaxation times are constant for the pH range of aqueous solutions investigated. The properties and structure of water in μEs are known to be significantly different to those of free water[26-29] with a bound layer of water existing at the charged interface whilst the remaining water forms a pool in the centre of the droplet. The free $Cu^{2+}$ ions are thus expected to reside in the water core and the structure forming

coordination of $H_2O$ may have a greater impact on the properties of the confined water. Another consideration is that the size of the reverse micelles may change with dissociation of the metal complex. Crans *et al.*[30] have discovered that a charged polar transition metal complex penetrates the hydrophobic region of the reverse micelle interface whilst Rack and co-workers[31] discovered that the chromophore probe molecule $Ru(bpy)_3^{2+}$ was able to dramatically change the water content and distribution of droplet sizes in CTAB reverse micelles. Although the relaxation times of protons in the hexanol and surfactant molecules have not been significantly decreased by the Cu(II)trien, suggesting that the complex does not reside in the hydrophobic region of the interface, further investigations regarding the location of the metal-complex and the size and structure of the droplets were not made. $T_2$ relaxation times mimic the trend that was observed in Chapter 4 for the μE system; there is a sharp decrease in $T_2$ relaxation times as the pH is increased at low pH values, followed by a steady increase in $T_2$ as the pH continues to increase. $T_2$ remains constant at pH values of 7 and above. The minimum $T_2$ relaxation time, however, is shifted to a higher pH. The $T_2$ behaviour does not mimic that of aqueous Cu(II)trien solutions as a function of pH. The overriding mechanism that affects the spin-spin relaxation process is thus proton exchange between hydroxyl groups of water and hexanol and not the effect of pH-dependent chelation of the paramagnetic metal-ion. The shift in the minimum $T_2$ to a higher pH reflects enhanced proton exchange for a lower acid concentration however, again, thorough evaluation of the reaction kinetics is difficult from the information currently available.

The pH of the bromate-sulfite-CTAB system is found to change from a pH of approximately 7 to an end pH of approximately 2.8 (Chapter 4). This corresponds to

a difference in $T_1$ relaxation times of approximately 15 % and a difference in $T_2$ relaxation times of approximately 30 % when Cu(II)trien is included in the microemulsion. If, however, the end pH were 0.3 units higher the difference in $T_2$ relaxation times would be completely removed. The data presented in this chapter therefore demonstrate that the pH dependent chelation of Cu(II)-triethylenetetramine does not enhance relaxation contrast in the bromate-sulfite-CTAB system, as was hoped from the equivalent aqueous data shown. The absence of a large and sharp change in relaxation rates with pH will restrict the contrast that can be achieved and hence the ability to readily distinguish between the reactant and more acidic product environments. The data however, do again demonstrate the change in $T_2$ associated with hydroxyl proton exchange and it is this phenomenon that is now discussed as a means to provide MR contrast in the bromate-sulfite-CTAB system.

### 5.3.2 CHESS imaging of the bromate-sulfite-CTAB system

Acid-facilitated exchange of hydroxyl protons in CTAB-hexanol-aq microemulsions was observed and discussed in the previous chapter. This process results in a coalescence and chemical shift of hydroxyl proton resonances as the acid concentration increases. Consequently, chemical shift contrast was proposed to be a viable method for obtaining magnetic resonance contrast between reactant (high pH) and product (low pH) states of the bromate-sulfite-CTAB reaction. The chemical shift of proton resonance frequencies of the bromate-sulfite-CTAB system was first investigated as a function of time. Figure 5.5a shows data acquired from a 2D pulse-acquire sequence and Figure 5.5b shows 1D representations of selected experiments during the course of the reaction. The hydroxyl resonances have been highlighted in

both figures (for full assignment of spectral peaks please refer to the previous chapter).

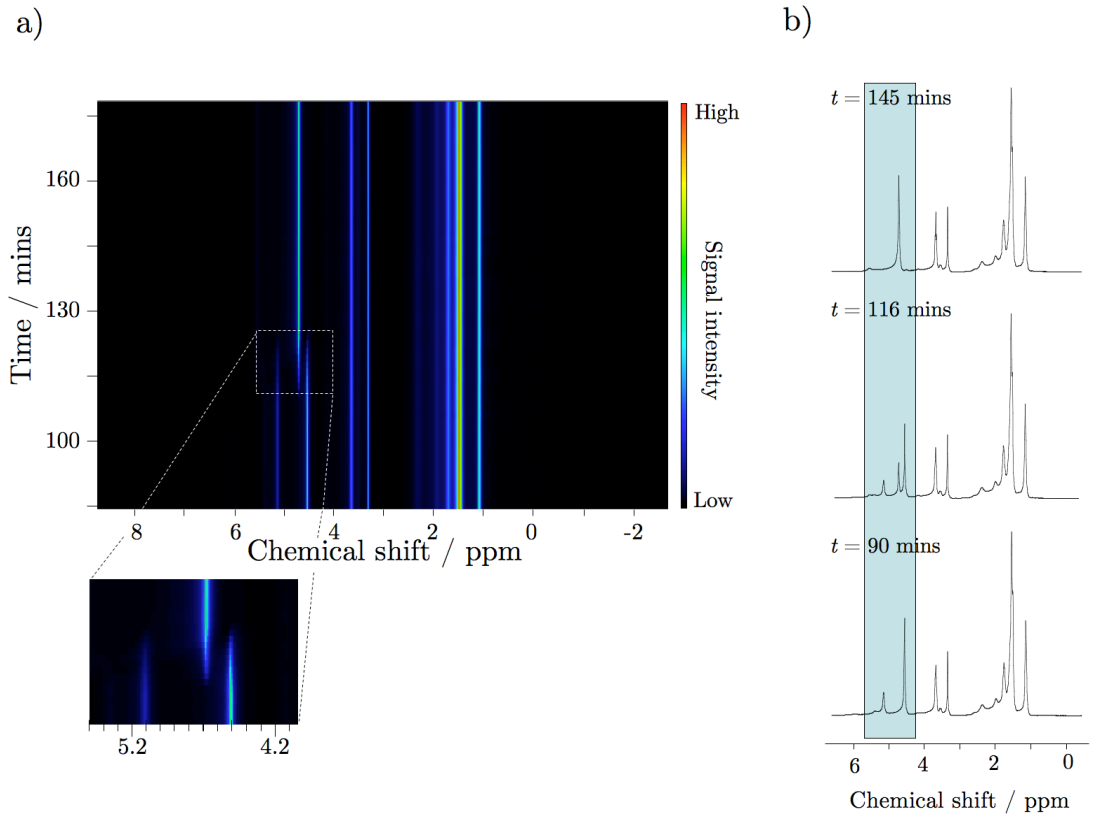


Figure 5.5: Results from a 2D pulse-acquire sequence that was used to acquire multiple spectra of the bromate-sulfite-CTAB reaction as a function of time. a) shows the 2D data plot (see Appendix 12). The point of coalescence between the hydroxyl proton frequencies is enlarged. b) shows the 1-dimensional representations of experiments acquired at selected times during the sequence. The highlighted region shows (from bottom to top) two proton resonances for hexanol and water hydroxyl protons in the reactant system, three resonances when both reactant and product regions exist within the sample and, finally, one resonance proton frequency for the product environment. The chemical shift scale is shown here in the conventional way of increasing from right to left.

The spectra acquired at $t = 90$ and $t = 145$ mins (Figure 5.5b), where $t = 0$ corresponds to the time at which the first spectrum was recorded, match those obtained for high and low pH CTAB μEs respectively (Chapter 4). These spectra, therefore, represent reactant and product μE samples. The spectrum acquired at $t =$

116 mins however, displays three hydroxyl proton peaks; two peaks have the same chemical shift as the hydroxyl peaks at $t = 90$ mins (reactant μE) whilst the third peak has the same chemical shift as the hydroxyl peak observed at $t = 145$ mins (product μE) and resides between the two other –OH peaks. The spectrum therefore shows that two chemical environments were present within the sample corresponding to product and reactant regions.

The bromate-sulfite reaction displays a sudden change in pH as the reaction 'clocks' i.e. as autocatalytic production of acid occurs. This increase in acidity facilitates exchange of protons between the hydroxyl group of hexanol and water molecules in the microemulsions system, which results in coalescence of the hydroxyl peak. The associated change in the chemical shift is 0.179 ppm for the water and -0.439 ppm for the hydroxyl-OH peak. Successful image contrast requires that the product and reactant hydroxyl resonances can be readily distinguished, with no contribution to the signal intensity from other resonance frequencies. For example, for a resonance frequency that corresponds to only that frequency of the hexanol-hydroxyl protons of the reactant state microemulsion, contributions to the signal intensity will arise from only those protons. Thus for the product environments, no proton spins of this frequency are present and thus there will be zero contribution to the signal intensity. There will be no contribution from all other hexanol, CTAB and water proton resonance frequencies. Excitation therefore requires that a narrow frequency of proton spin resonances can be selectively excited. This can prove challenging due to not all of the sample experiencing a 90° pulse and also due to inaccuracies in the range of the frequencies selected by the pulse. Another difficulty inherent with chemical shift selective imaging is that the signal contribution is reduced. For

example, the concentration of hexanol-OH protons in the CTAB μE system is 7.14 mol $dm^{-3}$ compared to a proton concentration of 112.0 mol $dm^{-3}$ for hexanol and water. For these reasons, a phantom sample of pure hexanol and water (Phantom 1) was first used to investigate chemical shift selective imaging; in this system the resonance frequencies for water and hexanol hydroxyl protons have a greater separation and there is a greater concentration of these proton spins than in the μE system.

Figure 5.6 shows MR images of Phantom 1 acquired using an m_CHESS imaging sequence for different excitation pulse bandwidths and excitation pulse offsets. The 1D spectrum of Phantom 1 is shown in Figure 5.7 and has an on-resonance water signal, the frequencies of spins that are excited for a given pulse bandwidth and pulse offset are highlighted. The spectrum shows that an excitation pulse bandwidth of 350 Hz and an excitation pulse offset of -1000 Hz should excite only the aliphatic proton spins of hexanol whilst the same excitation pulse bandwidth with a zero offset excites only those spins of water. This correlates with the MR images which show (a) high signal intensity for hexanol (outer tube) compared to that of water (inner tube), and (b) low signal intensity for hexanol compared to that of water, respectively. These images show good contrast and demonstrate how chemical shift selective imaging can be used to reduce the signal contributions from unwanted spins. It is important to note, however, that in Figure 5.6b some signal contribution remains from hexanol whilst there is no signal contribution from water in Figure 5.6a. This is due to the close proximity of hexanol spin resonances to the water spin resonance (see Figure 5.7) and highlights the difficulty in using a perfect 90° pulse that completely suppresses the signal from proton spins of neighbouring frequencies.

Figure 5.6c is included to illustrate the absence of contrast when an excitation pulse does not excite a narrow range of proton frequencies.

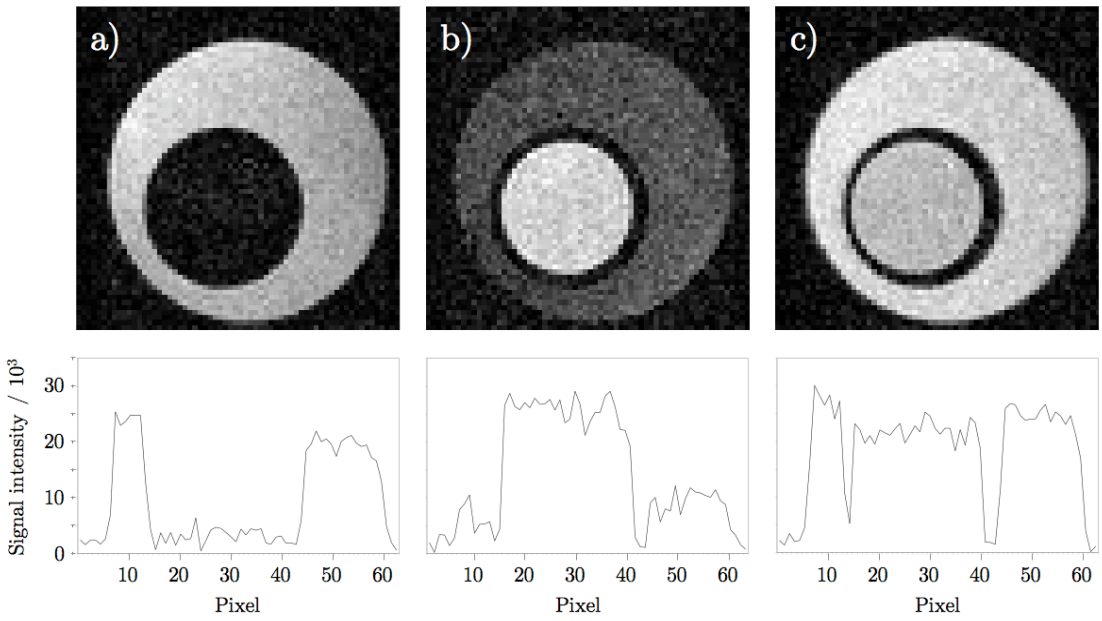


Figure 5.6: Magnetic resonance images (top), acquired using an m_CHESS imaging sequence, showing a 1 mm horizontal slice taken through the centre Phantom 1 (inner tube contains water, outer tube contains hexanol). An excitation pulse bandwidth and excitation pulse offset of a) 350 Hz and -1000 Hz, b) 350 Hz and 0 Hz and c) 1000 Hz and 0 Hz have been used respectively. An intensity profile is shown for each image (bottom). All images have a FOV of 10 × 10 mm for 64 × 64 pixels.

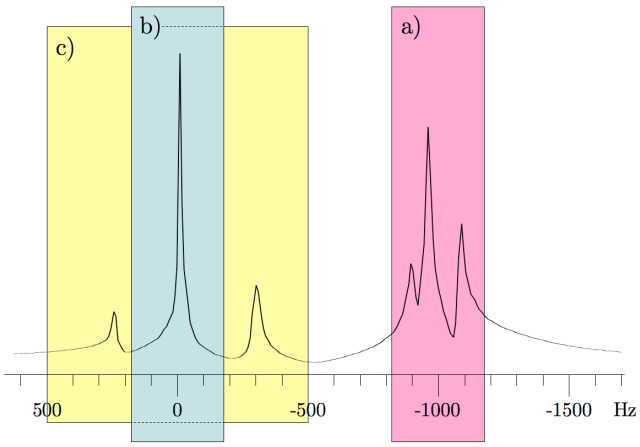


Figure 5.7: A 1D spectrum of Phantom 1 with the frequencies of excited proton spins illustrated for excitation pulse bandwidths and offsets of a) 350 Hz and -1000 Hz, b) 350 Hz and 0 Hz and c) 1000 Hz and 0 Hz respectively. The spectrometer was placed on-resonance for the water peak.

Having established that chemical shift selective excitation could be used to provide contrast between pure hexanol and water samples, a phantom (Phantom 2) consisting of bromate-sulfite-CTAB product and CTAB μE (aqueous phase of pure water) was then investigated. Bromate-sulfite-CTAB reactant samples were not used as this would introduce a time constraint, determined by procedure of the reaction, on the optimisation of experimental parameters. The spectrum for the sample is shown in Figure 5.8 and the frequency range corresponding to an excitation pulse bandwidth of 300 Hz and an excitation pulse offset of 210 Hz highlighted. The spectrum clearly shows the proximity and overlap of the water signals from the product (low pH) and the higher pH microemulsions. For this reason, and despite the spin density being lower than for that of water-OH, the hexanol-OH proton spins of solution b were chosen for excitation. MR images of the phantom acquired using these excitation pulse parameters and, again, using an m_CHESS pulse sequence, are shown in Figure 5.9 for a horizontal and vertical slice. The images were acquired using a 90° pulse attenuation of 11.0 dB and a 180° pulse attenuation of 5.0 dB.

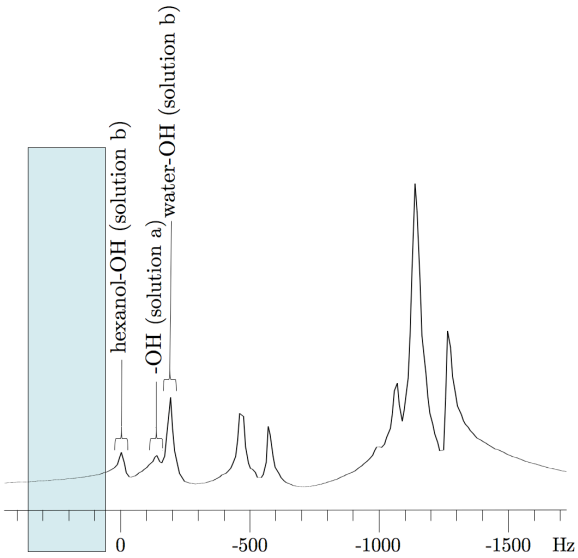


Figure 5.8: A 1D spectrum of Phantom 2 with an on-resonance hexanol-OH proton peak. The box represents the frequency range for an excitation pulse bandwidth of 300 Hz and excitation pulse offset of 210 Hz.

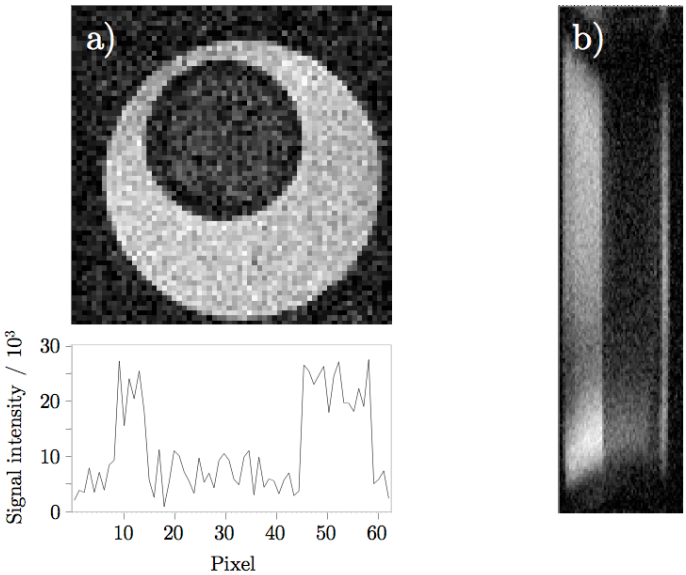


Figure 5.9: Magnetic resonance images showing a 1 mm (a) horizontal and (b) vertical slice of Phantom 2 (inner tube contains product state μE, outer tube contains μE with an aqueous phase of water). Images were acquired using an m_CHESS imaging sequence using an excitation pulse offset of 210 Hz and an excitation pulse bandwidth of 300 Hz. The images have a) a FOV of 10 × 10 mm for 64 × 64 pixels and b) a FOV of 30 × 10 mm for 128 × 64 pixels. An intensity profile is also shown for a).

Contrast was achieved by adjusting experimental parameters such as the excitation pulse bandwidth, offset and pulse power. From Figure 5.8, it seems apparent that the excitation pulse bandwidth and excitation pulse offset indicated would excite a frequency range that is absent of proton spins, thus producing zero signal. However, the MR images clearly show high signal intensity for solution b compared to low signal intensity for solution a (the dark regions at the top and bottom of Figure 5.9b are artefacts arising from magnetic field and transmit rf pulse inhomogeneities). This excitation of proton spins outside the expected frequency range demonstrates imperfections in the 90°, chemically selective pulse and emphasises the need to use phantom samples for optimisation of experimental parameters. The MR images obtained for Phantom 2 show good contrast and demonstrate that sufficient signal intensity can be obtained from the chemical selective excitation of only hexanol-OH proton spins in a CTAB μE system. Following this discovery, a phantom system containing reactant and product bromate-sulfite-CTAB (Phantom 3) was investigated.

MR images of Phantom 3 are shown in Figure 5.10 for a horizontal and vertical slice. A narrower slice thickness (0.5 mm) and increased matrix size (128 × 128 pixels for a FOV of 10 × 10 mm and 25 × 25 mm) were investigated to see if contrast could be obtained for images with improved spatial resolution (resolution = FOV / matrix size). The image and intensity profile shown in Figure 5.10a demonstrate increased noise when compared to those in Figure 5.9a. This arises due to a decrease in the pixel size and a subsequent lower spin density for a given imaging voxel. The signal-to-noise ratio can be improved by increasing the number of scans (a second repetition doubles the signal whereas random noise is increased by only a factor of

√2); however, this would increase the experiment time. A compromise, therefore, has to be made between temporal and spatial resolution. Although a reduced signal-to-noise ratio is observed, contrast between the product and reactant μE environments can be seen in Figure 5.10a and thus imaging investigations of this system can be performed with a pixel size of 0.078 mm pixel$^{-1}$. Further images were, however, acquired with a pixel size of 0.195 mm pixel$^{-1}$ (i.e. Figure 5.10b). The total experiment time was 128 seconds.

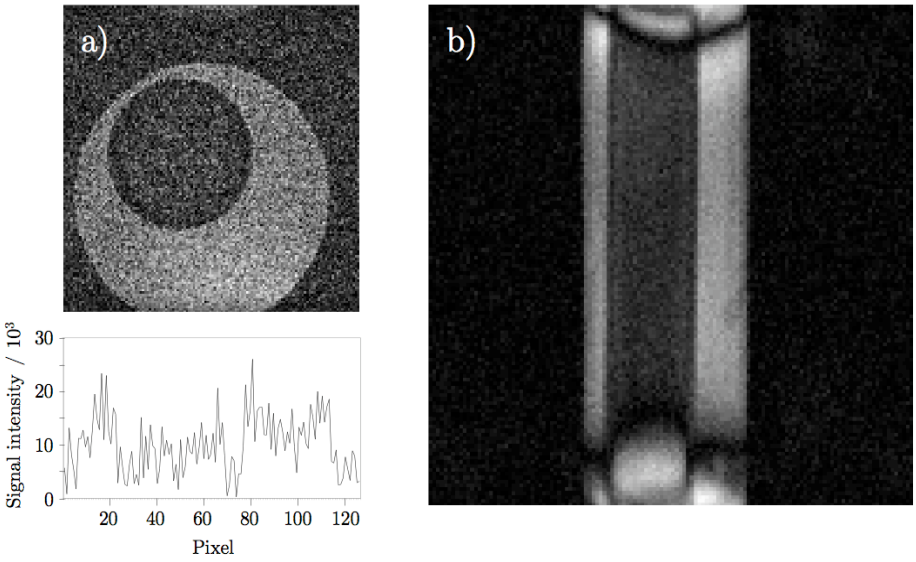


Figure 5.10: Magnetic resonance images showing a 0.5 mm (a) horizontal and (b) vertical slice of Phantom 2 (inner tube contains product state μE, outer tube contains μE with an aqueous phase of water). Images were acquired using an m_CHESS imaging sequence using an excitation pulse bandwidth of 350 Hz. The images have a) a FOV of 10 × 10 mm and b) a FOV of 25 × 25 mm for a 128 × 128 matrix array. An intensity profile is also shown for a).

Finally, freshly prepared bromate-sulfite-CTAB samples were investigated using the parameters determined to give contrast in Phantom 3. Figure 5.11 shows MR images acquired using the m_CHESS pulse sequence and a chemically selective excitation pulse bandwidth of 350 Hz; each image acquisition took 128 seconds and images were

acquired successively. The images show darker outer regions with a central dark structure propagating down the centre of the image before the darker outer regions spread inwards. From the contrast observed for images of Phantom 3 it is known that this darker region corresponds to a region of low pH where the coalesced hexanol-OH signal does not contribute to signal intensity. Thus Figure 5.11 shows the first MR images of a propagating acidity front in a microemulsion system. Initially, the propagating acidity front displays a spiral-like motion before appearing to remain in one plane and propagating downwards at an approximate speed of 0.065 mm $min^{-1}$. The presence of a downward propagating front was expected from observations reported in Chapter 2 where the conversion of reactants to products was seen to occur more readily at the μE/air interface (top of the sample), similarly, products are then observed at the μE/glass interface.

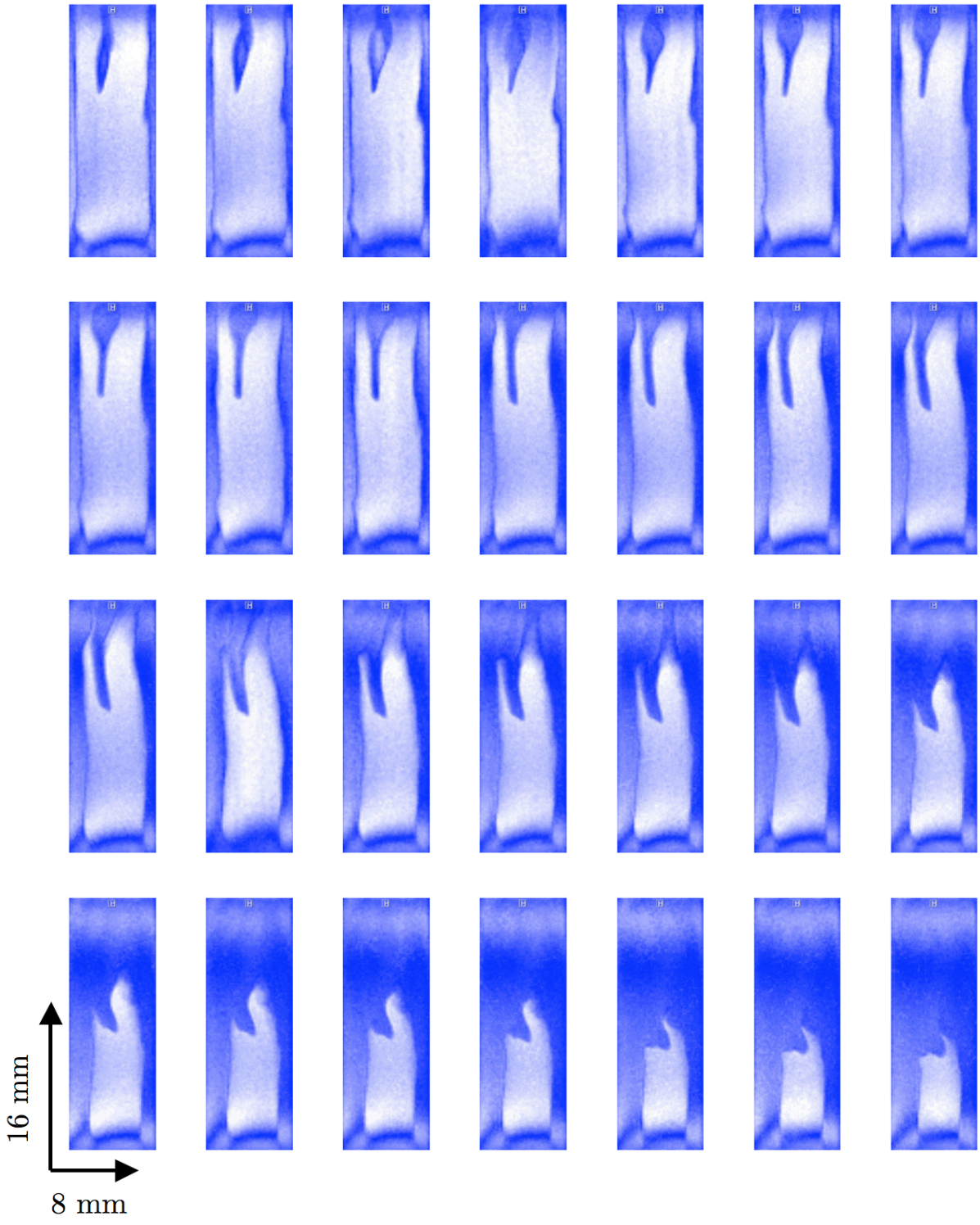


Figure 5.11: MR images showing a propagating acidity front of the bromate-sulfite reaction performed in a CTAB-hexanol-aq microemulsion system with $\omega_0 = 8.3$ and $\phi_d = 0.4$. FOV shown is 8.3 x 25 mm. Images were acquired consecutively and had an acquisition time of 128 seconds.

## 5.4 Conclusions and further work

The suitability of Cu(II)trien as an MR active pH indicator for imaging of the bromate-sulfite-CTAB reaction was investigated. The induction period of the reaction increased with the presence of Cu(II)trien and the final pH was higher than that of the non-paramagnetic analogue; however, the reaction still displayed typical clock behaviour. The relaxation times of CTAB μEs containing 2 mM Cu(II)trien pseudoaqueous phases were investigated as a function of pH. The behaviour of the transition metal ion and tetradentate ligand in the microemulsion is not fully understood and cannot be determined easily from the data obtained; the relaxation times recorded for the microemulsion system do not mimic the analogous aqueous system. The hydroxyl proton exchange between water and alcohol was found to be the overriding mechanism through which spin-spin relaxation occurs and not through the influence of the paramagnetic metal ion on the proton spins. The absence of a large and sharp change in relaxation rates with pH will restrict the contrast that can be achieved and hence the ability to readily distinguish between the reactant and more acidic product environments of the reaction. Thus, the work in this chapter demonstrates that Cu(II)trien is unsuitable as a pH-active MR contrast agent for imaging of the bromate-sulfite reaction in a CTAB w/o μE. Subsequently, the observed proton exchange phenomenon was exploited to provide MR contrast in the bromate-sulfite-CTAB reaction.

The work in this chapter shows that during the course of the bromate-sulfite-CTAB reaction the hydroxyl proton resonances of both water and hexanol coalesce. This is a consequence of facilitated proton exchange that occurs as the proton environments become more acidic, following conversion of reactants to products. An MR imaging sequence that uses a chemically selective excitation pulse was then investigated to

determine its suitability in exploiting this exchange phenomenon. Experimental parameters were optimised to give contrast between samples of hexanol and water, high and low pH CTAB μEs and ultimately, reactant and product bromate-sulfite-CTAB environments. This was achieved by the selective excitation of proton spin frequencies corresponding to only those found in either the product or reactant environment. Consequently, MR images of a propagating acidity front of the bromate-sulfite reaction performed in a water-in-oil microemulsion were obtained. The images that were acquired represented a 0.5 mm slice taken through the centre of the sample and had a resolution of 0.195 mm pixel$^{-1}$.

The results presented in this chapter demonstrate the first MR images of a propagating acidity front in heterogeneous media. Having demonstrated that MRI is a suitable technique for the visualisation of these reaction fronts, the opportunity now exists to, not only further develop and optimise imaging sequences, but also to further evaluate the behaviour of these fronts, given this new insight into their behaviour. An obvious enhancement would be the acquisition of multiple slices, since the experiments performed thus far obtained single-slice data, whilst the conflict between spatial and temporal resolution offers an ever-present challenge to those who utilise MRI techniques. The existence of acid-facilitated proton exchange within the microemulsion allows for the effect microstructure has on propagating acidity fronts to be investigated by adjusting the parameters that define a microemulsion's structure, such as droplet fraction and droplet size. The ability to probe and visualise these 3D systems and structures creates pathways to improved understanding of these systems and the possibility of being able to model the behaviour that results from the coupling of non-linear reaction dynamics with heterogeneous media.

## 5.5 References


[1] I. R. Epstein, J. A. Pojman, *An introduction to nonlinear chemical dynamics : oscillations, waves, patterns, and chaos*, Oxford University Press, New York, **1998**.

[2] I. R. Epstein, V. K. Vanag, *Chaos* **2005**, *15*.

[3] R. E. McIlwaine, H. Fenton, S. K. Scott, A. F. Taylor, *Journal of Physical Chemistry C* **2008**, *112*, 2499.

[4] A. Keresztessy, I. P. Nagy, G. Bazsa, J. A. Pojman, *Journal Of Physical Chemistry* **1995**, *99*, 5379.

[5] V. Volpert, S. Petrovskii, *Physics of Life Reviews* **2009**, *6*, 267.

[6] L. F. Jaffe, *Proceedings of the National Academy of Sciences of the United States of America* **1991**, *88*, 9883.

[7] G. I. Sivashinsky, *Annual Review of Fluid Mechanics* **1983**, *15*, 179.

[8] A. Tzalmona, R. L. Armstrong, M. Menzinger, A. Cross, C. Lemaire, *Chemical Physics Letters* **1990**, *174*, 199.

[9] R. Evans, C. R. Timmel, P. J. Hore, M. M. Britton, *Chemical Physics Letters* **2004**, *397*, 67.

[10] M. M. Britton, *Journal Of Physical Chemistry A* **2006**, *110*, 5075.

[11] V. V. Zhivonitko, I. V. Koptyug, R. Z. Sagdeev, *Journal Of Physical Chemistry A* **2007**, *111*, 4122.

[12] B. W. Thompson, J. Novak, M. C. T. Wilson, M. M. Britton, A. F. Taylor, *Physical Review E* **2010**, *81*.

[13] M. C. Rogers, M. D. Mantle, A. J. Sederman, S. W. Morris, *Physical Review E* **2008**, *77*.

[14] M. M. Britton, *Chemical Society Reviews* **2010**, *39*, 4036.

[15] R. B. Lauffer, *Chemical Reviews* **1987**, *87*, 901.

[16] A. E. Merbach, É. Tóth, *The chemistry of contrast agents in medical magnetic resonance imaging*, Wiley, Chichester ; New York, **2001**.

[17] E. Toth, L. Helm, A. E. Merbach, in *Contrast Agents I, Vol. 221*, **2002**, p. 61.

[18] T. A. Bley, O. Wieben, C. J. Francois, J. H. Brittain, S. B. Reeder, *Journal of Magnetic Resonance Imaging* **2010**, *31*, 4.

[19] A. Haase, J. Frahm, W. Hanicke, D. Matthaei, *Physics in Medicine and Biology* **1985**, *30*, 341.

[20] A. Haase, J. Frahm, *Journal of Magnetic Resonance* **1985**, *64*, 94.

[21] P. T. Callaghan, *Principles of nuclear magnetic resonance microscopy*, Clarendon Press; Oxford University Press, Oxford [England] New York, **1991**.

[22] J. M. Baker, J. E. Teggins, J. W. Hoffman, *JAWRA Journal of the American Water Resources Association* **1971**, *7*, 1246.

[23] J. H. Fendler, *Accounts of Chemical Research* **1976**, *9*, 153.

[24] K. Bhattacharyya, *Accounts of Chemical Research* **2003**, *36*, 95.

[25] R. E. Smith, P. L. Luisi, *Helvetica Chimica Acta* **1980**, *63*, 2302.

[26] K. Bhattacharyya, B. Bagchi, *Journal of Physical Chemistry A* **2000**, *104*, 10603.

[27] N. E. Levinger, *Science* **2002**, *298*, 1722.

[28] M. Hasegawa, T. Sugimura, Y. Shindo, A. Kitahara, *Colloids and Surfaces a-Physicochemical and Engineering Aspects* **1996**, *109*, 305.

[29] K. M. Manoj, R. Jayakumar, S. K. Rakshit, *Langmuir* **1996**, *12*, 4068.

[30] D. C. Crans, C. D. Rithner, B. Baruah, B. L. Gourley, N. E. Levinger, *Journal of the American Chemical Society* **2006**, *128*, 4437.

[31] J. J. Rack, T. M. McCleskey, E. R. Birnbaum, *Journal of Physical Chemistry B* **2002**, *106*, 632.

# 6 Concluding remarks

In this research, magnetic resonance (MR) methods, which probe pH in aqueous and reverse micelles in CTAB and Triton-X microemulsions, have been investigated. These methods have been used to image propagating acidity fronts in the bromate-sulfite reaction both in aqueous solution and a CTAB microemulsion.

The bromate-sulfite reaction was investigated in a CTAB water-in-oil microemulsion system and propagating reaction fronts were observed in tubes of inner diameter 2.3 – 8.6 mm. Fronts were observed using a pH indicator and recorded using a CCD camera, and a range of hydrodynamic instabilities were observed. These measurements however, highlighted the limitations of this method for visualising this system, whereby measurements are integrated across the width of the tube and hence are unable to distinguish between the regions at the centre of the tube from regions at the edge. Magnetic resonance imaging (MRI) of propagating fronts of the bromate-sulfite reaction was employed to eliminate this problem.

Initial investigations focussed on the bromate-sulfite reaction in aqueous solution and the development of a suitable pH-dependent contrast agent for imaging of pH fronts in this reaction was investigated. To this end, Mn(II) and Cu(II) species and the tetradentate chelating ligand trien were investigated. $[Mn(trien)]^{2+}$ was unstable in solution and was thus unsuitable as a contrast agent in the reaction, however, the complex $[Cu(trien)]^{2+}$ existed for pH values greater than pH 4 and dissociated for pH values below 4. This pH-dependent chelation of the metal ion provided the necessary

relaxation time contrast to allow successful MR imaging of propagating acidity fronts of the reaction.

Cu(II)trien was also investigated as a suitable pH-dependent paramagnetic contrast agent for the bromate-sulfite-CTAB system. The presence of the metal ion and chelating ligand did not prevent the formation of a stable water-in-oil microemulsion. The reaction still behaved as a classic clock in the presence of Cu(II)trien by displaying a sudden drop in pH as autocatalytic production of $H^+$ occurred but the kinetics of the reaction were affected; the induction period of the clock was greater when Cu(II)trien was present. The formation of a stable water-in-oil microemulsion and the display of clock behaviour in the presence of Cu(II)trien is important as it may allow for Cu(II)trien to be used to image the reaction in different microemulsion media. However, it was found that a pH contrast agent was not necessary in the CTAB system as the pH could be probed through an acid-catalysed proton exchange mechanism, which dominated the relaxation time of protons in the reverse micelle core. Cu(II)trien may be a suitable pH-dependent contrast agent in systems where proton exchange mechanisms between alcohol and water do not dominate.

Magnetic resonance methods were investigated which enabled the pH to be measure in a microemulsion. Proton relaxation times were measured as a function of pH and were found to change with pH for values below pH 6. This observation was due to acid-facilitated proton exchange mechanisms between water molecules and the hydroxyl groups in hexanol in the microemulsion. This exchange process resulted in a coalescing of the hydroxyl peaks in the NMR spectrum, at approximately pH 3.4. This proton-exchange phenomenon was investigated as a function of the water-to-

surfactant ratio and ionic strength and was found to be sensitive to these parameters. However, by calibrating the relaxation times as a function of pH, for a given water-to-surfactant ratio and ionic strength, it was possible to monitor the pH change of the bromate-sulfite-CTAB system without the need to introduce probe molecules.

In an investigation of the bromate-sulfite-CTAB system it was found that the final pH was higher than in the aqueous analogue. This may be due to a number of reasons such as the effect on the microemulsion structure itself of acid and heat production during the reaction. It is also possible that there may be an actual difference in the pH between the aqueous and microemulsion systems: This will need further investigation. Regardless of these differences, this work has, for the first time, allowed direct measurement of pH in this system.

The coalescence of hydroxyl peaks, due to the proton-exchange mechanism, was then exploited to image the bromate-sulfite-CTAB system. A chemical shift selective pulse sequence was used that selectively excites only a narrow range of frequencies, which, in these experiments were those of the hexanol-hydroxyl protons. Thus, the first magnetic resonance images of a propagating acidity front in heterogeneous media have been acquired. An image was acquired of a 0.5 mm slice through the centre of the sample and a downward propagating finger observed that displayed an initial spiral motion before appearing to remain in the plane in which the slice was acquired. Having established a suitable means to obtain MR contrast it is now possible to image these systems more thoroughly than has previously been achieved using optical imaging. It is anticipated that this will allow for a greater

understanding of the behaviour of reaction fronts within these systems, and the effect of changing the microenvironment in which the reaction is performed can be investigated.

# 7 Appendices

## 7.1 Appendix 1

Two parameters define microemulsion structure; the water to surfactant ratio $\omega_0$ and the droplet fraction $\phi_d$. The mole volume of CTAB is 1.15 mL per g of dissolved solid such that, for CTAB-hexanol-aqueous microemulsions with a composition of 6.1 g CTAB, 14 mL hexanol and 2.5 mL aqueous, $\omega_0$ and $\phi_d$ are typically calculated as:

$$\text{Moles CTAB} = \frac{6.1\ \text{g}}{364.45\ \text{g mol}^{-1}} = 0.0167\ \text{mol}$$

$$\text{Moles } H_2O = \frac{2.5\ \text{g}}{18\ \text{g mol}^{-1}} = 0.139\ \text{mol}$$

$$\text{Total volume} = 6.1\ \text{g} \times 1.15\ \text{mL g}^{-1} + 14\ \text{mL} + 2.5\ \text{mL} = 23.515\ \text{mL}$$

$$\text{Concentration of CTAB} = \frac{0.0167\ \text{mol}}{23.515 \div 1000\ \text{dm}} = 0.71\ \text{mol dm}^{-3}$$

$$\text{Concentration of } H_2O = \frac{0.139\ \text{mol}}{23.515 \div 1000\ \text{dm}} = 5.91\ \text{mol dm}^{-3}$$

$$\omega_0 = \frac{[H_2O]}{[\text{CTAB}]} = \frac{5.91\ \text{mol dm}^{-3}}{0.71\ \text{mol dm}^{-3}} = 8.3$$

$$\phi_d = \frac{\text{Vol}_{\text{CTAB}} + \text{Vol}_{H_2O}}{\text{Total volume}} = \frac{(6.1 \times 1.15) + 2.5}{23.515} = 0.40$$

## 7.2 Appendix 2

The coupling of pattern forming reactions with flow is able to extend the range of patterns that can be achieved and observed. The aqueous bromate-sulfite reaction was incorporated in a Couette-cell (Figure 7.1): A Couette-cell consists of two concentric cylinders; the inner cylinder is rotated. Above a critical rotation rate, steady Taylor vortices can be produced. Propagating waves of the BZ reaction have been studied in this system[1]. Figure 7.1 demonstrates the first example of a propagating reaction front through a series of three-dimensional vortices.

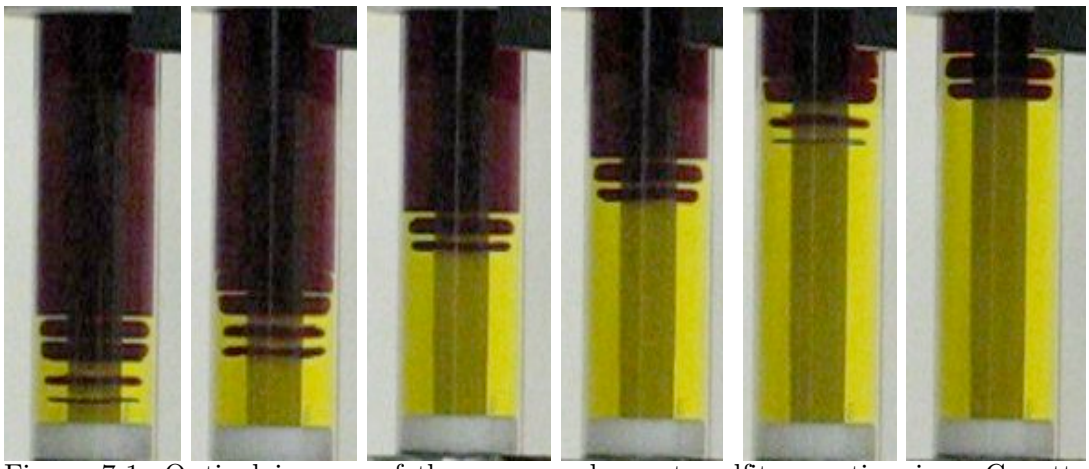

Figure 7.1: Optical images of the aqueous bromate-sulfite reaction in a Couette-cell. The Couette cell consists of two concentric cylindrical tubes. The outer cylinder has an inner diameter of 11 mm, the inner cylinder has an outer diameter of 5 mm, thus giving an annulus (distance between the cylinders) of 3 mm. The length of the sample is 50 mm. The colour pH indicator bromocresol purple was used to give contrast between the reactant (purple) and more acidic product (yellow) environments. The images shown cover a time scale of 1 minute 50 seconds and were acquired for an inner rotation rate of 3.1 Hz.

[1] B. W. Thompson, J. Novak, M. C. T. Wilson, M. M. Britton, A. F. Taylor, *Physical Review E* **2010**, *81*.

## 7.3 Appendix 3

The parameters that define the composition of a four-component system in a water-in-oil microemulsion phase are the water-to-surfactant ratio $\omega_0$, the cosurfactant-to-surfactant ratio $P_0$ and the oil-to-surfactant ratio $n_0/n_s$. Water-in-oil microemulsions were thus prepared with $\omega_0 = 8.2$, $P_0 = 12$ and $n_0/n_s = 7.6$.

$$\text{Moles CTAB} = \frac{3.65\ \text{g}}{364.45\ \text{g mol}^{-1}} = 0.0100\ \text{mol}$$

$$\text{Moles } H_2O = \frac{1.5\ \text{g}}{18\ \text{g mol}^{-1}} = 0.083\ \text{mol}$$

$$\text{Moles pentanol} = \frac{13\ \text{cm}^3 \times 0.8144\ \text{g cm}^{-3}}{88.15\ \text{g mol}^{-1}} = 0.120\ \text{mol}$$

$$\text{Moles hexane} = \frac{10\ \text{cm}^3 \times 0.6548\ \text{g cm}^{-3}}{86.18\ \text{g mol}^{-1}} = 0.076\ \text{mol}$$

$$\omega_0 = \frac{[H_2O]}{[\text{CTAB}]} = \frac{0.083\ \text{mol}}{0.01\ \text{mol}} = 8.3$$

$$P_0 = = \frac{[\text{pentanol}]}{[\text{CTAB}]} = \frac{0.120\ \text{mol}}{0.01\ \text{mol}} = 12$$

$$\frac{n_o}{n_s} = \frac{[\text{hexane}]}{[\text{CTAB}]} = \frac{0.076\ \text{mol}}{0.01\ \text{mol}} = 7.6$$

## 7.4 Appendix 4

Mixtures with a chemical composition of;

0.670 mL aqueous phase

2.65 mL Triton X-100 (TX)

5.00 mL cyclohexane

2.70 mL 1-hexanol

were used to produce microemulsions with $\omega_0 = 8.2$ and $\phi_d = 0.3$. These parameters were determined through the following calculations, using the density of Triton X-100 as 1.07 g $cm^{-3}$ and the relative molecular mass as 624.8 (calculated assuming n = 9.5 in the formula $(C_2H_4O)_nC_{14}H_{22}O$:

$$\text{Number of moles } H_2O = \frac{0.670}{18.0148} = 3.719 \times 10^{-2}$$

$$\text{Number of moles TX} = \frac{2.65 \times 1.07}{624.8} = 4.538 \times 10^{-3}$$

$$\omega_0 = \frac{[H_2O]}{[TX]} = \frac{3.719 \times 10^{-2}}{4.538 \times 10^{-3}} = 8.2$$

Total volume = 0.670 + 2.65 + 5.00 + 2.70 = 11.02 mL

$$\phi_d = \frac{\text{Vol}_{TX} + \text{Vol}_{H_2O}}{\text{Total volume}} = \frac{2.65 + 0.670}{11.02} = 0.30$$

## 7.5 Appendix 5

Microemulsions of AOT-octane-aq were prepared; firstly, a 1.5 M AOT in octane solution was prepared. The volume of this solution needed to give a specific water-to-surfactant ratio, $\omega_0$, was then determined by fixing the volume of water used, thus;

$$\omega_0 = \frac{[H_2O]}{[AOT]} = \frac{\#\text{ moles } H_2O}{\#\text{ moles AOT}} \text{ since the total volume is the same.}$$

$$8.2 = \frac{55.556 \times 2\,\text{mL}}{1.5 \times \text{vol}_{\text{AOT}}} \;\therefore\; \text{vol}_{\text{AOT}} = \frac{55.556 \times 2}{1.5 \times 8.2} = 9.0\,\text{mL}$$

Thus, a composition of 9 mL AOT solution (1.5 M in octane) and 2 mL aqueous solution gives a microemulsion with $\omega_0 = 8.2$. To determine the droplet fraction, $\phi_d$, the following equations are used:

$$\phi_d = \frac{\text{Vol}_{\text{AOT}} + \text{Vol}_{H_2O}}{\text{Total volume}}$$

$$\phi_w = \frac{\text{Vol}_{H_2O}}{\text{Total volume}}$$

$$\phi_d \approx \phi_w \left(1 + \frac{21.6}{\omega_0}\right)$$

Thus,

$$\phi_w = \frac{2}{9+2} = 0.182 \text{ and } \phi_d = 0.182\left(1 + \frac{21.6}{8.2}\right) = 0.66$$

6 mL of this solution was then diluted with 4 mL octane to give an AOT-octane-aq microemulsion with $\phi_d = 0.4$.

## 7.6 Appendix 6

For aqueous phase pH values greater than 3.1, the spin-spin relaxation times of water in CTAB-hexanol-aq microemulsions were dependent on the delay time $\boldsymbol{\tau}$ that was used (Figure 7.2). The effect of translational motion on the measured $T_2$ can account for this; diffusion of the nuclei to a region experiencing a slightly different magnetic field during the course of the pulse sequence will result in incomplete refocusing of the spins following the 180° pulse. Hence an apparent enhancement of the spin-spin relaxation rate $(1/T_2)$ will occur. The nuclei will diffuse more and experience more varying local magnetic fields in a longer given time, i.e. for a longer $\boldsymbol{\tau}$ . The absence of $\boldsymbol{\tau}$ effects on the measured $T_2$ of the system below a pH of 3.1 is due to the fast-exchange mechanisms of water protons in the system at this pH; protons here are in fast exchange on the NMR time-scale between the water molecules and the hexanol-OH moieties and thus an average signal is seen, further enhancement of the relaxation process due to diffusion therefore, does not occur.

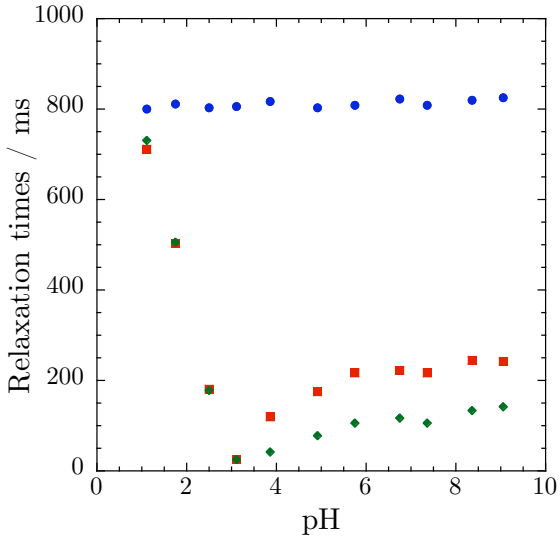


Figure 7.2: Relaxation times of water in a CTAB-hexanol-aq microemulsion with $\omega_0 = 8.3$ and $\phi_d = 0.4$ as a function of pH. $T_1$ relaxation times are shown with a blue circle, $T_2$ relaxation times determined using $\boldsymbol{\tau} = 1$ ms are shown as red squares and $T_2$ relaxation times determined using $\boldsymbol{\tau} = 4$ ms shown as green diamonds.

## 7.7 Appendix 7

Initial relaxation time measurements of CTAB-hexanol-aq microemulsions were performed on microemulsions that were prepared using 95 % CTAB (Aldrich, product code 855820). This product is now unavailable and CTAB (≥ 98 %) was used for subsequent experiments. Figure 7.3 shows the relaxation times of water in a CTAB (95 %)-hexanol-aq microemulsion with $\omega_0 = 8.3$ and $\phi_d = 0.4$ as a function of aqueous phase pH. The $T_1$ relaxation time increases from approximately 350 ms to 790 ms as the pH increases from 1 to 3, before remaining constant at approximately 790 ms as the pH continues to increase. The $T_2$ relaxation time displays an increase from approximately 230 ms to 270 ms as the pH increases from 1 to 2, then decreases to a minimum of 11 ms at pH 3.1 before gradually increasing with pH to a maximum of 98 ms at pH 9. For CTAB (≥ 98 %) microemulsions, the $T_1$ relaxation times were constant for the entire pH range investigated; the $T_2$ relaxation time decreased from 700 ms to 11 ms as the pH increased from 1 to 3 before gradually increasing as the pH continued to increase. It is presumed that impurities present in the 95 % CTAB affected the relaxation rates of water in the microemulsion at low pH values.

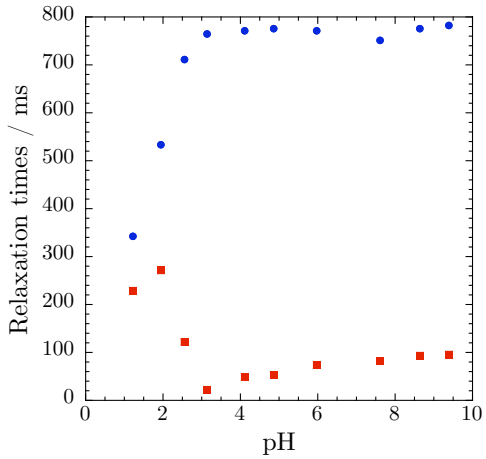


Figure 7.3: $T_1$ (●) and $T_2$ (■) relaxation times of water in CTAB-hexanol-aq microemulsions ($\omega_0 = 8.3$ and $\phi_d = 0.4$) for a pH range of 1.2 – 9.3. The pH here is the measured pH of the aqueous stock solution prior to uptake in the microemulsion.

## 7.8 Appendix 8

The relaxation times of water in CTAB-hexanol-aq microemulsions ($\omega_0$ = 8.3 and $\phi_d$ = 0.4) as a function of pH and ionic strength are shown in Figure 7.4. The $T_1$ relaxation times are constant for all experiments.

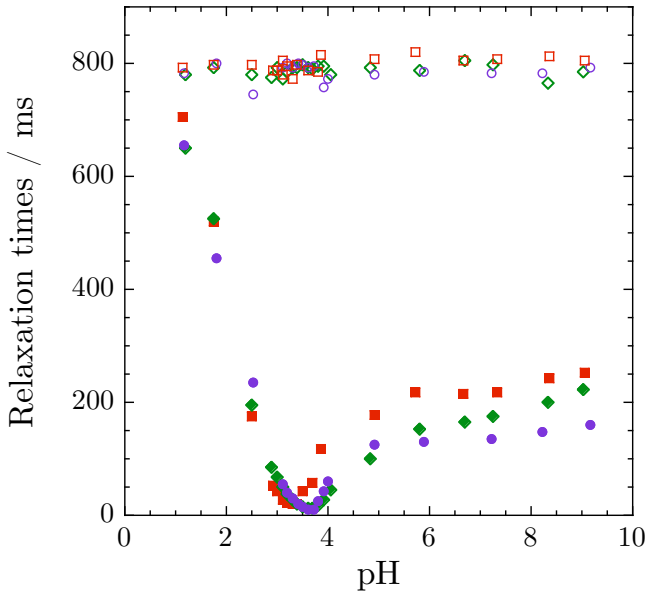


Figure 7.4: $T_1$ (hollow shapes) and $T_2$ (filled shapes) relaxation times of water in CTAB-hexanol-aq microemulsions ($\omega_0$ = 8.3 and $\phi_d$ = 0.4) for aqueous ionic strengths of 0.15 M (red square), 0.30 M (green diamond) and 0.45 M (purple circle). The pH is the measured pH of the aqueous stock phase prior to uptake in the microemulsion.

## 7.9 Appendix 9

The chemicals shift of hydroxyl peaks was found to move downfield as $\omega_0$ increased (Figure 7.5) and the change in chemical shift of the water peak following coalescence was smaller for larger $\omega_0$ whilst the chemical shift difference between the hexanol-hydroxyl and coalesced resonances increased with $\omega_0$ (Table 9).

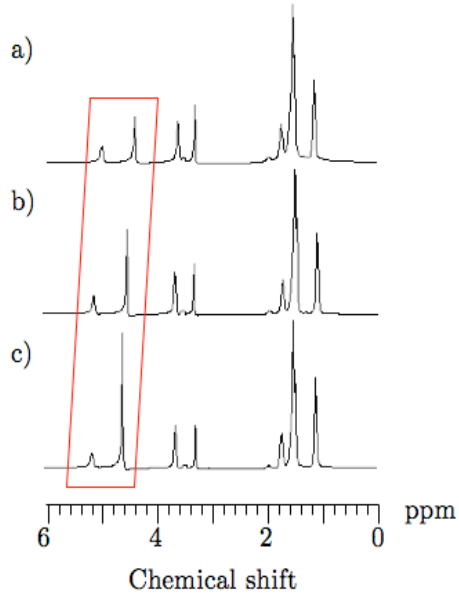


Figure 7.5: $^1$H NMR spectra for CTAB-hexanol-aq microemulsions with $\phi_d$ = 0.4 and $\omega_0$ = a) 5.2, b) 8.3 and c) 16.4. The pH of the aqueous phase is 7.3 for all. The hydroxyl peaks shift downfield as $\omega_0$ increases.

Table 9: The difference in the chemical shift of the hydroxyl resonance following coalescence (chemical shift at pH 7 – chemical shift at pH 2).

| | **Change in the chemical shift / ppm** | |
|---|---|---|
| $\omega_0$ | **Hydroxyl-OH** | **Water-OH** |
| 5.2 | 0.40 | 0.24 |
| 8.3 | 0.44 | 0.18 |
| 16.4 | 0.46 | 0.11 |

## 7.10 Appendix 10

Figure 7.6 represents the coalescence of hydroxyl peaks in a quaternary CTAB-hexane-pentanol-aq microemulsion ($\omega_0$ = 8.2) as the pH of the aqueous phase is lowered.

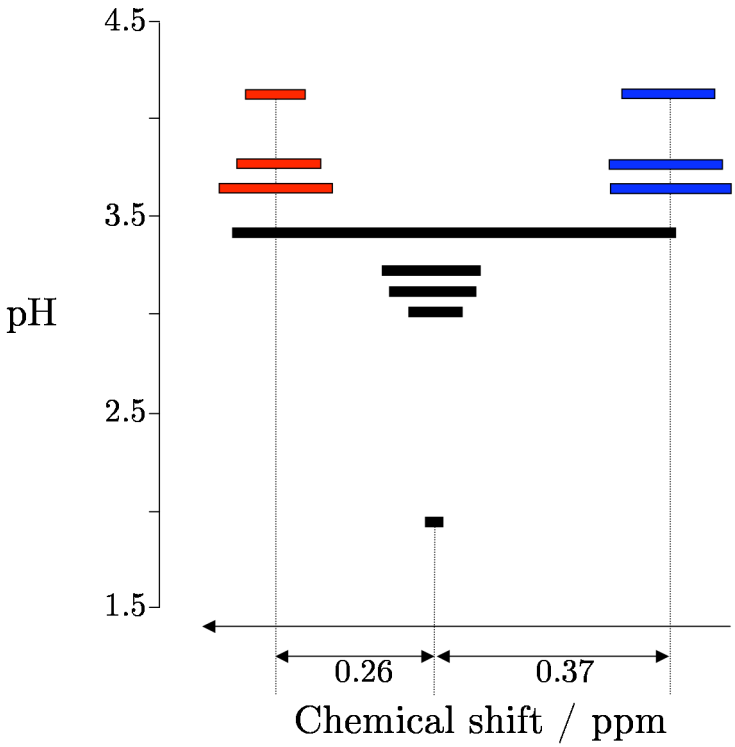


Figure 7.6: A plot representing the coalescence of hydroxyl resonances in a quaternary CTAB-hexane-pentanol-aq microemulsion ($\omega_0$ = 8.2). The length of the bar represents the line-width of the peak (the bar is the full-width-at-half-maximum of the peak). The red bars represent the hydroxyl-OH peak, the blue bars represent the water-OH peak and the black bars represent the coalesece hydroxyl peak.

## 7.11 Appendix 11

The findings that have been discussed in Chapter 4 and the conclusions that have been drawn have been presented in the Journal of Physical Chemistry B in a paper entitled "Detection of pH in Microemulsion, without a Probe Molecule, Using Magnetic Resonance". A copy of the paper can be found overleaf.

# Detection of pH in Microemulsions, without a Probe Molecule, Using Magnetic Resonance

**Nicola A. Halliday,[†] Andrew C. Peet,[‡] and Melanie M. Britton*[,†]**

*School of Chemistry and School of Cancer Sciences, University of Birmingham, Edgbaston, Birmingham B15 2TT, United Kingdom.*

*Received: September 10, 2010*

Proton NMR relaxation times have been used to probe the pH of water inside reverse micelles of a cetyltrimethylammonium bromide (CTAB)−hexanol−aq microemulsion. $T_2$ relaxation times were found to change with pH; however, $T_1$ relaxation times remained unaffected. This behavior was attributed to acid-catalyzed exchange between protons of water and hydroxyl protons of the cosurfactant hexanol. The rate of exchange and its influence on the $T_2$ relaxation time of water, inside the reverse micelle, were investigated as a function of water-to-surfactant ratio ($\omega_0$) and ionic strength. This exchange behavior and pH-dependent $T_2$ relaxation time were also observed for two other microemulsions—CTAB−hexane−pentanol−aq and Triton X-100−cyclohexane−hexanol−aq. Using this pH-dependent $T_2$ relaxation time, it was possible to monitor pH changes in the bromate−sulfite reaction inside a CTAB−hexanol−aq microemulsion.

## Introduction

Water-in-oil (w/o) microemulsions are thermodynamically stable, optically transparent, isotropic mixtures of water, oil, surfactant, and, frequently, cosurfactant. For certain compositions, the mixture self-organizes to form reverse micelles (RMs) of nanosized water droplets, sequestered from the continuous organic phase by a layer of surfactant, and frequently cosurfactant, molecules. These systems have been used as nanoreactors for chemical and enzymatic reactions,[1,2] utilized in the formation of nanoparticles[3] and proposed as possible drug delivery carriers.[4] Hydrated RM systems also serve as simplified models for biological systems since they share important features, such as confined water, interfacial regions, and partitioning of reactants.[1,5]

In w/o microemulsions a "bound" layer of water exists, which is associated with the polar moieties of the surfactant molecules; the remaining water forms a pool in the center of the droplet. As the size of this so-called "water pool"[6] increases, the water begins to behave more like bulk "free" water.[7,8] The size of the water pool is determined by the water-to-surfactant ratio $\omega_0$ (eq 1); an increase in $\omega_0$ correlates to an increase in the diameter of the droplet.

$$\omega_0 = [H_2O]/[\text{surfactant}] \quad (1)$$

In RMs, effective polarity, pH, ionic strength, and microviscosity of the confined water pools are known to be substantially different from those of bulk water.[9] Whether the macroscopic definitions of pH still apply in a restricted environment is also uncertain,[10] and there continues to be debate about the nature of pH inside RMs. Even so, the ability to measure pH in RMs is important in order to understand its effects on acid−base,[11] biochemical, and electron-transfer[12] reactions. Generally, the characterization of pH in w/o microemulsions has relied on the use of spectroscopic measurements of pH-sensitive probe molecules.[6,13−16] Several studies have used adsorption and fluorescence spectroscopy of organic dyes[17] or $^{51}V$ NMR of oxovanadate probes[18] to measure pH. However, when a probe molecule is used, an important variable in determining the pH inside the water droplets is the location of this molecule. Measurements using optical spectroscopy typically rely on the shifts of spectral peaks to explain molecular locations.[19,20] The location of probe molecules can also be determined using NMR experiments looking at chemical shift changes or NOE interactions.[18,21] It is found that there is a tendency for probe molecules to either reside in the surfactant layer or stick to the interface in the water droplet, and it is difficult to get a probe molecule to reside in the core of the micellar droplet. In addition to issues related to probe location, there are also questions about whether probe molecules change the structure of the RMs.[19,22] For example, Rack and co-workers discovered that the chromophore probe molecule $Ru(bpy)_3^{2+}$ was able to dramatically change the water content and distribution of droplet sizes in CTAB RMs. In order to avoid problems with probe molecules, an alternative method would be to measure the aqueous core directly. Experiments have been performed which achieve this by measuring the $^{31}P$ NMR chemical shifts of phosphate buffers contained in the RM.[10,14] The limitations with this approach are that a phosphate buffer is necessary, as the aqueous phase, and that an assumption is made that the $pK_a$ values of phosphate ions remain the same in the water pools as they were in bulk water.[10]

In this paper, we report a new method for determining pH in reverse micelles by probing the NMR signal of water, contained in the droplet core, directly. Magnetic resonance relaxation measurements were performed, and the effect of changing pH on $T_1$ and $T_2$ relaxation times of the aqueous droplets was observed for cationic (cetyltrimethylammonium bromide, CTAB) and nonionic (Triton X-100) surfactant based RMs. We have found that the $T_2$ relaxation time is sensitive to the pH of the aqueous core and so have been able to directly probe the pH inside these reverse micelles. This behavior is associated with exchange between protons in the hydroxyl groups in the alcohol and water. A $\omega_0$ and ionic strength dependence was also observed for this behavior.

* To whom correspondence should be addressed. E-mail address: m.m.britton@bham.ac.uk.
[†] School of Chemistry.
[‡] School of Cancer Sciences.

10.1021/jp108649x 
Published on Web 10/13/2010

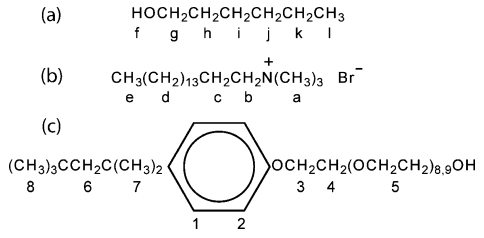


**Figure 1.** Molecular structure and numbering scheme for protons for (a) 1-hexanol, (b) CTAB, and (c) Triton-X.

## Experimental Section

Water-in-oil microemulsions were prepared by adding stock aqueous solution to a mixture of 1-hexanol (98%, Acros) and CTAB (cetyltrimethylammonium bromide, >98% (Aldrich); 1-pentanol (Sigma), *n*-hexane (Fisher), and CTAB or 1-hexanol, cyclohexane (>99%, Fisher) and Triton X-100 (Sigma). Reagents were used without further purification. High-purity water (Nanopure filtered, 18.0 MΩ cm) was used for all aqueous solutions. The pH of the water core was varied by titrating a stock solution of 0.1 M NaOH (>97%, Fluka) against a solution of 0.05 M $H_2SO_4$ (98%, Fisher). The pH of the aqueous solution was measured prior to the formation of the reverse micelles, using a glass combination pH electrode (Radleys) connected to a pH meter (Orion 720A). Measurements were typically made over a pH range of 1.1−9.2.

Cationic water-in-oil microemulsions with a droplet fraction ($\phi_d$) of 0.4 and $\omega_0 = 5.3$, 8.3, and 16.4 were formed by adding 0.8, 1.25, and 2.5 mL of the pH-adjusted, aqueous solution to 3.50 g CTAB in 6.2, 7, and 9 mL of 1-hexanol respectively. The values of $\omega_0$ investigated cover the range over which reverse micelles form in the (CTAB)−hexanol−aq system for a droplet fraction of 0.4.[23] Reverse micelles of different ionic strength were formed by increasing the concentrations of the acid and base in the titration. RMs were also formed using aqueous stock LiCl (Fluka, 98%) solutions of ionic strength 0.3, 0.15, and 0.075 M. The reported ionic strengths were calculated for the concentration of acid prior to addition of NaOH, assuming complete dissociation. The total change in the ionic strength for the titration was less than 0.025 M. A quaternary cationic microemulsion of $\omega_0 = 8.3$ was formed by adding 1.5 mL of the aqueoues stock solution to a mixture of *n*-hexane (10 mL), 1-pentanol (13 mL), and CTAB (3.64 g). Nonionic microemulsions of $\omega_0 = 8.3$ were formed by adding 670 $\mu$L of the aqueous stock solution to a mixture of cyclohexane (5.0 mL), 1-hexanol (2.7 mL), and Triton X-100 (2.65 mL). These systems are known[23−25] to form water-in-oil microemulsions and were mixed and used once transparent. The formation of reverse micelles in the CTAB−hexanol−aq microemulsion was confirmed using PGSE diffusion measurements. Figure 1 shows the structures and numbering scheme for protons of 1-hexanol and the CTAB and Triton X-100 surfactant molecules. Measurements of mixtures of hexanol and water were also made by adding 1 mL of pH-adjusted aqueous stock solution to 5 mL of 1-hexanol and shaking for 10 min. The mixture was allowed to rest for 10 min and a sample taken from the hexanol layer.

All magnetic resonance (MR) experiments were performed on a Bruker DMX300 spectrometer operating at a proton resonance frequency of 300 MHz, at 295 ± 0.1 K, in a 10 mm radiofrequency resonator. MR data were analyzed using the software package PROSPA.[26] Spectra were collected using a pulse-acquire sequence, [90°-acq], using 16k complex data points, at a spectral width of 20 kHz and a repetition time of 7 s, and acquiring two signal averages. The chemical shifts for peaks in the CTAB microemulsion spectra were calibrated using the chemical shift of the H-a peak in CTAB from a spectrum of the same system using $D_2O$ as the aqueous phase and TMP as the reference. The chemical shifts for peaks in the Triton X-100 microemulsion spectra were calibrated using a literature value for the H-8 peak in Triton X-100 from a reference spectrum found in the literature for Triton X-100.[27] $T_1$ relaxation times were measured using an inversion recovery experiment, $[180^\circ_x - \tau - 90^\circ_x - \mathrm{acq}]_n$, performing $n = 20$ experiments, with logarithmically spaced delay times ($\tau$) ranging from $5 \times 10^{-6}$ to 7 s. $T_2$ relaxation times were measured using a CPMG experiment, $[90^\circ_x - (\tau - 180^\circ_y - \tau)_m - \mathrm{acq}]_n$, performing $n = 28$ experiments, varying the number of echoes from $m = 0$ to 2400 (0 to 4200 for $\omega_0 = 16.4$) and using a delay of $\tau = 1$ ms. In all experiments, a repetition time of 7 s (>5$T_1$) was used and two signal averages were collected.

Diffusion measurements of water in CTAB−hexanol−aq reverse micelles ($\omega_0 = 8.3$) were performed using a pulsed field gradient spin echo (PGSE) sequence, 16 gradient increments, ramped between −120 and +120 G cm$^{-1}$, a gradient duration, $\delta$, of 1 ms, and an observation time, $\Delta$, of 250 ms. Eight signal averages were acquired with a repetition time of 5 s. The diffusion coefficient of water in the CTAB−hexanol−aq system was measured over the pH range 1.1−9.2 and found to remain constant at a value of $(1.8 \pm 0.16) \times 10^{-10}$ m$^2$ s$^{-1}$.

A CTAB−hexanol−aq microemulsion containing the bromate−sulfite reaction was prepared by first preparing two aqueous reagent solutions (1 and 2). Solution 1 was prepared by dissolving sodium bromate (1.51 g, Sigma-Aldrich) in 100 mL water, and solution 2 was prepared by dissolving sodium sulfite (1.26 g, Sigma-Aldrich) in 100 mL water with 1 M $H_2SO_4$ (1.5 mL). Two stock CTAB−hexanol−aq microemulsions were then prepared using the method described previously, where reagent solutions 1 or 2 were used as the aqueous phase. Equal volumes of these stock microemulsions were then mixed, with stirring, to give the bromate−sulfite−microemulsion reaction system.

## Results

$^1$H NMR spectra for microemulsions containing CTAB or Triton X-100 surfactants are shown in Figure 2. Peak assignments for these spectra are given in Table 1 for the CTAB microemulsion and Table 2 for the Triton X-100 microemulsion. Relaxation time measurements for water in the core of the reverse micelles (4.48 ppm) of the CTAB−hexanol−aq microemulsion, as a function of pH, are shown in Figure 3. The $T_1$ relaxation times are unaffected by a change in pH; however, the $T_2$ relaxation times are sensitive to pH at values lower than pH 6. The $T_2$ relaxation time is fairly constant above pH 6 but decreases steadily as the pH drops until pH 3, where there is then a rapid increase.

The underlying origins for this pH-dependent $T_2$ relaxation time were investigated by probing the effects of ionic strength, proton exchange, and $\omega_0$. As the pH was varied there was an associated change in ionic strength, with a minimum value of 0.125 M at pH 4 and 0.15 M at pH 1. To test the effect of ionic strength, LiCl was added to increase the ionic strength on the order expected during the variation in pH. However, no change in relaxation time was observed. The sensitivity of the pH-dependent behavior to ionic strength was further tested by performing a series of experiments, where the ionic strength was increased, by increasing the concentration of acid and base, from the maximum value at pH 1 of 0.15 to 0.45 M (Figure 4).

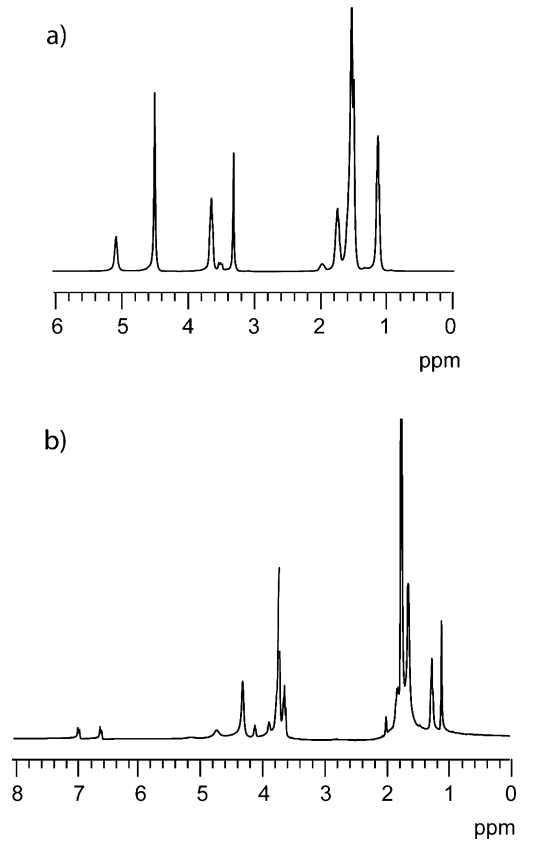


**Figure 2.** $^1$H NMR spectra at pH 7 for CTAB−hexanol−aq (a) and Triton-X−hexanol−cyclohexane−aq (b) microemulsions.

**TABLE 1: $^1$H NMR Peak Assignments for CTAB−Hexanol−Aq Microemulsion**

| δ/ppm | assignment |
|---|---|
| 5.10 | H-f |
| 4.48 | $H_2O$ |
| 3.69 | H-g |
| 3.55 | H-b |
| 3.35 | H-a |
| 1.98 | H-c |
| 1.71 | H-h |
| 1.56−1.40 | H-d, H-i, H-j, H-k |
| 1.10−1.02 | H-e, H-l |

The same trend in relaxation behavior is observed for all three experiments; however, there is a shift of the minimum to higher pH as the ionic strength is increased.

Proton exchange has been observed[28] between hydroxyl protons of butanol and water molecules in a quaternary microemulsion. Proton exchange is a well-known phenomenon[29−31] between hydroxyl protons in alcohol and water mixtures and is found to be catalyzed by acid or base. Proton exchange between the hydroxyl groups of the hexanol and water was probed as a function of pH in the CTAB−hexanol−aq reverse micelles, and a series of $^1$H NMR spectra, over a range of pHs, are shown in Figure 5. At pH 3.8 two peaks are observed, one for water ($\delta_{H_2O}$) and one for the hydroxyl group of hexanol ($\delta_{H-f}$). As the pH is decreased, these two peaks move together and eventually coalesce at an approximate pH of 3.4, appearing at a chemical shift of 4.66 ppm. It should be noted that in the CTAB−hexanol−aq microemulsion the $T_2$ relaxation

**TABLE 2: $^1$H NMR Peak Assignments for Triton X-100−Cyclohexane−Hexanol−Aq Microemulsion**

| δ/ppm | assignment |
|---|---|
| 7.13 | H-1 |
| 6.76 | H-2 |
| 4.66 | H-f |
| 4.23 | $H_2O$ |
| 4.00 | H-3 |
| 3.60 | H-5 |
| 3.47 | H-g |
| 1.42 | cyclohexane |
| 1.58−1.22 | H-7, H-i, H-j, H-k, |
| 0.84 | H-l |
| 0.64 | H-8 |

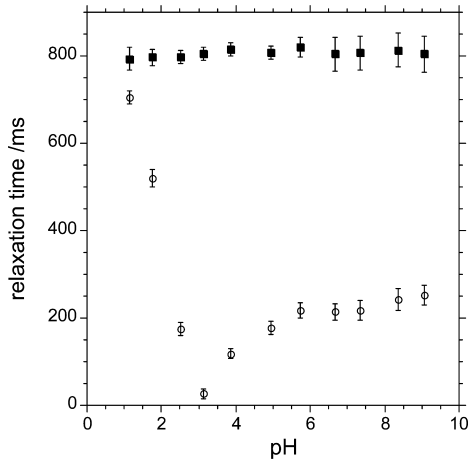


**Figure 3.** $T_1$ (■) and $T_2$ (○) relaxation times of water (peak 4.48 ppm from Figure 2a) in reverse micelles of a CTAB−hexanol−aq microemulsion with $\omega_0 = 8.3$. The pH refers to the pH of the aqueous phase prior to uptake into the microemulsion.

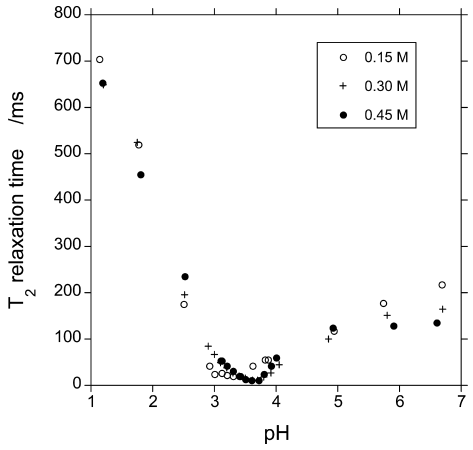


**Figure 4.** $T_2$ relaxation times of water (peak 4.48 ppm from Figure 2a) in reverse micelles of a CTAB−hexanol−aq microemulsion at $\omega_0 = 8.3$ and at aqueous stock ionic strengths of (at pH 1) 0.15 M (○), 0.30 M (+), and 0.45 M (●).

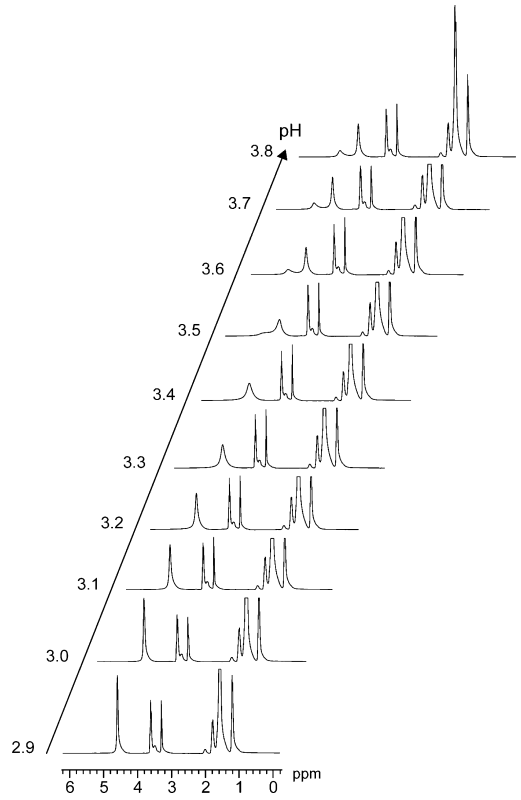


**Figure 5.** $^1$H NMR spectra of CTAB−hexanol−aq microemulsions over a droplet pH range of 2.9−3.8.

time is therefore measured using the $H_2O$ peak above pH 3.4 and using the coalesced peak below pH 3.4. The pH at which coalescence occurs corresponds to the minimum $T_2$ relaxation time. As the pH drops further, the peak linewidth decreases. The same effect is observed in $^1$H NMR spectra for mixtures of hexanol and water over a similar pH range and is shown in Figure 6. Again, at higher pH (pH 4), two peaks are observed, one for water ($\delta_{H_2O} = 4.60$ ppm) and one for the hydroxyl group of hexanol ($\delta_{H\text{-}f} = 5.38$ ppm). These peaks merge at approximately pH 3.7, following which the peak linewidth decreases.

Finally, the effect of $\omega_0$ was investigated on the pH-dependent relaxation behavior of CTAB−hexanol−aq droplets. Figure 7 shows the $T_2$ relaxation times for water, as a function of pH, for three $\omega_0$ values. While the same behavior is observed, the pH at which the minimum relaxation time appears shifts with $\omega_0$ and can be seen to increase with increasing $\omega_0$. Also, the chemical shift of the coalesced peak is found to move downfield as $\omega_0$ increases.

A quaternary system using the same surfactant− CTAB−hexane−pentanol−aq—was also studied, and the same behavior was observed. Having measured the change in relaxation times of water for CTAB RMs, a nonionic based microemulsion was investigated in order to determine how widespread this behavior was. Reverse micelles composed of Triton X-100 surfactants were investigated in the quaternary system Triton X-100−cyclohexane−hexanol−aq. Relaxation times for the droplet water (4.23 ppm), as a function of pH, are shown in Figure 8.

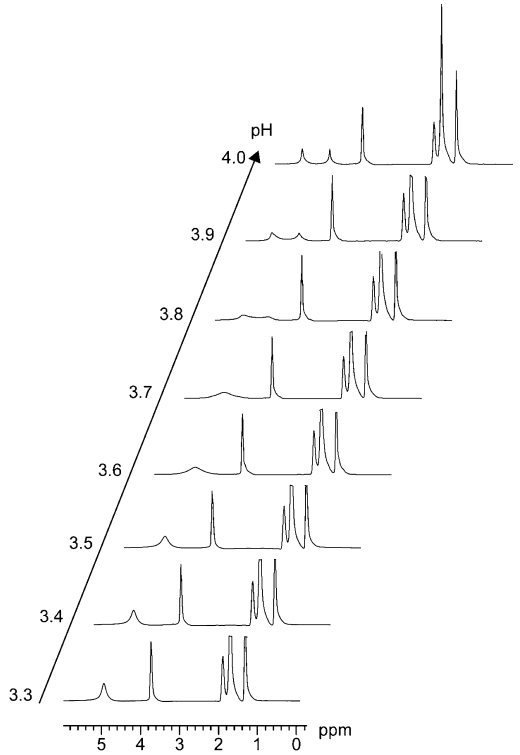


**Figure 6.** $^1$H NMR spectra for mixtures of hexanol and water over an aqueous pH range of 3.3−4.0.

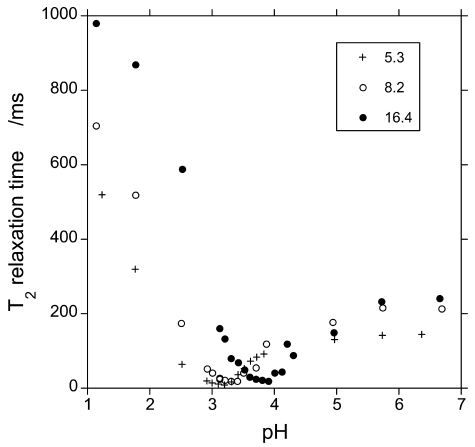


**Figure 7.** $T_2$ relaxation times of water (peak at 4.48 ppm from Figure 2a) in reverse micelles of a CTAB−hexanol−aq microemulsion at $\omega_0 = 5.2$ (+), 8.3 (○), and 16.4 (●).

As seen in the CTAB systems, the $T_1$ values remain constant while the $T_2$ relaxation times decrease as the pH decreases, to a minimum at pH 1.9. There then follows a rapid increase in $T_2$, as the pH drops further to pH 1. $^1$H NMR spectra for the same system, over the pH range 1.8−2.5, are shown in Figure 9. The water peak appears at a chemical shift of 4.23 ppm, with the alcoholic hydroxyl group at 4.66 ppm. As the pH decreases, these two peaks move together and start to merge at a pH of

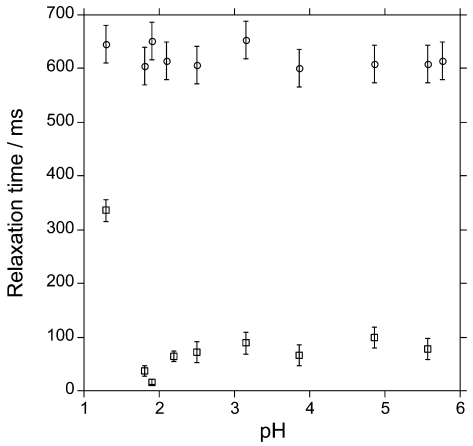


**Figure 8.** $T_1$ (○) and $T_2$ (□) relaxation times of water (peak at 4.23 ppm from Figure 2b) in reverse micelles of a Triton X-100−cyclohexane−hexanol−aq quaternary microemulsion system. The pH refers to the pH of the aqueous phase prior to uptake into the microemulsion.

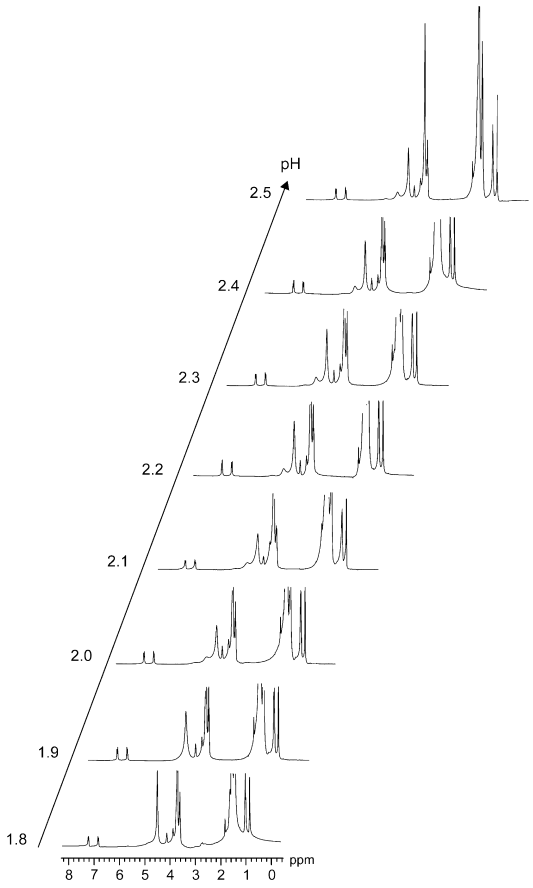


**Figure 9.** $^1$H NMR spectra for a Triton X-100 microemulsion system over a droplet pH range of 1.8−2.5.

approximately 1.9, following which the peak then further decreases in linewidth.

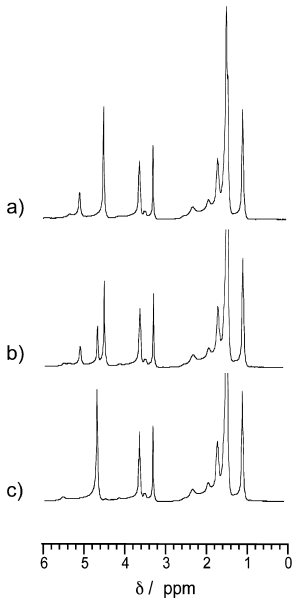


**Figure 10.** $^1$H NMR spectra for a CTAB−hexanol−aq microemulsion containing reactants for bromate−sulfite reaction at time intervals of (a) 80 min, (b) 90 min, and (c) 110 min following the mixing of reactants.

In order to determine whether the exchange process between the water and hexanol hydroxyl protons could be used to monitor pH changes during reaction, a test reaction was investigated in the CTAB−hexanol−aq system. The autocatalytic bromate−sulfite reaction was used, which is known to cause a pH change from pH 7 to 2, in aqueous solution.[32] This reaction is a clock reaction and after an induction period produces a rapid change in pH. Reagents from the bromate−sulfite reaction were contained inside CTAB−hexanol−aq reverse micelles (where $\omega_0 = 8.3$, $\phi_d = 0.4$, and $I = 0.3$ M), and a series of spectra were collected over time, three of which are shown in Figure 10. The spectrum in Figure 10a was taken at the start of the reaction during the induction period, when, in aqueous solution, the pH is 7. Two resonances are observed for the $H_2O$ (5.1 ppm) and H-f (4.48 ppm) protons. The next spectrum (Figure 10b) was taken midway through the reaction, and in addition to the peaks for the $H_2O$ and H-f protons, a third peak can now be observed between them (4.66 ppm). At this point in the reaction (and as the reaction mixture is unstirred inside the NMR magnet), there is a mixture of micelles at both the initial and final pH. Thus the spectrum shows separate peaks for the $H_2O$ and H-f protons, for RMs were the reaction has not yet clocked, as well as the coalesced peak, for RMs where the reaction has clocked. The final spectrum (Figure 10c) was collected once the system had fully clocked. In aqueous solution this corresponds to a final pH of 2. The $T_2$ relaxation time for $H_2O$ protons at the start of the reaction was found to be 172 ms, and the $T_2$ relaxation time of the coalesced peak at the end of the reaction was found to be 88 ms.

## Discussion

To the best of our knowledge, the variation in $T_2$ relaxation time with pH, for water inside a reverse micelle, has not previously been reported. The origins of this pH dependence

were investigated, looking at the influence of proton exchange, ionic strength, and $\omega_0$. The $T_2$ relaxation time sensitivity to pH was found to be a result of acid-catalyzed proton exchange between protons in the water and alcohol hydroxyl groups. Acid-catalyzed proton exchange is well-known[29−31,33−35] in mixtures of water and alcohol, and we also observed it in mixtures of hexanol and water, as a function of pH. By comparing $T_2$ relaxation times in the CTAB microemulsion with the corresponding spectra, it was observed that the minimum $T_2$ relaxation time marked the pH at which the water and alcohol proton resonances coalesced. Sensitivity to ionic strength inside the RM and $\omega_0$ was observed for the coalescence point and relaxation time; there was an increase in the pH at which coalescence occurred with increasing $\omega_0$ or ionic strength.

The presence of chemical exchange between protons in the water and the hydroxyl groups of hexanol, and its sensitivity to pH, was investigated. Where acid, which acts as a catalyst, is present in solutions of water and alcohol, fast exchange occurs between the protons in the water and hydroxyl group of the alcohol, leading to a single peak in the NMR spectrum. If all the acid is rigorously excluded, separate resonances are observed for these protons.[36] Separate resonances have been observed for the hydroxyl proton in pentanol and water in a nonionic microemulsion,[37] where no catalyst was present. In an investigation of the *N*-octylribonamide−brine−decane−butanol microemulsion, the composition of the microemulsion was found to control the rate of proton exchange between the water and butanol.[28] In our experiments on the CTAB microemulsion, a change in the rate of proton exchange between the water and hydroxyl groups of hexanol was observed as a function of pH. At a pH of 3.6 and higher, separate resonances were clearly observed for the water and hydroxyl groups of hexanol, indicating slow exchange. The minimum $T_2$ relaxation time was observed to occur at the pH value where the peaks had coalesced and hence where the measured peak was broadest.

In the pH range from 6 to 3.4, the rate of hydroxyl proton exchange is in the slow intermediate regime.[38] Exchanging spins will experience jumps in their precessional frequency and an increase in dephasing of the transverse magnetization, leading to a decrease in their relaxation time. Hence as the pH decreases from 6 to 3.4, the linewidth broadens for the two resonances (H-f and $H_2O$). As the pH decreases still further, the exchange rate increases, moving to the fast intermediate regime. A single, coalesced resonance is observed at the crossover between the two regimes (at pH 3.4). As the pH decreases below 3.4, the exchange rate increases further. This leads to greater averaging between the different precessional frequencies, and hence the linewidth of the coalesced peak reduces due to the rapid molecular jumps between the different chemical sites.[38] Thus, the relaxation time of the coalesced peak increases as the pH decreases from 3.4 to 1.1.

In fast intermediate exchange, the chemical shift at which the peak coalesces is a weighted average of the chemical shifts for the two separate resonances ($\delta_{H_2O} = 4.48$ ppm, $\delta_{H\text{-}f} = 5.05$ ppm) and is dependent upon the relative populations and average lifetimes of these resonances. The chemical shift of the coalesced peak was observed to move downfield (toward $\delta_{H\text{-}f}$) as $\omega_0$ increased, which suggested a related change in relative populations of the H-f and $H_2O$ protons and/or a change in their lifetime at the two sites. As $\omega_0$ changed the relative proportions of both hexanol and water were altered, thus affecting the chemical shift of the coalesced peak.

In our experiments, a change in the ionic strength inside the RM occurred as the pH decreased, due to the addition of greater amounts of acid. Ionic strength was calculated as a function of the concentration of all the ions present in solution by assuming complete dissociation and was found to vary from a minimum value of 0.125 M at pH 4 to a maximum of 0.15 M at pH 1. Ionic strength is known to have an effect on the size and structure of droplets inside a microemulsion,[39,40] which could then have a subsequent effect on the relaxation time of the water inside the droplets. However, little change was observed in the relaxation time of the water droplets when the ionic strength was increased through the addition of LiCl. The ionic strength was also increased by increasing the concentration of the acid and base used to vary the pH of the aqueous phase. A change in the absolute relaxation time, at a given pH, was observed; however, the same trend in behavior was still found. Thus this pH-dependent relaxation time behavior cannot be explained by a change in ionic strength. However, the coalescence point and hence rate of exchange are affected by ionic strength which may be due to the effect of ionic strength on the p$K_a$ of the alcohol and water.

The pH at which coalescence occurred was found to be dependent on the system. The coalescence pH in the hexanol/water mixture was found to be higher than that in the CTAB microemulsion, at a pH of 3.7 compared to pH 3.4. This difference could be due to how the pH was defined, which was as the pH of the aqueous phase prior to RM or mixture preparation. There could also be an inherent difference in the pH inside the RM associated with other factors such as the influence of the interface. The coalescence pH was found to be sensitive to ionic strength, which could affect the p$K_a$ of the alcohol and water, and was found to move to higher pH with increasing ionic strength. The coalescence point also changed with $\omega_0$ and was observed to go to higher pH as $\omega_0$ increased. This could be associated with a change in the proportions of hexanol and water at the interface and a change in the electrostatic nature of the interface. While these variations in coalescence pH are relatively small, they currently prevent a direct measure of pH inside the RM with absolute certainty. However, by looking at relaxation times or spectra, it is possible to closely monitor variations in pH.

The determination of the rate of proton exchange as a function of pH is not possible at this time. NMR line shapes and relaxation times cannot be related in a simple way to the rate of proton exchange in these highly complex systems, and there remain too many unknown parameters, such as the exchange rate of hexanol between the micelle interface and continuous phase and the relative proportion of hexanol in the interface. Work is continuing to model this system and determine these parameters, which would allow the exchange rate to be calculated. Further work is also being undertaken to understand the effect of $\omega_0$ and surfactant type on proton exchange in these reverse micelle systems.

Although challenges remain defining pH within a microemulsion droplet, the results here demonstrate that by following the relationship between proton exchange and pH, for a microemulsion of known composition, it becomes possible to observe the variation of pH inside the droplet without the need for a probe molecule. This was demonstrated in the study of the bromate−sulfite reaction in a CTAB−hexanol−aq microemulsion. By acquiring spectra over time, and using one of the calibration plots of $T_2$ against pH from Figure 4, it was possible to monitor the pH change during the reaction. Using the calibration plot at an ionic strength of 0.3 M (which corresponds to the ionic strength of the reaction[32]), the initial and final $T_2$ relaxation values (172 and 88 ms) were found to correspond to

pH values of 7.1 and 2.8, respectively. The final and initial pH values in aqueous solution, for this reaction, are typically 7 and 2, respectively. Measurements of the pH change in this reaction in microemulsions have been made previously using a pH electrode[32] and were also found to be higher in the CTAB−hexanol−aq microemulsion than in aqueous solution. The origins of these differences remains uncertain and requires further investigation.

The general applicability of this technique was tested by investigating two other microemulsions (CTAB−hexane−pentanol−aq and Triton X-100−cyclohexane−hexanol−aq) which used an alcohol as a cosurfactant. It was found that the same pH-dependent exchange behavior was observed, providing a means to probe the pH for water inside these RMs. In the Triton X-100 system the same trend in $T_2$ relaxation time was observed; however, the coalescence pH occurred at a higher acid concentration than the CTAB microemulsion. This could be explained by the highly charged interface of the CTAB RM, which may be more likely to facilitate the proton exchange mechanism, compared to the nonionic Triton X-100 RM interface.

## Conclusion

This paper reports the first application of $T_2$ relaxation times to probe the pH inside reverse micelles without the need for a probe molecule. $T_2$ relaxation times were found to change with pH, as a function of the rate of proton exchange between water and hydroxyl groups in the cosurfactant alcohol. A minimum $T_2$ relaxation time was observed at the point where the peaks for these resonances coalesced. The position of this $T_2$ minimum was investigated as a function of $\omega_0$ and ionic strength, and it was found that there was a small shift to higher pH with increasing ionic strength and $\omega_0$.

Although the question of how to precisely define pH within the water core of the reverse micelles is not addressed, this work demonstrates a unique way to monitor pH changes for a given microemulsion system. This was demonstrated in the investigation of pH changes produce during the bromate−sulfite reaction in a CTAB−hexanol−aq microemulsion. It is anticipated that this method can be applied to most microemulsions that utilize an alcohol as a cosurfactant, thus eliminating the need for a probe molecule.

**Acknowledgment.** The authors thank Dr. Annette Taylor for useful discussions and the University of Birmingham for funding.

## References and Notes

(1) Fendler, J. H. *Acc. Chem. Res.* **1976**, *9*, 153.
(2) Pileni, M. P. *J. Phys. Chem.* **1993**, *97*, 6961.
(3) Uskokovic, V.; Drofenik, M. *Surf. Rev. Lett.* **2005**, *12*, 239.
(4) Kogan, A.; Garti, N. *Adv. Colloid Interface Sci.* **2006**, *123*, 369.
(5) Bru, R.; Sanchezferrer, A.; Garciacarmona, F. *Biochem. J.* **1995**, *310*, 721.
(6) Menger, F. M.; Saito, G. *J. Am. Chem. Soc.* **1978**, *100*, 4376.
(7) Bhattacharyya, K.; Bagchi, B. *J. Phys. Chem. A* **2000**, *104*, 10603.
(8) Riter, R. E.; Willard, D. M.; Levinger, N. E. *J. Phys. Chem. B* **1998**, *102*, 2705.
(9) Levinger, N. E. *Science* **2002**, *298*, 1722.
(10) Smith, R. E.; Luisi, P. L. *Helv. Chim. Acta* **1980**, *63*, 2302.
(11) Miguel, M. D.; Burrows, H. D.; Pereira, M. A. E.; Varela, A. P. Probing solute distribution and acid-base behaviour in water-in-oil microemulsions by fluorescence techniques. 12th International Symposium on Surfactants in Solution (SIS), Stockholm, Sweden, 1998.
(12) Aoudia, M.; Rodgers, M. A. J. *J. Phys. Chem. B* **2003**, *107*, 6194.
(13) El Seoud, O. A.; Chinelatto, A. M.; Shimizu, M. R. *J. Colloid Interface Sci.* **1982**, *88*, 420.
(14) Fujii, H.; Kawai, T.; Nishikawa, H. *Bull. Chem. Soc. Jpn.* **1979**, *52*, 2051.
(15) Hasegawa, M. *Langmuir* **2001**, *17*, 1426.
(16) Lay, M. B.; Drummond, C. J.; Thistlethwaite, P. J.; Grieser, F. *J. Colloid Interface Sci.* **1989**, *128*, 602.
(17) Biswas, S.; Bhattacharya, S. C.; Bhowmik, B. B.; Moulik, S. P. *J. Colloid Interface Sci.* **2001**, *244*, 145.
(18) Crans, D. C.; Rithner, C. D.; Baruah, B.; Gourley, B. L.; Levinger, N. E. *J. Am. Chem. Soc.* **2006**, *128*, 4437.
(19) Rack, J. J.; McCleskey, T. M.; Birnbaum, E. R. *J. Phys. Chem. B* **2002**, *106*, 632.
(20) Saez, M.; Abuin, E. A.; Lissi, E. A. *Langmuir* **1989**, *5*, 942.
(21) Binks, D. A.; Spencer, N.; Wilkie, J.; Britton, M. M. *J. Phys. Chem. B* **2010**, in press.
(22) Baruah, B.; Swafford, L. A.; Crans, D. C.; Levinger, N. E. *J. Phys. Chem. B* **2008**, *112*, 10158.
(23) Ekwall, P.; Mandell, L.; Fontell, K. *J. Colloid Interface Sci.* **1969**, *29*, 639.
(24) Wu, J. M.; Yan, H.; Zhang, X. H.; Wei, L. Q.; Liu, X. G.; Xu, B. S. *J. Colloid Interface Sci.* **2008**, *324*, 167.
(25) Colafemmina, G.; Palazzo, G.; Balestrieri, E.; Giomini, M.; Giustini, M.; Ceglie, A. Towards the comprehension of the cosurfactant role: A NMR self-diffusion and conductivity study of a four-components water-in-oil microemulsion. In *Trends in Colloid and Interface Science Xi*; Rosenholm, J. B., Lindman, B., Stenius, P., Eds.; Dr Dietrich Steinkopff Verlag: Berlin 33, 1997; Vol. 105, p 281.
(26) Magtritek. Prospa; http://www.magritek.com/prospa.html.
(27) Yuan, H.-z.; Miao, X.-j.; Zhao, S.; Shen, L.-f.; Yu, J.-y.; Du, Y.-r. *Magn. Reson. Chem.* **2001**, *39*, 33.
(28) Bastogne, F.; Nagy, B. J.; David, C. *Colloids Surf., A* **1999**, *148*, 245.
(29) Fukumi, T.; Fujiwara, Y.; Arata, Y.; Fujiwara, S. *Bull. Chem. Soc. Jpn.* **1968**, *41*, 41.
(30) Oakes, J. *J. Chem. Soc., Faraday Trans. 2* **1973**, *69*, 1311.
(31) Paterson, W. G. *Can. J. Chem.−Rev. Can. Chim.* **1963**, *41*, 2472.
(32) McIlwaine, R. E.; Fenton, H.; Scott, S. K.; Taylor, A. F. *J. Phys. Chem. C* **2008**, *112*, 2499.
(33) Coccia, A.; Indovina, P. L.; Podo, F.; Viti, V. *Chem. Phys.* **1975**, *7*, 30.
(34) Hills, B. P. *J. Chem. Soc., Faraday Trans.* **1990**, *86*, 481.
(35) Kuppers, J. R.; Carriker, N. E. *J. Magn. Reson.* **1971**, *5*, 73.
(36) Hore, P. J. *Nuclear Magnetic Resonance*; Oxford University Press: Oxford, U.K, 1995.
(37) Waysbort, D.; Ezrahi, S.; Aserin, A.; Givati, R.; Garti, N. *J. Colloid Interface Sci.* **1997**, *188*, 282.
(38) Levitt, M. H. *Spin Dynamics*; John Wiley and Sons Ltd: Chichester, U.K., 2001.
(39) Guering, P.; Lindman, B. *Langmuir* **1985**, *1*, 464.
(40) Hamada, K.; Ikeda, T.; Kawai, T.; Kon-No, K. *J. Colloid Interface Sci.* **2001**, *233*, 166.

JP108649X

## 7.12 Appendix 12

Figure 7.7a shows data acquired from a 2D pulse-acquire sequence performing 64 experiments and acquiring 4096 real data points per experiment for a spectral width of 10000 Hz. The plot therefore corresponds to a chemical shift versus time plot with one data point equal to 10000/4096 Hz. Figure 7.7b shows 1D representations of selected experiments during the course of the bromate-sulfite-CTAB reaction. The hydroxyl resonances have been highlighted in both figures.

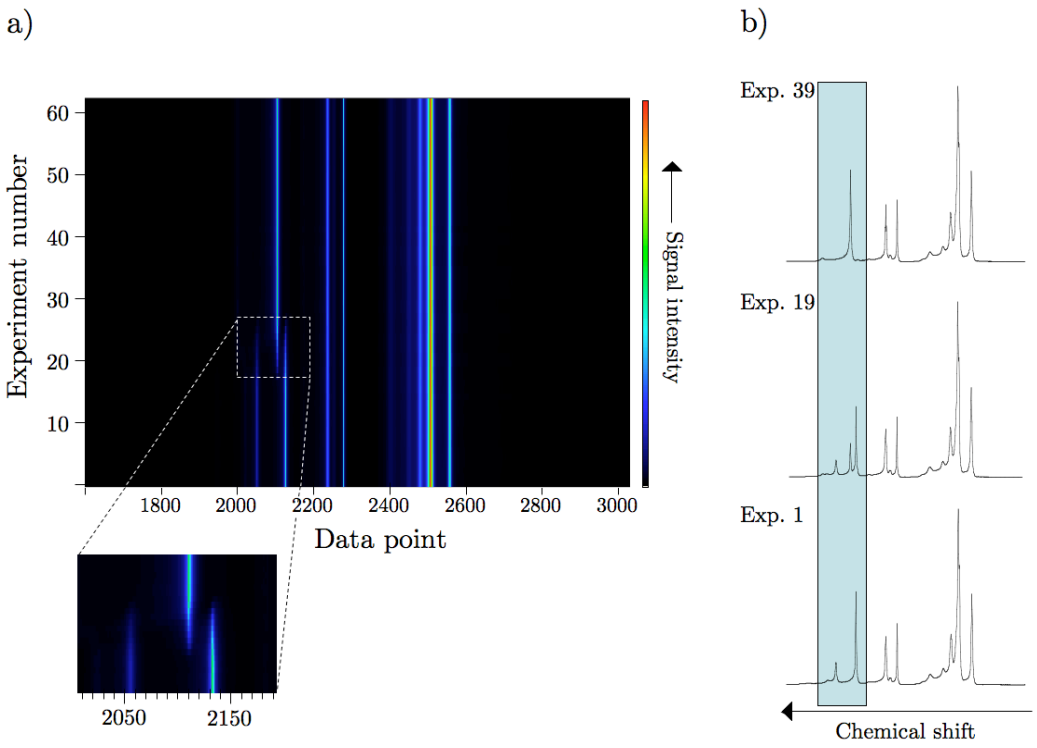


Figure 7.7: Results from 2D-zg measurements of the bromate-sulfite-CTAB system. The 2D plot (a) shows data points versus experiment number, which corresponds to chemical shift against time. The point of coalescence between the hydroxyl proton frequencies is enlarged. One-dimensional representations of specific experiments are shown in b). The highlighted region shows (from bottom to top) two proton resonances for hexanol and water hydroxyl protons in the reactant system, three resonances when both reactant and product regions exist within the sample and, finally, one resonance proton frequency for the product environment. The chemical shift scale is shown here in the conventional way of increasing from right to left.

The chemical shift difference between product and reactant hydroxyl resonance frequencies was determined using the following calculation:

$$\left(\begin{matrix}\text{reactant peak}\\ \text{data point}\end{matrix} - \begin{matrix}\text{product peak}\\ \text{data point}\end{matrix}\right) \times \frac{\text{spectral width (Hz)}}{\text{total number real data points}} = \text{frequency difference (Hz)}$$

$$\frac{\text{frequency difference (Hz)}}{\text{operating frequency (MHz)}} = \text{chemical shift difference (ppm)}$$

Thus, the change in chemical shift of the water peak is;

$$\left(2134 - 2112\right) \times \frac{10000}{4096} = 53.7 \text{ Hz} \quad \text{or} \quad \frac{53.7}{300} = 0.179 \text{ ppm}$$

and the change in chemical shift of the hexanol-OH peak is;

$$\left(2058 - 2112\right) \times \frac{10000}{4096} = -131.8 \text{ Hz} \quad \text{or} \quad \frac{-131.8}{300} = \text{-}0.439 \text{ ppm} .$$